UNIVERSITY OF NAPLES FEDERICO II

DEPARTMENT OF INDUSTRIAL ENGINEERING

PH.D. THESIS

A LUMPED PARAMETER APPROACH ON EXTERNAL GEAR PUMPS: ANALYSIS AND OPTIMIZATION TO REDUCE NOISE EMISSIONS

Advisors:

Ch.mo Prof. Ing. Adolfo Senatore

Ch.ma Prof.ssa Ing. Emma Frosina

Ch.mo Prof. Ing. Pietro Marani

Ch.ma Prof.ssa Ing. Tatiana Minav

Dott. Ing. Michele Pavanetto

Candidate:

Pietro Mazzei

Matr. DR995132

PH.D. CYCLE XXXVI

Table of Contents

List of Tables

List of Figures

Chapter I: Introduction

I.1. Background

Since about the early 2000’s years, the majority of the industrial fields are undergoing deep transformations. These transformations are the results of the process of electrification and hybridization involving all type of machines [1-2]. This development is led by the needs to achieve increasing energy efficiency levels as a reaction to the rise of the global warming due to the combustion of fossil fuels to power machines. Fluid Power applications are one of the most impacted categories by these changes. Scientific community and industrial companies both presented many examples of machines’ electrification and hybridization for both off-road and on-road mobile applications that showed robust gain in the overall machine efficiency [3-4].

Despite the promising results, research also shown some limits of the electrical machines: their lower energetic power density prevents their use in heavy-duty applications [5] that represents the most employed case and the principal cause of pollutant and greenhouse gas emissions for this industrial sector. This is the reason today is still of utmost importance to research new methods and methodologies to improve the performance and the global efficiency of both components and systems of traditional hydraulics machines.

Modern fluid power systems require to be both extremely efficient while maintaining noise and vibrations emission under determined level.

This restriction needs to be enforced both to respect the ever increasingly stringent regulation and to remain competitive against the process of mechanical electrification substitution.

The electrification process actually has given new strength to the research, due to highlighting of new limits and shortcomings of hydraulic drive systems. In fact, the implementation of quieter electric drives in place of the noisier traditional internal combustion engines made more relevant the noise emissions from the hydraulic units, becoming the predominant source in some applications.

The primary sources of noise in hydraulic systems are pumps and motors. For these machines, the noise sources are of two types: fluid-borne noise (FBN) and structure-borne noise (SBN). FBN is due to flow ripples while SBN is mainly caused by the vibration of mechanical components as a consequence of force oscillations. These two typologies of noise sources affect the total air-borne noise (ABN) emission.

Therefore, in order to study and reduce the ABN in an effort to provide increasingly comfortable working conditions, the understanding of fluid-dynamics responsible for the noise emissions is fundamental. To offer increasingly comfortable and healthier working conditions the understanding of fluid dynamics responsible for the generation of is essential. So, researchers are focusing on reducing the noise emissions without compromising the fluid dynamics performances and the global efficiency.

To reach this challenging objective, scientific researchers have various instruments. In the past, the principal tool to enhance the performances of a machine was through implementations of experimental tests. This approach required extended period of times and a tremendous prototyping demand. Nowadays, the availability of high computational power permits to execute a simpler and streamlined prototyping process in consequence of the use of *digital twins* of the machine. The numerical models implemented in the digital twins' simulations are characterized by the type of methodologies utilized to simulate the machine analyzed. The most utilized implement three-dimensional CFD (Computational Fluid-Dynamics) or lumped parameters approaches, especially for the Fluid Dynamics applications. Each methodologies present pros and cons but both permit to study, analyze and optimize the investigated hydraulic machine through the implementation of numerical models and have become essential tools.

External Gear Pumps (EGPs) are a typologies of displacement machines that are widely used for energy transmission in hydraulic and fluid power systems, especially the mobile ones. They are simple and robust hydraulic components, suitable to work at a wide range of pressures and rotational speeds. They are also characterized by long life, high reliability and efficiency, compactness, low weight, low cost and minimum maintenance. Unfortunately, those pumps are of the fixed displacement type, making thus the handling of workload variations more complex and less efficient compared to other typology of pump with variable displacement. In addition, EGPs are generally characterized by relative high levels of emitted noise and vibrations. To improve this typology of hydraulic machines, tools to better understand and analyze the physics involved in the generation of noise emissions are necessary to help researchers.

I.2. Objective

Main objective of this Ph.D. thesis is the development of a comprehensive tool based on numerical modeling that permits to analyze, design and optimize EGPs, with the main focus being the reduction of the vibrations and noise emission phenomenon.

The developed tool was based on a lumped parameter approach. This approach was chosen against a 3D CFD approach due to its more flexibility and less computational power requirements that permits to execute a high number of simulations, allowing thus to also execute optimization procedure that were the final objective. But the 3D CFD approach was not completely set aside, in fact, it was used in in a hybrid mode combination with experimental measurements to validate the lumped parameter model, reducing thus the number of measurements to be performed.

The methodologies, techniques and approaches described in this thesis are developed by the Fluid Power Research Group of the Industrial Engineering department of the Federico II University of Naples lead by Prof. Senatore and Prof. Frosina. The Ph.D. program, which this thesis is the culmination, is of a particular type that needs a brief explanation to better comprehend the work done. It belongs to a particular type, named *Industrial*, established by the Italian Ministry of Education, University and Research. This program imposes a robust industrial characterization aimed to create high doctoral level specialization that could easily be employed in the Italian productive system. This is executed by a rigorous collaboration between the University promoter of the Ph.D. program with Italian companies and foreign universities. For this work, the University of Naples Federico II collaborated with the international company Duplomatic Motion Solution, the Italian National Research Council (in Italian *Consiglio Nazionale delle Ricerche, CNR*), in particular with the STEMS Institute (Sciences and Technologies for Sustainable Energy and Mobility) located in Ferrara, and with the Tampere University (Finland), in particular with the Innovative Hydraulics and Automation (IHA) Center.

The following section will briefly describe the working principle of EGPs and the actual state of the art of research literature about the study of them. The third section will describe in great detail the developed tool working principles and governing equations for the different aspects modelled. The fourth section will show the result of the validation process of the lumped parameters approach by meaning of both 3D CFD model and experimental measurements. The fifth section will describe the optimization procedure developed aimed at reducing the noise emissions and the results obtained from an experimental campaign on a prototype optimized pump against a reference one.

Chapter II: External Gear Pump

II.1. Working Principles

External Gear pumps (EGPs) are one of the simple designs and most cost attractive of all the positive displacement machines in the market. These are the main reasons why they are the mostly use hydrostatic pumps among the fixed displacement machines in the industry for all that cases where the application does not require a variable displacement volumetric machine. They are employed in a large variety of applications, from simple charge pumps and lubrication pumps for low pressure level to the high pressure range used in the industrial and heavy-duty field, with maximum working pressure of over 300 bar. Figure 1 displays a cross section of a typical EGP with the main components indicated.

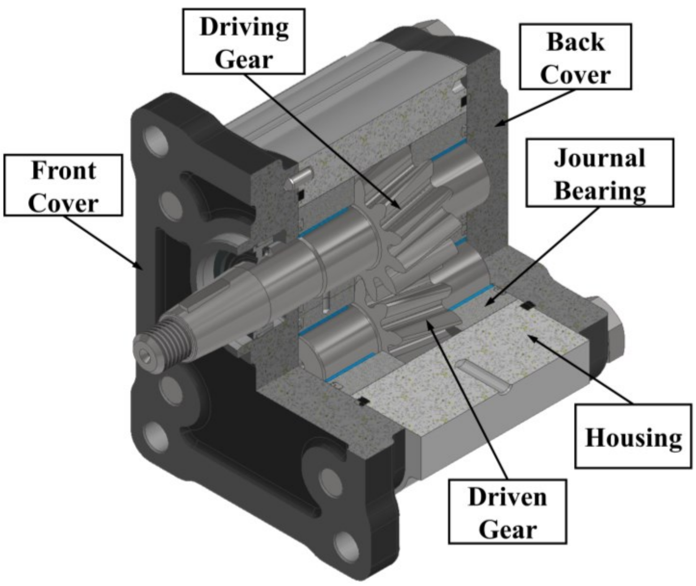

Figure 1 - Typical structure of an EGP.

The pump consists of two gears, a *driving gear* that leads a *driven gear*. The gears' shafts are supported through journal bearings. The *housing* contains the main component and the assemble is closed thanks to two covers. The working principle is based on the variable displacement chamber [6] and is showed in Figure 2.

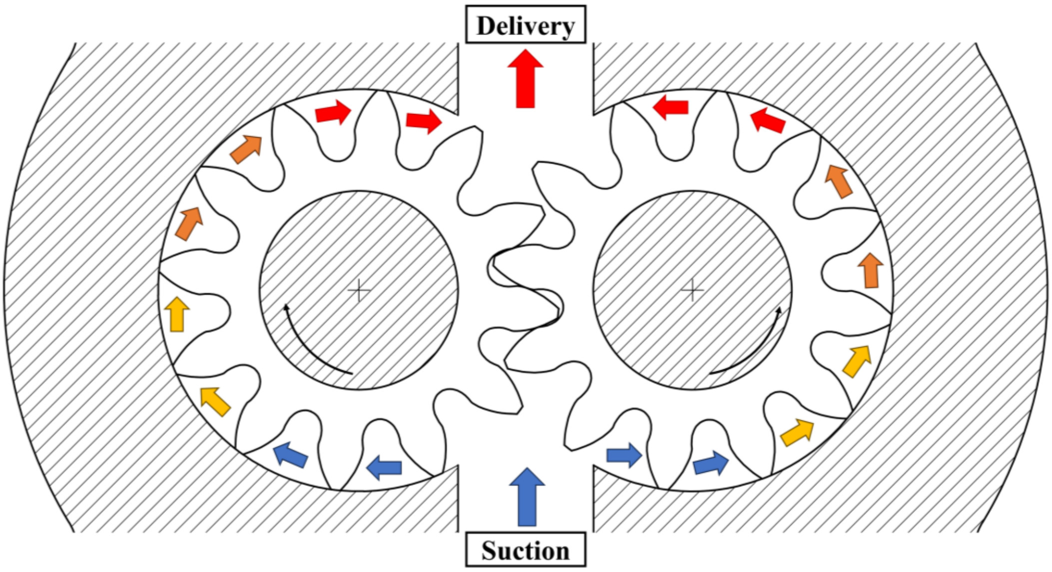

Figure 2 - Working principle of EGP.

The variable displacement chambers are each volume between two adjacent teeth for each gear. The gears' rotation moves away the teeth after the meshing zone, increasing the available volume that is filled by the fluid coming from the suction area. The fluid is then transferred in circumferential direction along the rotating gears until it arrives at the delivery area. The fluid is eventually pressurized by the volume reduction of the displacement chambers due to the meshing of the gears and it is then delivered outside the pump.

The teeth of the gears could employ different geometries, but the most used one are teeth with an involute profile. The axial development of the gears is another factor that heavily influence the noise and vibration emitted. The typical and most implemented axial geometry is the straight profile. This axial profile is the simplest to manufacture but also the worst regarding the noise emission due to higher flow ripples and pressure peaks in the meshing zone. A profile more suited to produce better noise performance is the helical geometry, where the teeth profiles are shifted along the axial dimension through a helical angle. This geometry allows lower flow ripples amplitude and pressure peaks, reducing thus the vibrations and the noise produced. The con of this geometry is the appearance of a thrusting axial force that makes the pump's dynamic control more challenging. Finally, in late years, the continuous contact circular helical gear profile was also explored. This profile further improves the noise and vibration emission thanks to minimum flow ripples but requires very precise and costly mechanical manufacturing process to obtain a correct meshing, limiting thus its application to only limited niche scenarios. The described teeth's profiles are exhibited in Figure 3.

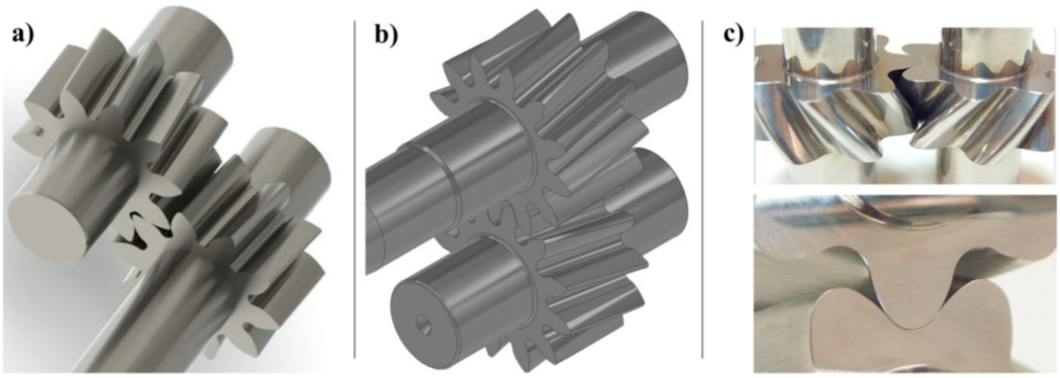

Figure 3 - Type of teeth profiles: a) spur gears; b) helical Gear; c) continuous-contact circular helical gear.

II.2. State of the Art

Even if EGPs have a simple working principle and low number of components, obtaining good volumetric efficiency coupled with low noise and vibration emissions is not a simple task. This is the reason many studies and research can be found in the scientific literature.

The industries' request of low noise pump with great overall efficiency pushed the research to find instruments to analyze EGPs and find solutions to minimize flow ripple fluctuations and pressure spikes. One of the possible responses to this request is the utilization of numerical models to analyze, predict and optimize the EGPs and reach the desired objectives.

There are different typologies of numerical models that can be implemented. Rundo [7] analyzed all the possible typologies that can be utilized to simulate EGPs, starting from the lumped parameters to the 3D CFD, describing their pros and cons.

To reduce the noise emissions, it is fundamental to understand and improve the flow behavior, as showed by Manring and Kasaragadda [8]. A way to analyze this aspect could be focusing only on this aspect. In this regard, Zhao and Vacca [9] investigated the theoretical kinematic flow ripples' source of EGPs through a lumped parameter approach.

The first models developed analyzed spur gears pumps. Frosina et al. [10] simulated a spur gear pump for high-pressure applications through a CFD model obtaining good accuracy against experimental measurements for both steady state and dynamics pump characteristics. Vacca and Guidetti [11] instead, studied a similar spur gear pump by means of a lumped parameter approach, obtaining great validation results compared to experimental results, too.

Other studies that implement lumped parameters approach models were done by Borghi et al. [12] [13] and Mancò and Nervegna [14] who investigated spur EGPs obtaining high accuracy against experimental data.

Haisler et al. focused their work on EGPs with helical gears [15]. They used a CFD approach employing some geometrical approximation to reduce the higher computational power required by the helical angle. Nevertheless, they succeeded in obtain good accuracy of the results. Many other similar 3D CFD models are available in literature like the work proposed by Qi et al. [16] and Corvaglia et al. [17].

Lumped parameter based models were employed also for the study of helical EGPs. Rasegnola et al. [18] apply a numerical tool to compare the results from simulations between spur and helical gear machines while Battarra and Mucchi [19] described a numerical model to predict pressure evolution of both spur and helical gear pumps.

One of the advantages of the lumped parameter-based approach model is the possibilities to be coupled with mechanical models to evaluate the forces and torques applied on the gears as well as their micromotion and their hydrodynamic balance with the supporting bearings. This possibility was exploited by many works, like the one by Zardin and Borghi [20], Marinaro et al. [21], Falfari and Pelloni [22], Mucchi et al. [23] [24] [25] [26], and by Rituraj et al. [27].

Other research available in literature employed 2D numerical modeling approaches with deforming mesh and volume re-meshing. Both

Strasser [28] and Orlandi et al. [29] successfully utilized this approach, however, even if they obtained striking results, they cannot evaluate the complete complexity of the internal flows like the 3D models and do not possess the same flexibility of the lumped parameter approach.

The flexibility of the lumped parameter approach allows to emphasis singular aspect or phenomenon of the analysis of the EGPs. Rituraj et al. [30] analyzed the possibility to model the thermal effects of the fluids using a lumped numerical approach, while Zhou et al. [31] developed a lumped parameter model to evaluate the gas cavitation process in External Gear Machines (EGMs).

Other researchers focused them enquire to simulate design modification in order to reduce the noise and vibration emissions. Marinaro et al. [21] investigated the use of an accessory volume to reduce the flow ripples' amplitude. Devendran and Vacca [32] explored the effect of modifying the design of the pressure relief grooves of an EGP.

Finally, the latest research also explored the numerical modeling for EGPs with continuous contact circular helical gears, like the work by Zhao et al. [33], obtaining promising results.

The majority of the literature focuses on fluid or hydromechanical aspects, analyzing the behavior of EGPs in various conditions or investigating particular solutions to enhance performance for specific cases. However, very few research work is available where the focus is the noise aspect of the EGPs or the development of a tool to optimize existing EGPs. This lack in literature, coupled with the industrial nature of the doctorate, were the driving forces behind the development of a tool capable of optimizing the EGPs from the sound emission point of view that is detailed in this thesis work.

Chapter III: Lumped Parameter Numerical Model

III.1. The Approach

III.1.1. Introduction

The lumped parameter-based numerical model implemented in the developed tool is based on the control volume (CV) approach. This methodology subdivides the area domain of the object of analysis in a number of control volumes, each of them assumed to have physical homogeneous properties, such as such as pressure, temperature, density, etc. These CVs are modeled as capacitive elements, evaluating the pressure value inside them as a function of the net ingoing flow rate. These CVs are connected to each other thanks to a series of resistive elements. These connection elements evaluate the net flow rate between CVs as a function of the pressure drop through them. Typical example of a resistive elements are the variable restrictors with both the turbulent and laminar flow regime possible. To obtain a numerical model with a good accuracy it was fundamental to correctly identify all the CVs and the type of the connections between them, that is dictate the proper governing equations.

III.1.2. Governing Equations

The tooth space volume (TSV) between two adjacent teeth for each gear was defined as the base control volume of the defined model. Being a lumped parameter approach, each CV was modeled as a capacitive element with homogeneous physical properties. The time variation of the pressure inside the CV is expressed as a function of the net ingoing flow rate:

$$\frac{dp_i}{dt} = \frac{\beta_k}{V_i}\left(\sum Q_i - \frac{dV_i}{dt}\right) \tag{1}$$

being β_k the fluid bulk modulus, V_i the volume of the CV and Q_i the volumetric flow rate, positive if ingoing. The first term in the parentheses represents the variation of the amount of fluid in the CV, the second term the variation of the volume of the CV itself.

The evaluation of the volumetric flow rates entering and departing the CV depends on the typology of the physical connection considered. The connections of the CV inside the meshing zones, with the pressure relief grooves and with the inlet and outlet volumes were modeled as a generic (no specific shape) turbulent orifice, thus the volumetric flow rate was expressed as:

$$Q_i = C_d A_i(\varphi)\sqrt{\frac{2|\Delta p|}{\rho}} \times sign(\Delta p) \tag{2}$$

where C_d is the flow discharge coefficient, A_i is the cross-sectional area of the orifice (constant or variable) function of the pump's rotational angle, Δp is the pressure difference between the CV analyzed and the preceding/following one, and ρ is the average working fluid density between the two CVs considered.

The flow discharge coefficient C_d present in Equation (2) is a parameter that influence the orifice behavior and it is determined with the following relation:

$$C_d = C_{d,max} \tanh\left(\frac{2\lambda}{\lambda_{crit}}\right) \tag{3}$$

where $C_{d,max}$ is the maximum flow coefficient, λ is the flow number, and λ_{crit} is the critical flow number. The values of $C_{d,max}$, and λ_{crit} present in equation (3) are parameters defined by the input user that can be changed to tweak the orifice's behavior.

To obtain thus the value of C_d it is necessary to know the flow number λ that is defined as:

$$\lambda = \frac{D_h}{\nu}\sqrt{\frac{2|\Delta p|}{\rho}} \tag{4}$$

Being D_h the orifice's hydraulic diameter and ν the kinematic viscosity determined at the pressure average between the two CVs considered. The hydraulic diameter of the generic orifice was evaluated as a function of the total orifice area and its wetted perimeter:

$$D_h = \frac{4 \cdot Area}{perimeter_{wet}} \tag{5}$$

The remaining connections to be modeled were the internal leakages, named tip, side and radial leakages. For these typologies of connection, both Couette and Poiseuille flow rate contributions were considered.

Tip leakages flow rate (Figure 4) were evaluated under the assumption that the equivalent considered orifice was of the flat rectangular type.

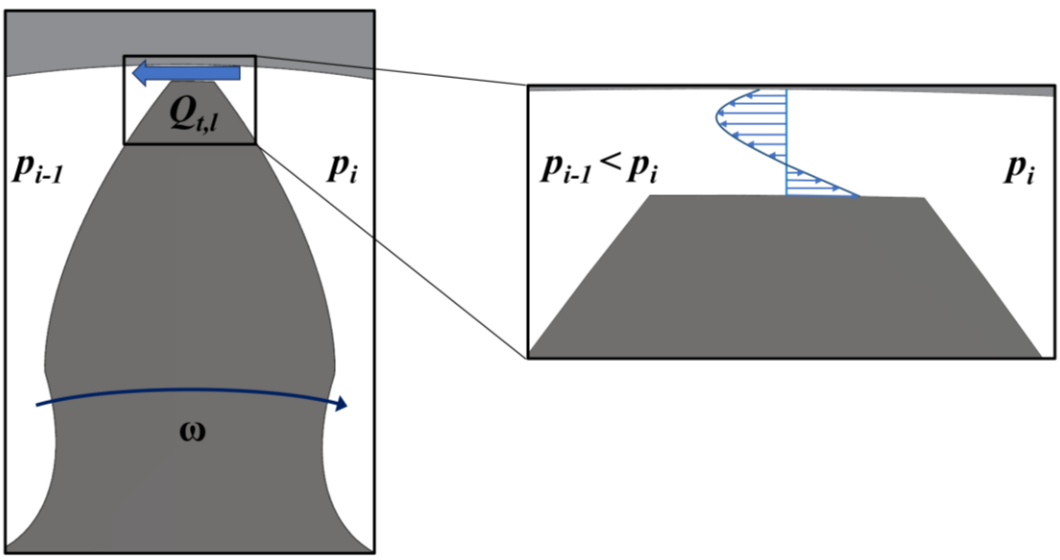

Figure 4 - Tooth tip leakage flow rate.

Under these assumptions, the tip leakage flow rate for a single tooth was evaluated with the following formulation:

$$Q_{tl} = \frac{bh_{tip}^3}{12\mu l_{tip}}\Delta p - \frac{bh_{tip}u_t}{2} \quad (6)$$

where b is the gear's axial width, h_{tip} is the variable height of the clearance along the sealing zone, μ is the dynamic viscosity determined at a mean value between p_i and p_{i-1}, l_{tip} is the tooth tip's width, and u_t is the tangential velocity at the tooth's tip. From Equation 6, the first part represents the Poiseuille flow contribution (pressure related) while the second one the Couette flow contribution (speed related).

The side leakages flow rate (Figure 5) require a more detailed analysis due to the structure of the tooth that demand a more complex structure of the orifice to reach a sufficient accuracy level. The tooth profile was divided into n slices, each of them characterized by the same height but different width.

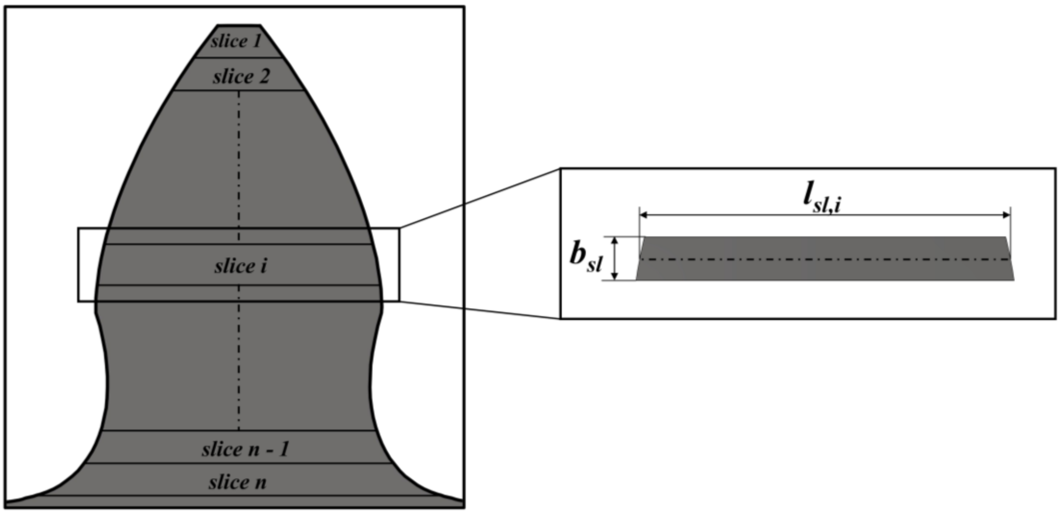

Figure 5 - Side tooth leakage flow rate.

The resulting equation to evaluate the side tooth leakage flow rate for a single tooth is the following:

$$Q_{sl} = 2\sum_{i=1}^{n}\frac{b_{slice}h_{side}^{3}}{12\mu l_{i,slice}}\Delta p \tag{7}$$

where b_{slice} is the height of each of the n slice, $l_{i,slice}$ is the average width of the *i-th* slice, and h_{side} is the gap clearance between the gears' side face and the wear plates. This clearance is user inputted and it is maintained constant during the simulation. The factor two was added to the equation to consider the flow rate from both side of the tooth. Equation 7 exhibited only the Poiseuille flow rate contribution due to the fact that this contribution is equally applied to both sides, resulting in a null net contribution. Typically, for teeth similar to the one analyzed in this work, a number of slices between 5 and 10 allows to obtain excellent results.

The radial leakages flow rate (Figure 6) were modeled similarly to the side leakages flow rate without the need to the more complex definition of the orifice geometry.

The resulting equation that regulates this leakage flow rate for a single CV is shown in Equation 8:

$$Q_{rl} = \frac{b_{rl}h_{side}^{3}}{12\mu l_{rl}}\Delta p \tag{8}$$

where b_{rl} is the arc length between two adjacent teeth on the gear's root diameter, and l_{rl} is distance difference between the gear's root and shaft diameter. Even for this typology of leakages, the Couette net flow rate contribution is zero.

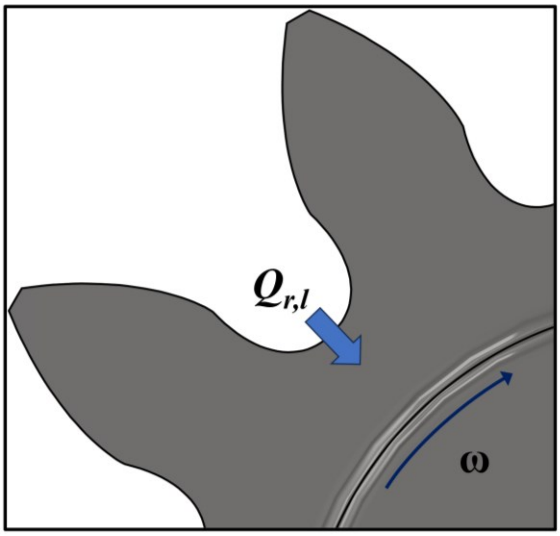

Figure 6 - Radial tooth leakage flow rate.

The following schematic (Figure 7) summarizes the different CVs and the connections between them identified and modeled for the lumped parameter approach model developed in this work.

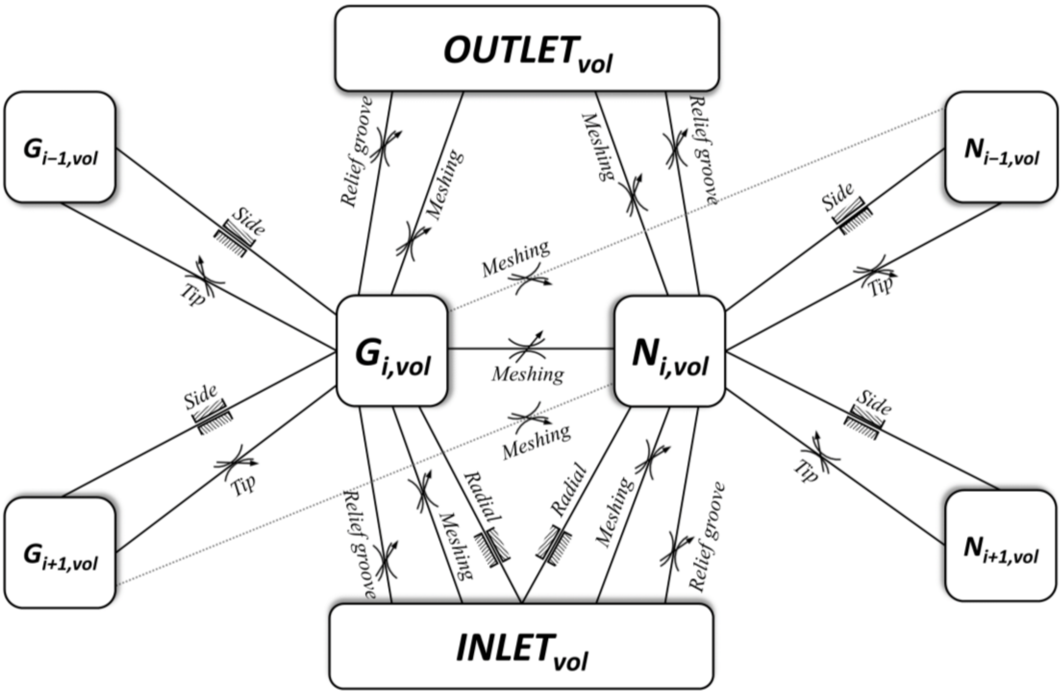

Figure 7 - Overview schematic of the lumped parameter approach model.

III.2. The EgeMATor MP+ Tool

The will to improve the noise performances of EGMs pushed to the creation of a tool that allowed to analyze but more importantly to optimize them obtaining certified results without the need to prototype the modification and then run a noise experimental campaign to validate the changes, permitting thus to save a lot of economic and time resources.

The tool was developed after the initial work by the Fluid Power Research Group of the Industrial Engineering department of the Federico II University of Naples that explored the numerical simulation of EGPs [21]. The previous work produced a lumped parameter model to analyze the fluid-dynamics performances of spur gears EGPs only. The main objective of this Ph.D. thesis was to further develop and refine the model created, expanding the analysis to different tooth profiles and to integrate it into a tool that also allowed the implementation of optimization procedures. The results of this development will be deeply detailed in the following sections.

III.2.1. EgeMATor MP+: General Description

EgeMATor MP+ (External Gear Machine Multi Tool Simulator for Multiple Gears' Profiles) is the developed tool from scratch based on the lumped parameter approach.

It permits simulating pumps with both traditional spur gears and helical gears profiles. The tool is comprised of various subroutines developed in different environments, interconnected to each other, as apparent from its workflow presented in Figure 8, to study and analyze the EGMs in depth.

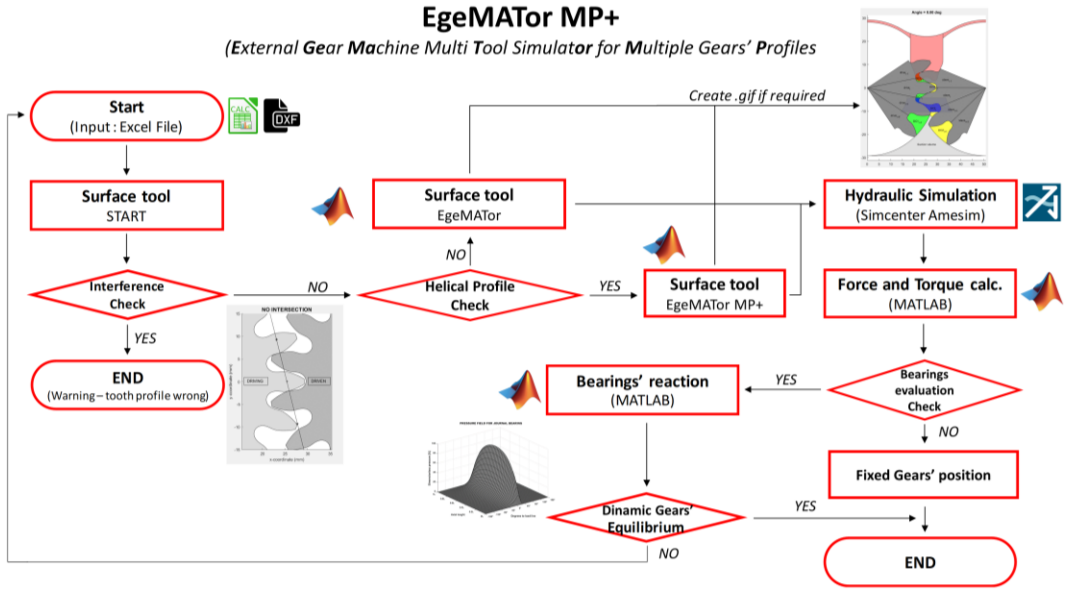

Figure 8 - EgeMATor MP+ workflow diagram.

Following the chart in Figure 8, the tool's workflow starts loading an excel file containing all the pump geometrical properties of the pump analyzed. This file also contains the links to the DXF files (Drawing Exchange Format) of tooth profiles and relief groove geometries. This data is acquired by the first subroutine developed so-called Surface Tool© which is the core of EgeMATor MP+. This subroutine, written in the MATLAB® (MathWorks Inc., Natick, Massachusetts, USA) environments, recreates a simplified 2D version of the EGM to execute checks on the physical feasibility of the inputted data and to extract the information required to the following subroutines. Initially, it verifies the correctness of the gear engagement with the chosen inputs, finding the relative rotation angle to obtain teeth contact with zero gaps and checking the presence of interference in the meshing zone. In case of interference, the tool produces a warning, stopping the procedure; otherwise, it moves to the next step where a check of the gears' profile typology is executed. In case of spur gears' typology, the tool proceeds with the standard subroutine, generating all the required data and files needed by the lumped parameter model and the subsequent hydraulic simulation; while, if gears' typology is helical, the tool activated a modified subroutine to consider the profile shifting along the axial dimension.

After the correct required subroutine completed, the next subroutine starts, that is the hydraulic simulation. This subroutine was developed in the Simcenter Amesim® environment (Siemens AG, Munich; Germany). It loads the files, generated by the Surface Tool, and runs a numerical simulation of the pump that evaluates the pressure and the volumetric fluxes for each of the CVs and connections modeled in the lumped parameters approach adopted. These values are then gathered in table files to be post-processed or used by the following subroutines.

The following subroutine is responsible for evaluating the mechanical characteristics of the pump. This subroutine is also written in MATLAB® environment and starts by loading the tables created by both the Surface Tool and the hydraulic simulation. From the first one it recovers geometrical data, CVs and connections values function of the rotation angle; from the latter, it extracts the fluid-dynamics properties of the aforementioned CVs. Using these data coupled with specific equations, it permits the evaluation of forces and torques acting on the pump's gears. This evaluation also considers the contribution of the friction forces due to the leakages and the contact forces due to the gears' meshing.

The final subroutine of the EgeMATor MP+ tool is tightly related to the previous one and enables the evaluation of the gears' micromotions. bearings' reactions. This subroutine was also written in the MATLAB® environment. It evaluates the bearings' reactions to extract the gears' micromotions. This subroutine starts with loading the geometrical data of the bearings from the initial excel file, while the load applied on them is obtained from the force and torque subroutine previously described. The code resolves the pressure film around the bearings through a finite difference method and computes the reaction to counterbalance the load applied on them. The eccentricity and the angle of minimum film thickness values are found through an iterative inverse procedure.

EgeMATor MP+ works in a closed loop; after the evaluation of the gears' micromotions thanks to the bearing subroutine, the obtained center gears' coordinates are compared with the initial chosen one. If the comparison results in a different position, the tool begins a new iteration, restarting from the Surface Tool subroutine. The closed loop continues until a convergence is reached. An additional check before the last subroutine was added to allow the simulation in a fixed gears' position. Therefore, at the "bearing evaluation check" state, in case of dynamic gears' position, EgeMATor MP+ evaluates the bearings' reaction with its closed loop; in case of fixed gears' position, the evaluation of the bearings' reaction is excluded, leading directly to termination.

A simulation for a chosen working condition requires small computational power and time. On a standard notebook equipped with an Intel® Core® CPU i7-8750H @ 2.20 GHz with 32 GB of RAM a complete simulation with a saving delta angle $\Delta\varphi$, that is the shaft angle difference for two consecutive points saved by the Surface Tool and the hydraulic simulation requires about 45 minutes to complete.

In the next section will be provided more information for each subroutine.

III.2.2. The Surface Tool©

The Surface Tool© is the core part of the developed lumped parametric tool. It is set up through reading an excel file containing all the geometrical information about the pump to be analyzed, such as number of teeth, gears' center to center distance, axial width, gears' module, etc. Additionally, the excel file also includes the path of the folder containing the drawings of tooth profile and wear-plates relief groove geometries. The drawings are stored as DXF files (Drawing Exchange format), and they can be extracted directly from the pump's CAD model or from experimental measurements. After loading the pump's geometrical characteristics, the Surface Tool© inspects the gears' engagement to check for the presence of any interference in the meshing zone with the inputted data. In case it found interference, the tool provides a warning, terminating its execution; otherwise, it continues the execution of its code.

Immediately after this first check, the Surface Tool executes another control to check the typology of the gears to analyze. In case of spur gears, the tool proceeds with the standard subroutine, evaluating the volumes of the CVs and the cross-sectional areas of their connections as a function of the rotational angle, generating thus all the required data and files needed by the lumped parameter model and the subsequent hydraulic simulation.

In case of helical gears, after the same evaluation done for the previous case, the tool activates a modified subroutine to take into consideration the profile shifting along the axial dimension.

The modified subroutine subdivides the gears into a series of slices, with a limited axial extension, and each slice is shifted of a certain degree compared to the others to replicate the helical axial shifting, as showed in Figure 9.

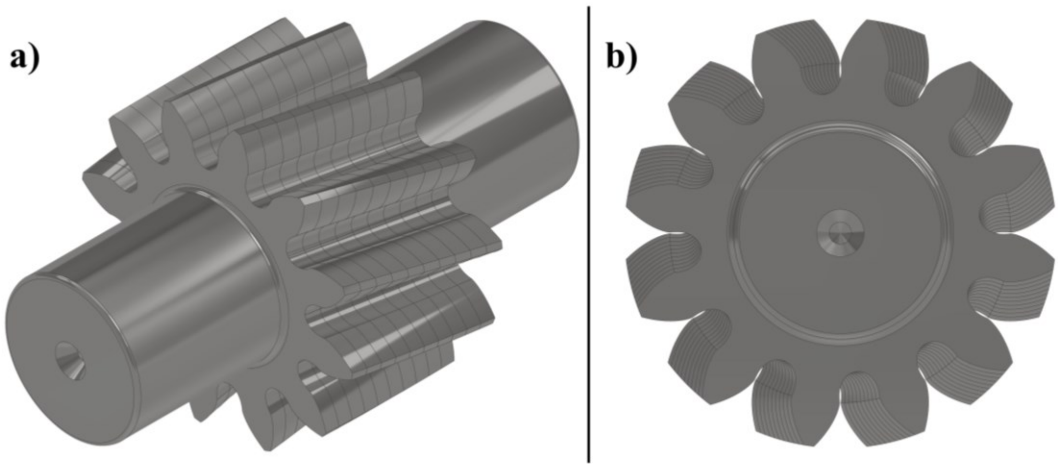

Figure 9 - Surface Tool for helical gear slicing procedure: a) 3D view; b) lateral view.

The relation between the slice axial extension (*Δz*) and its angular shift (*Δφ*) against a reference slice is the following:

$$\Delta z = \frac{b}{\beta}\,\Delta\varphi \qquad (9)$$

where b is the axial length of the gears and β is the total helical angle. Each slice is assumed to be as a spur gear. After imposing one of the gear's faces as a reference surface, for each slice the standard subroutine is executed with a rotating angle that is controlled by the Equation 10:

$$\varphi_i = \varphi_{ref} + \Delta\varphi\, k_i \tag{10}$$

where φ_i is the effective rotating shaft angle for the *i-th* slice, φ_{ref} is the rotating shaft angle of the face's surface chosen as reference, and k_i is an indicator to consider the cardinality of the slices.

The total values of the geometric characteristics of the pump analyzed (e.g., the volume of the displacement chamber) are achieved by integrating the values of all the slices considered:

$$V = \int_{z_1}^{z_2} A dz = \frac{b}{\beta}\int_{\varphi_1}^{\varphi_2} A(\varphi) d\varphi \tag{11}$$

where the z_1 and z_2 are respectively the top and bottom surfaces of the gear; φ_1 and φ_2 are their respective profile angle on the area curve, and the function $A(\varphi)$ is the area curve, that could represent a displacement area or a variable area.

Other than the geometrical data and drawings of the pump, the Surface Tool© requires another parameter to be set to properly function; that is the "*saving delta angle*" $\Delta\varphi$ that needs to be correctly chosen to obtain a robust and accurate hydraulic simulation. In fact, the tool produces a batch of data table files where a series of $[\varphi, g]$ couple are stored, being g an evaluated dimension function of the rotational angle φ.

This clarify why the value definition of the "*saving delta angle*" ($\Delta\varphi = \varphi_{i+1} - \varphi_i$) is of the utmost importance; a bigger $\Delta\varphi$ will speed up the *Surface Tool* subroutine but provide less accuracy with the possibility of losing information; with a smaller $\Delta\varphi$, the subroutine will require more computational resources and time to complete but will provide higher accuracy. This aspect is more crucial in the case of helical gears' pump due to this value being responsible to evaluate for the total number of slices considered and their effective axial extension Δz. To minimize the slices' axial extension, small values of the "*saving delta angle*" are required. During the analysis carried out for this work, it was found that a "*saving delta angle*" $\Delta\varphi = 0.25$ deg allows to obtain a good compromise between the computational resources required and the accuracy obtained.

After the interference and gears' geometry checks were successfully executed, the Surface Tool starts an automatic iterative procedure to find the rotational angle value required to put into contact the two gears. Following this iterative procedure, the subroutine finishes its executions creating the data required for the following subroutines of the lumped parameter model. Specifically, it saves around 100 table data files where every evaluated physical dimension, such as the value of the CV of the displacement chamber G_i (Driving gear) and N_i (Driven gear) or rather the cross-sectional area of their connection with the wear-plate pressure relief grooves as a function of the angular position, as plotted in the Figure 10.

Finally, to help visualizing the mesh and morphology of the CVs of the displacement chambers and their principal connection, the Surface

Tool© can optionally generate a GIF animation (Graphics Interchange Format) of the pump's gear meshing.

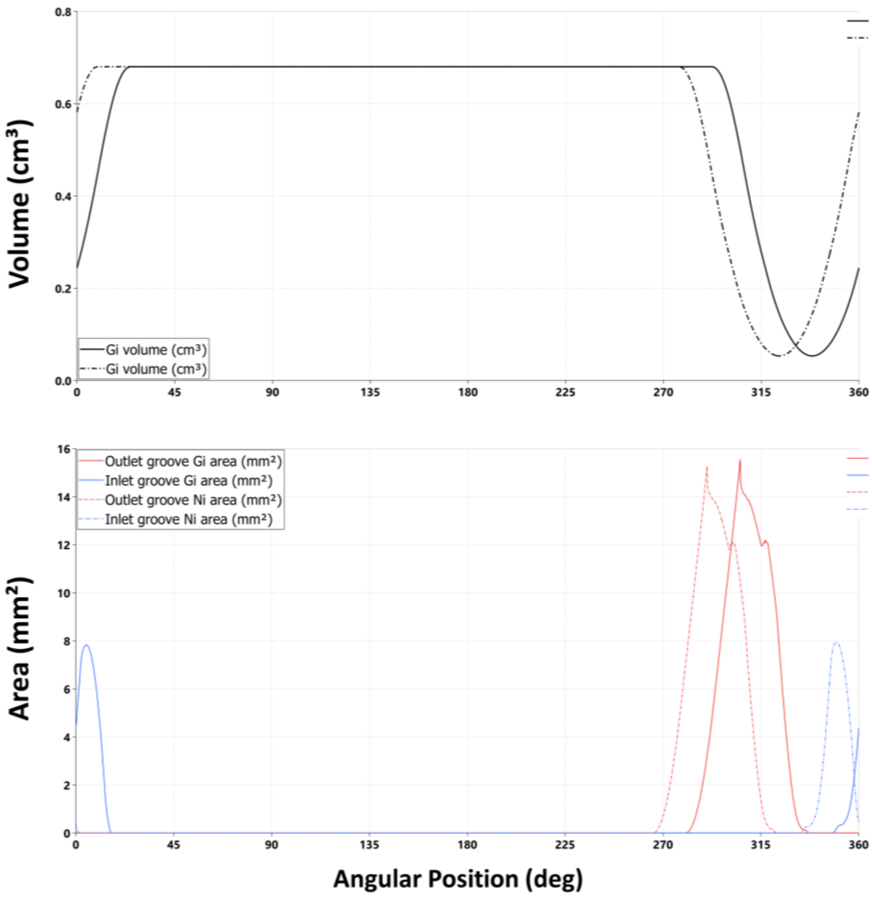

Figure 10 - Plot of some of the output of the Surface Tool.

Figure 11 shows two frames of an example of the outputted animation for two different angular positions where it can be seen some of the morphology that the displacement chambers and the internal connections can take during the meshing.

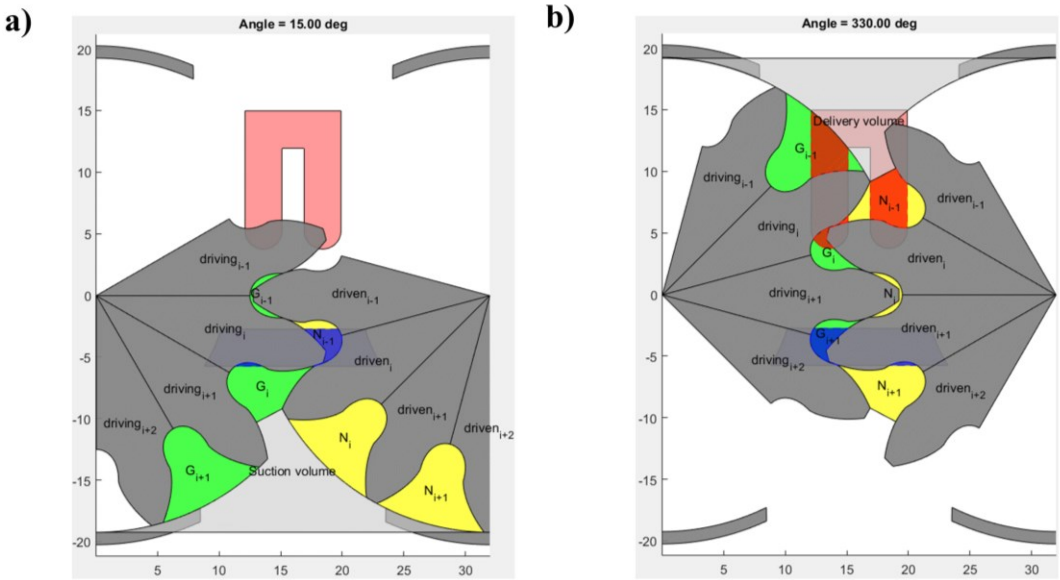

Figure 11 - Frames example extracted from GIF animation: a) 15 deg of angular position; b) 330 deg of angular position.

III.2.3. The Hydraulic Simulation Model

The hydraulic simulation subroutine, visible in Figure 12, is developed in the environment Simcenter Amesim® (Siemens AG, Munich; Germany). It loads the table data files generated by the Surface Tool and runs a numerical simulation of the pump. The model implements a large number of vectorized elements that allows the numerical model to automatically adapt to different typology of EGPs (such as EGPs with different number of teeth) without the needs to modify the model. Moreover, the employment of this type of element permits to optimize the computational resources required and thus reduce the time for the simulation to complete.

The hydraulic simulation evaluates the pressure and the volumetric fluxes for each of the CVs and connections modeled in the lumped parameters approach adopted. These values along other fluid properties are then gathered in table data files to be post-processed and to be used as required input by the following subroutines that are focused on the force and torque calculations.

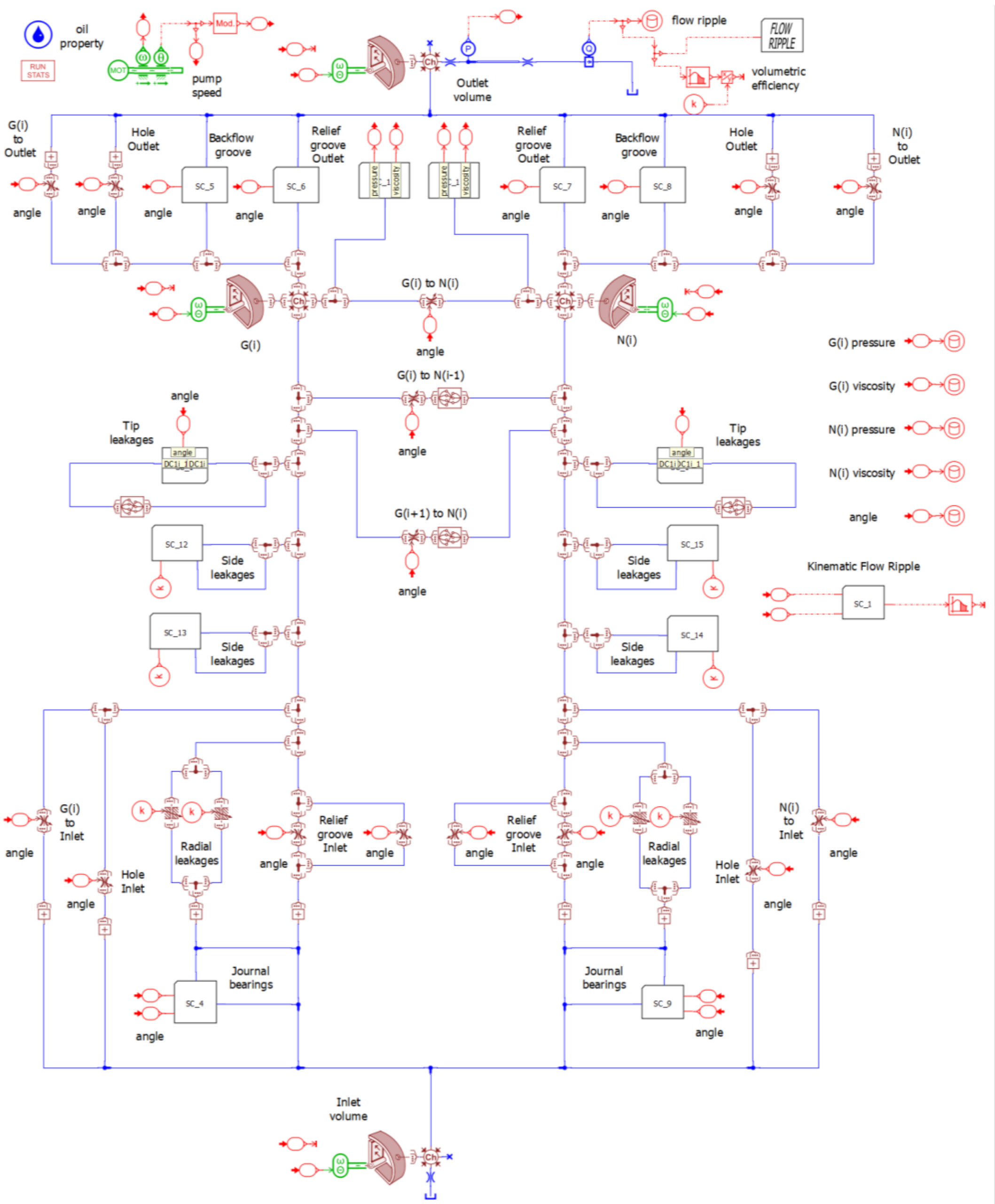

Figure 12 - Hydraulic simulation model overview.

III.2.4. The Force and Torque Calculation's Subroutine

The force and torque calculation's subroutine is responsible for evaluating the mechanical characteristics of the pump. This subroutine was also written in MATLAB® environment and loads table data files created by both the Surface Tool and the hydraulic simulation. Therefore, it obtains geometrical data, CVs and connections values function of the rotation angle; from the latter, it extracts the fluid-dynamics properties of the aforementioned CVs, permitting thus the evaluation of forces and torques acting on the pump's gears. This evaluation considers the contribution of the friction forces due to the leakages and the contact forces due to the gears' meshing.

In the next sections, a description of the methodology and the equations employed for the evaluation of both forces and torque acting on the pump's gears will be provided.

III.2.4.1. Torque Evaluation

The total torque required to supply to the pump' shaft to maintain it in a specific working condition is the sum of different contributions:

$$M_{tot} = M_G + M_N + M_{EHL} + M_{bear} + M_{churn,loss} \tag{12}$$

Where:

- M_G and M_N are the moments acting respectively on driving and driven gears due to pressure forces and internal friction;

- M_{EHL} is the moment due to friction force in the elastohydrodynamic lubrication [34] due to the teeth contact in the meshing zone;
- M_{bear} is the moment due to the viscous friction in the bearings;
- $M_{churn,loss}$ is the moment due to the churning losses.

The moments acting on the gear, M_G and M_N, were evaluated as a sum of different contribution:

$$M_G = M_{p,G} + M_{tl,G} + M_{sl,G} + M_{rl,G}$$
$$M_N = M_{p,N} + M_{tl,N} + M_{sl,N} + M_{rl,N} \tag{13}$$

where M_p is the moment of the pressure forces, M_{tl} is the moment of the friction forces due to the tip leakages, M_{sl} is the moment of the friction forces due to leakages over the side of a tooth, and M_{rl} is the moment of the friction forces due to the radial leakages.

III.2.4.1.1. Pressure Forces' Moment Evaluation: M_p

The pressure forces' moment of a displacement chamber is generated in the meshing zone, where the deformation of the CV creates pressure force not directed towards the radial direction of the gear. This is the case for both spur gears and helical gears typology, with the latter differing to the spur gear case for the resulting pressure forces being normal to both the tooth surface and the helical angle.

In the meshing zone, the interaction between two consecutive teeth of each gear determines the division of the CV in three different area with three different pressures, as visible from Figure 13 and Figure 70, where the three pressure forces for each teeth cavity have been presented for the driving and driven gears. Even the three zones red, blue, and green (later called R, B, and G) are showed and used as a reference.

Therefore, the surface corresponding to each area's tooth profile was projected on planes parallel to the reference system's axes. In first approximation, the pressure forces are supposed to be applied to the profile projections' center. In this way, the evaluation of these moments was obtained through linear equations that require, besides the pressure forces' values, distance values easily obtainable by the Surface Tool©.

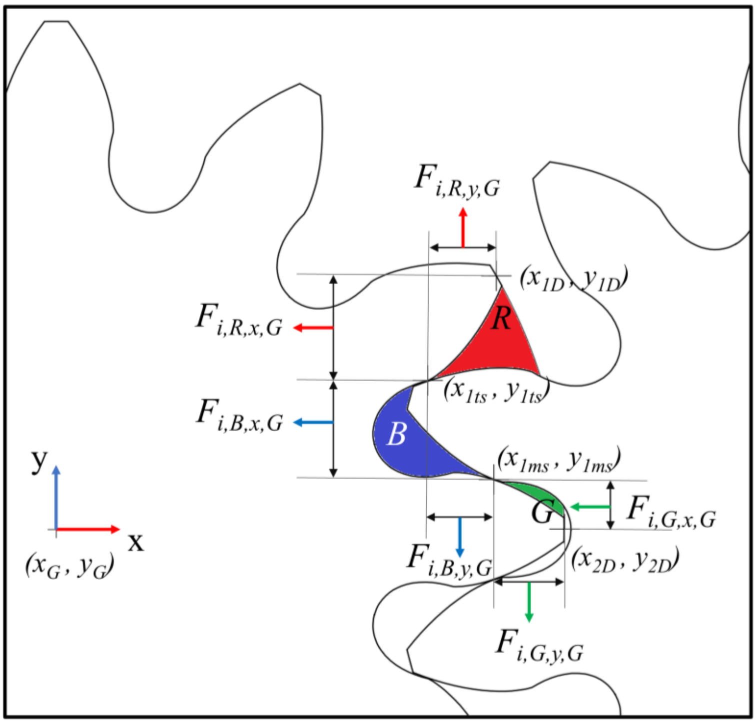

Figure 13 - Pressure forces schematization in the meshing zone for driving gear.

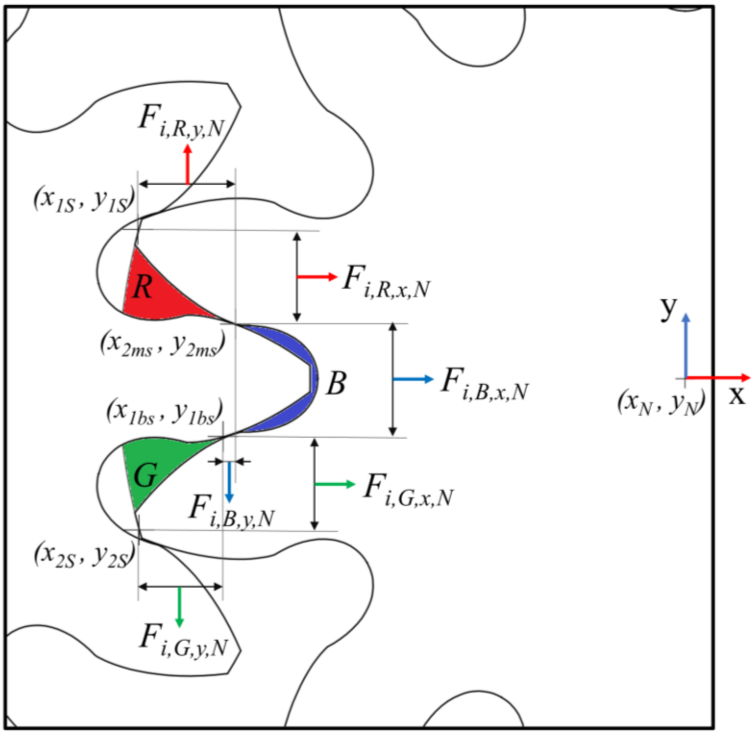

Figure 14 - Pressure forces schematization in the meshing zone for driven gear.

Thus, the moment generated by the pressure forces for the driving and driven gears is the sum of the following components:

$$M_{p,G} = \sum_{z} \left(M_{i,R,x,G} + M_{i,B,x,G} + M_{i,G,x,G} + M_{i,R,y,G} + M_{i,B,y,G} + M_{i,G,y,G} \right)$$

$$M_{p,N} = \sum_{z} \left(M_{i,R,x,N} + M_{i,B,x,N} + M_{i,G,x,N} + M_{i,R,y,N} + M_{i,B,y,N} + M_{i,G,y,N} \right) \tag{14}$$

where the moments of each zone for the driving gear was evaluated using the equations reported as follow:

- *Red Zone:*

$$M_{i,R,x,G} = -F_{i,R,x,G} \cdot \left[\frac{|y_{1D} + y_{1ts}|}{2} - y_G\right] \cdot sign\left[\frac{(y_{1D} + y_{1ts})}{2} - y_G\right]$$

(15)

$$M_{i,R,y,G} = F_{i,R,y,G} \cdot \left[\frac{|x_{1D} + x_{1ts}|}{2} - x_G\right]$$

- *Blue Zone:*

$$M_{i,B,x,G} = -F_{i,B,x,G} \cdot \left[\frac{|y_{1ts} + y_{1ms}|}{2} - y_G\right] \cdot sign\left[\frac{(y_{1ts} + y_{1ms})}{2} - y_G\right]$$

(16)

$$M_{i,R,y,G} = F_{i,B,y,G} \cdot \left[\frac{|x_{1ts} + x_{1ms}|}{2} - x_G\right]$$

- *Green Zone:*

$$M_{i,G,x,G} = -F_{i,G,x,G} \cdot \left[\frac{|y_{1ms} + y_{2D}|}{2} - y_G\right] \cdot sign\left[\frac{(y_{1ms} + y_{2D})}{2} - y_G\right]$$

(17)

$$M_{i,G,y,G} = F_{i,G,y,G} \cdot \left[\frac{|x_{1ms} + x_{2D}|}{2} - x_G\right]$$

The moments of each zone for the driven gear were evaluated using the same methodology and system reference, obtaining thus the following equations:

- *Red Zone:*

$$M_{i,R,x,N} = -F_{i,R,x,N} \cdot \left[\frac{|y_{1S} + y_{2ms}|}{2} - y_N\right] \cdot sign\left[\frac{(y_{1S} + y_{2ms})}{2} - y_N\right]$$

$$M_{i,R,y,N} = F_{i,R,y,N} \cdot \left[\frac{|x_{1S} + x_{2ms}|}{2} - x_N\right] \tag{18}$$

- *Blue Zone:*

$$M_{i,B,x,N} = -F_{i,B,x,N} \cdot \left[\frac{|y_{2ms} + y_{2bs}|}{2} - y_N\right] \cdot sign\left[\frac{(y_{2ms} + y_{2bs})}{2} - y_N\right]$$

$$M_{i,R,y,N} = F_{i,B,y,N} \cdot \left[\frac{|x_{2ms} + x_{2bs}|}{2} - x_N\right] \tag{19}$$

- *Green Zone:*

$$M_{i,G,x,N} = -F_{i,G,x,N} \cdot \left[\frac{|y_{2S} + y_{2bs}|}{2} - y_N\right] \cdot sign\left[\frac{(y_{2S} + y_{2bs})}{2} - y_N\right]$$

$$M_{i,G,y,N} = F_{i,G,y,N} \cdot \left[\frac{|x_{2S} + x_{2bs}|}{2} - x_N\right] \tag{20}$$

The dimensions x_G, y_G, x_N and y_N found in the equations (15) - (20) are the coordinates along the chosen x and y axes of the center of rotation of the driving gear and the driven gear. The other coordinates are relative to the points displayed indicated in Figure 13 and Figure 14.

In case of helical gears, the equations (15) - (20) are still valid for each slice on which the gears were divided due to the "*slice methodology*" implemented in the Surface Tool©. The total moments for each of the three zone for each gear is obtained then through an integration along the axial dimension, which is along the helical angle. So, for each of the moments already described, the following relation is always valid in case of helical EGP:

$$M_{g,helical} = \int_{z_1}^{z_2} M_g dz = \frac{b}{\beta}\int_{\varphi_1}^{\varphi_2} M_g(\varphi) d\varphi \tag{21}$$

where $M_{g,helical}$ is the generic moments evaluated in case of helical gears and M_g is one of the moments described in the equations (15) - (20).

III.2.4.1.2. Pressure Forces' Evaluation in the Meshing Zone

To complete the description of the evaluation of the moment due to the pressure forces, it is necessary describe the method use to evaluate these forces. The instantaneous pressure forces utilized in the equations (15) - (20) were obtained through linear equations that require, besides the values of instantaneous pressure, constant in all the CV due to the lumped parameter approach implemented, distance values that represent the surface corresponding to each area's tooth profile projected on planes parallel to the reference system's axes. These distances were calculated by the Surface Tool©.

With reference to Figure 13 and Figure 14, the pressure forces in the meshing zone in the subdivided zone were evaluated as follow:

- *Red Zone:*

$$F_{i,R,x,G} = -\cos\beta \cdot p_{i-1,N} \cdot [b\,|y_{1D} - y_{1ts}|]$$
$$F_{i,R,y,G} = \cos\beta \cdot p_{i-1,N} \cdot [b\,|x_{1D} - y_{1ts}|] \tag{22}$$

- *Blue Zone:*

$$F_{i,B,x,G} = -\cos\beta \cdot p_{i,G} \cdot [b\,|y_{1ts} - y_{1ms}|]$$
$$F_{i,B,y,G} = \cos\beta \cdot p_{i,G} \cdot [b\,|x_{1ms} - x_{1ts}|] \cdot sign(x_{1ts} - x_{1ms}) \tag{23}$$

- *Green Zone:*

$$F_{i,G,x,G} = -\cos\beta \cdot p_{i,N} \cdot [b\,|y_{1ms} - y_{2D}|]$$

$$F_{i,G,y,G} = -\cos\beta \cdot p_{i,N} \cdot [b\,|x_{1ms} - x_{2D}|] \tag{24}$$

These equations were referred to the driving gear. For the driven gear, the pressure forces are evaluated as follows:

- *Red Zone:*

$$F_{i,R,x,N} = \cos\beta \cdot p_{i,G} \cdot [b\,|y_{1S} - y_{2ms}|]$$

$$F_{i,R,y,N} = \cos\beta \cdot p_{i,G} \cdot [b\,|x_{1S} - y_{2ms}|] \tag{25}$$

- *Blue Zone:*

$$F_{i,B,x,G} = \cos\beta \cdot p_{i,N} \cdot [b\,|y_{2ms} - y_{2bs}|]$$

$$F_{i,B,y,G} = \cos\beta \cdot p_{i,N} \cdot [b\,|x_{2ms} - x_{2bs}|] \cdot sign(x_{2bs} - x_{2ms}) \tag{26}$$

- *Green Zone:*

$$F_{i,G,x,G} = \cos\beta \cdot p_{i+1,G} \cdot [b\,|y_{2bs} - y_{2S}|]$$

$$F_{i,G,y,G} = -\cos\beta \cdot p_{i+1,G} \cdot [b\,|x_{2bs} - x_{2S}|] \quad (27)$$

Equations (22) – (27) all contains the term $cos\ \beta$ to encompass the needs of the resulting forces to be also normal to the helical angle in case of helical gear. In fact, in case of spur gears, the helical angle β would be equal to zero and so the term would reduce to the unity, not altering the pressure force values.

In case of helical gear, the equations (22) - (27) also need to be executed through the "*slice methodology*" implemented in the Surface Tool©. The total pressure forces for each of the three zone for each gear is obtained through the same integration described previously, obtaining the following relation for helical EGP:

$$F_{p,g,helical} = \int_{z_1}^{z_2} F_{p,g}\,dz = \frac{b}{\beta}\int_{\varphi_1}^{\varphi_2} F_{p,g}(\varphi)\,d\varphi \quad (28)$$

where $F_{pg,helical}$ is the generic pressure force evaluated in case of helical gears and $F_{p,g}$ is one of the pressure forces described in the equations (22) - (27).

III.2.4.1.3. Tip Leakages' Moment Evaluation: M_{tl}

Viscous friction forces on the tooth tip were evaluated with the leakage's shear stress integration on the tip's surface. Since the flow of this type of leakage was modeled as a sum of the Couette and Poiseuille effects, the shear stress was modeled as follows:

$$\tau_{i,tl} = \frac{h_{tip}}{2}\frac{\Delta p}{l_{tip}} - \frac{\mu\omega R_{mj}}{h_{tip}} \tag{29}$$

where R_{mj} is the gear's major radius, corresponding to the distance of tooth's tip from the gear center, as defined in Figure 15.

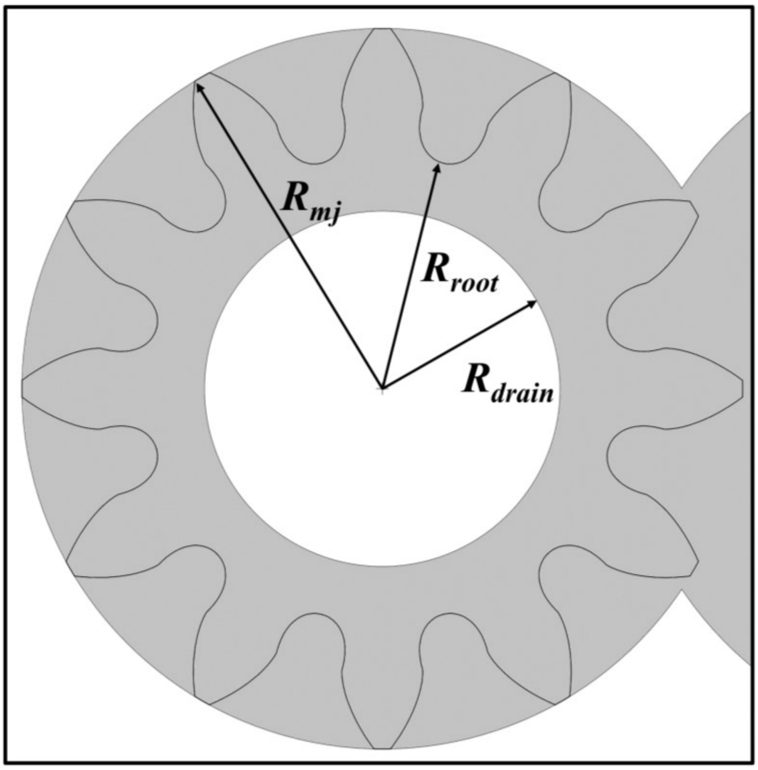

Figure 15 - Definition of R_{mj}, R_{root} and R_{drain} for friction moments evaluation.

The friction force acting on the tooth's tip surface due to the Couette-Poiseuille flow for each gear were thus evaluated as follow:

$$F_{i,tl,G} = b \cdot \tau_{i,tl,G} \cdot l_{tip}$$
$$F_{i,tl,N} = b \cdot \tau_{i,tl,N} \cdot l_{tip} \tag{30}$$

The friction moment produced on each gear by these forces are expressed by the following equations:

$$M_{tl,G} = \sum_{z} F_{i,tl,G} \cdot R_{mj}$$
$$M_{tl,N} = \sum_{z} F_{i,tl,N} \cdot R_{mj} \tag{31}$$

In case of helical gear, the only dimension that is function of the helical angle is the tooth's height gap h_{tip}, being R_{mj} and l_{tip} constant physical characteristics of the gears and the instantaneous pressure and viscosity values are constant along the CV being the model a lumped parameter one. The h_{tip} value is not constant also along the rotational angle due to pressure forces acting on the gears that shift them towards the inlet side, generating an eccentricity. For this reason, in case of helical gear pump, only the h_{tip} value needs to be integrated along the helical angle:

$$h_{tip,helical} = \int_{z_1}^{z_2} h_{tip} dz = \frac{b}{\beta} \int_{\varphi_1}^{\varphi_2} h_{tip}(\varphi) d\varphi \tag{32}$$

The new value obtained can thus be utilized in equation (29) to find the required shear stress for this type of gears.

III.2.4.1.4. Side Tooth Leakages' Moment Evaluation: M_{sl}

While for the evaluation of the side flow rate the Couette contribution was not considered due to the net result being zero, for the evaluation of the friction contributions it has to be evaluated due to the dependence from the viscosity of two different CV. For this reason, the shear stress to evaluate the friction moment due to the tooth side leakage for the *n-th* slice (Figure 5) was modeled as follow:

$$\tau_{n,i,sl} = \frac{h_{side}}{2}\frac{\Delta p}{l_{n,slice}} - \frac{\mu\omega R_{n,slice}}{h_{side}} \tag{33}$$

where $l_{n,slice}$ and $R_{n,slice}$ are the length and the radius of the *n-th* slice.

Thus, the friction forces for each tooth for each gear was:

$$F_{n,i,sl,G} = \int_{R_{n,slice}-\frac{b_{slice}}{2}}^{R_{n,slice}+\frac{b_{slice}}{2}} \left(\tau_{n,i,sl,G} \cdot l_{n,slice}\right) dR$$

$$F_{n,i,sl,N} = \int_{R_{n,slice}-\frac{b_{slice}}{2}}^{R_{n,slice}+\frac{b_{slice}}{2}} \left(\tau_{n,i,sl,N} \cdot l_{n,slice}\right) dR \tag{34}$$

where b_{slice} is the slice's height, chosen constant for all of them, as showed in Figure 5.

The friction moment due to the side leakages tooth friction forces for a single slice is equal to:

$$M_{n,i,sl,G} = F_{n,i,sl,G} \cdot R_{n,G}$$
$$M_{n,i,sl,N} = F_{n,i,sl,N} \cdot R_{n,N} \tag{35}$$

The total side leakages friction moment on a single tooth is:

$$M_{i,sl,G} = \sum_{n} M_{n,i,sl,G}$$
$$M_{i,sl,N} = \sum_{n} M_{n,i,sl,N} \tag{36}$$

Finally, the total friction moment acting on both sides gaps for each gear is equal to:

$$M_{sl,G} = 2 \cdot \sum_{z} M_{i,sl,G}$$
$$M_{sl,N} = 2 \cdot \sum_{z} M_{i,sl,N} \tag{37}$$

In case of helical gears, the tooth structure on the end faces of the gear is not affected, but only their positioning is offset by an angular value equal to β that, thanks to the homogeneous property inside of a CV due to the lumped parameter approach, does not affect the described methodology.

III.2.4.1.5. Radial Tooth Leakages' Moment Evaluation: M_{rl}

The pressure driven leakage flow (Poiseuille) component of the radial leakages is directed along the radial pump's direction. Thus, the shear stress due to this flow component does not generate any friction moment. The friction moment is then only due to the Couette type flow and the shear stress equation for a differential gear slice for a single CV (Figure 16) is:

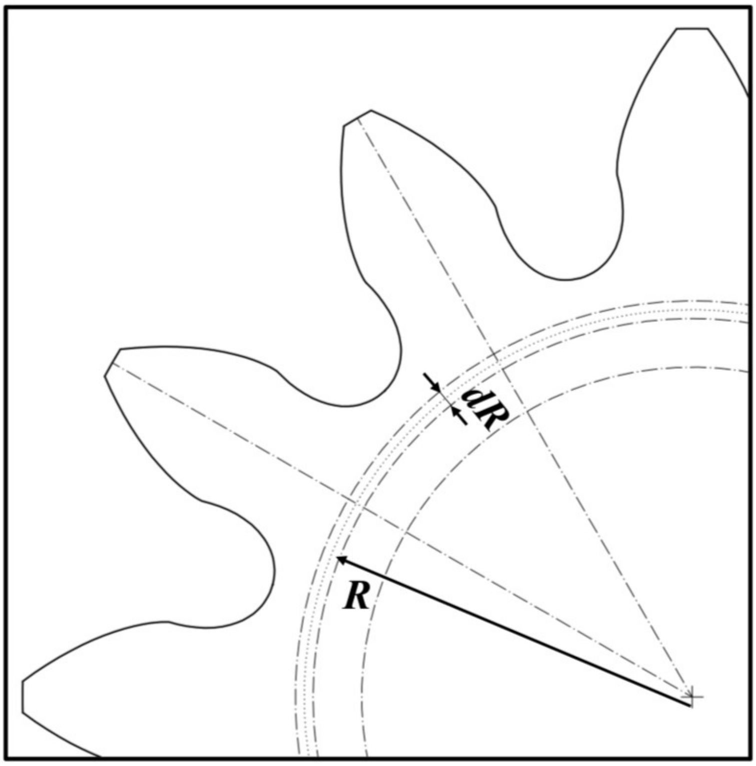

Figure 16 - Definition of the gear slice surface for the radial leakage friction moment evaluation.

$$\tau_{i,rl} = \frac{\mu\omega R}{h_{side}} \tag{38}$$

The friction forces generated by this shear stress for a single CV for each gear is then determined as:

$$F_{i,rl,G} = \int_{R_{drain}}^{R_{root}} \left(\tau_{i,rl,G} \cdot \frac{2\pi R}{z}\right) dR$$

$$F_{i,rl,N} = \int_{R_{drain}}^{R_{root}} \left(\tau_{i,rl,N} \cdot \frac{2\pi R}{z}\right) dR \tag{39}$$

The corresponding friction moment is then:

$$M_{i,rl,G} = F_{i,rl,G} \cdot \left(\frac{R_{root} + R_{drain}}{2}\right)$$

$$M_{i,rl,N} = F_{i,rl,N} \cdot \left(\frac{R_{root} + R_{drain}}{2}\right) \tag{40}$$

Therefore, considering the two face surfaces of the gears, the total friction moment due to the radial tooth leakages were defined as:

$$M_{rl,G} = 2 \cdot \sum_{z} M_{i,rl,G}$$

$$M_{rl,N} = 2 \cdot \sum_{z} M_{i,rl,N} \tag{41}$$

In case of helical gears, the same stated observations done for the side leakages are still valid, so the presence of the helical angle β does not influence the described methodology.

The moments M_{EHL}, M_{bear} and $M_{churn,loss}$, although they provide a non-zero contribution, their magnitude is significantly lower than of the other contribution and for this reason it was decided that they would be neglected in this study.

III.2.4.2. Forces Evaluation

An analysis on the forces acting on each gear during the rotation were also carried out. On each gear, the resultant force applied is the sum of different type of forces:

$$F_{tot,G} = F_{p,tot,G} + F_{tl,G} + F_{sl,G} + F_{rl,G} + F_{cont,G}$$

$$F_{tot,N} = F_{p,tot,N} + F_{tl,N} + F_{sl,N} + F_{rl,N} + F_{cont,N} \tag{42}$$

where $F_{p,tot}$ are the pressure forces, F_{tl} are the friction forces due to the tip leakages, F_{sl} are the friction forces due to side tooth's leakages, F_{rl} are the friction forces due to the radial leakages and F_{cont} are the contact force's reactions between the gears.

For the pressure forces $F_{p,tot}$, the total contribution on each gear is the sum of the pressure forces during the meshing zone and outside the meshing zone:

$$F_{p,tot,G} = \sum_{z} \left(F_{i,nm,G} + F_{i,R,G} + F_{i,B,G} + F_{i,G,G}\right)$$
$$F_{p,tot,N} = \sum_{z} \left(F_{i,nm,N} + F_{i,R,N} + F_{i,B,N} + F_{i,G,N}\right) \tag{43}$$

The pressure forces outside the meshing zone are showed in Figure 17 and Figure 18 respectively for the driving and driven gear.

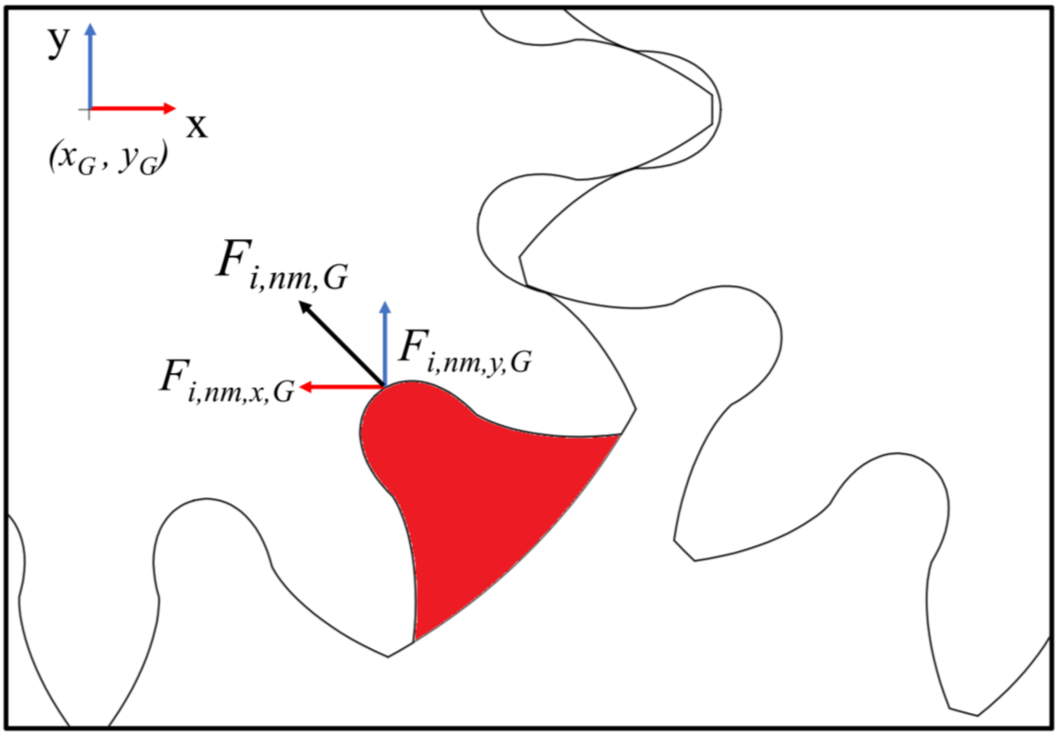

Figure 17 - Pressure forces in the non-meshing zone (Driving gear).

For the driving gear, the pressure forces outside the meshing zone projected along the x and y axis of the reference system of a single CV are expressed by the following equations:

$$F_{i,nm,x,G} = -\cos\beta \cdot F_{i,nm,G} \cdot \cos\left(\varphi + \frac{\pi}{z} + \varphi_0\right)$$
$$F_{i,nm,y,G} = \cos\beta \cdot F_{i,nm,G} \cdot \sin\left(\varphi + \frac{\pi}{z} + \varphi_0\right) \quad (44)$$

where φ_o is the phase angle of the *i-th* teeth compared to the reference coordinate system.

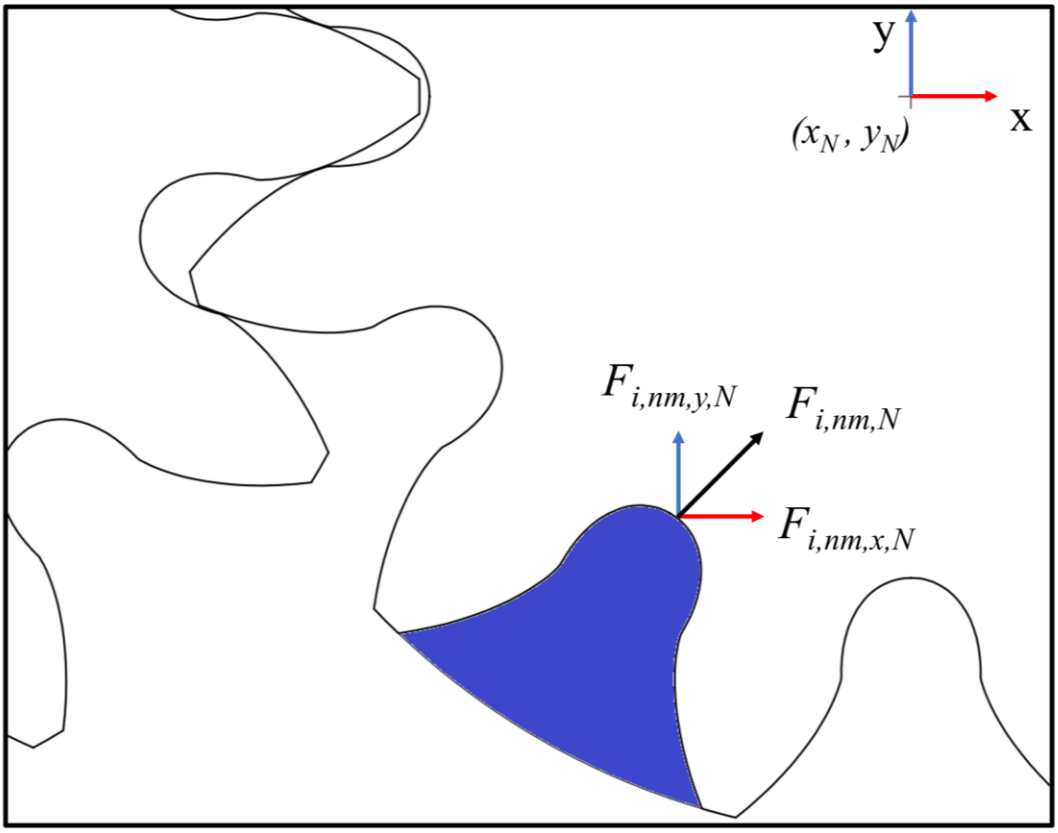

Figure 18 - Pressure forces in the non-meshing zone (Driven gear).

For the driven gear, the pressure forces outside the meshing zone projected along the x and y axis of the reference system of a single CV are instead expressed by the following equations:

$$F_{i,nm,x,N} = \cos\beta \cdot F_{i,nm,N} \cdot \cos\left(\varphi + \frac{2\pi}{z} - \alpha + \varphi_0\right)$$
$$F_{i,nm,y,N} = \cos\beta \cdot F_{i,nm,N} \cdot \sin\left(\varphi + \frac{2\pi}{z} - \alpha + \varphi_0\right) \tag{45}$$

where α is the angle to achieve contact between the *i-th* teeth of both gears.

Equations (43) – (45) all contains the term *cos β* to encompass the needs of the resulting forces to be also normal to the helical angle in case of helical gear. In fact, in case of spur gears, the helical angle β would be equal to zero and so the term would reduce to the unity, not altering the pressure force values.

Substituting the values of the pressure forces in the non-meshing area, equations (43) – (45) become:

$$F_{i,nm,x,G} = -\cos\beta \cdot p_{i,G} \cdot b \cdot \frac{2\pi}{z} \cdot \cos\left(\varphi + \frac{\pi}{z} + \varphi_0\right)$$
$$F_{i,nm,y,G} = \cos\beta \cdot p_{i,G} \cdot b \cdot \frac{2\pi}{z} \cdot \sin\left(\varphi + \frac{\pi}{z} + \varphi_0\right) \tag{46}$$

$$F_{i,nm,x,N} = \cos\beta \cdot p_{i,G} \cdot b \cdot \frac{2\pi}{z} \cdot \cos\left(\varphi + \frac{2\pi}{z} - \alpha + \varphi_0\right)$$

(47)

$$F_{i,nm,y,N} = \cos\beta \cdot p_{i,G} \cdot b \cdot \frac{2\pi}{z} \cdot \sin\left(\varphi + \frac{2\pi}{z} - \alpha + \varphi_0\right)$$

Finally, the component for the total pressure forces can be written as follow:

$$F_{p,tot,x,G} = \sum_z \left(F_{i,nm,x,G} + F_{i,R,x,G} + F_{i,B,x,G} + F_{i,G,x,G}\right)$$

(48)

$$F_{p,tot,y,G} = \sum_z \left(F_{i,nm,y,G} + F_{i,R,y,G} + F_{i,B,y,G} + F_{i,G,y,G}\right)$$

$$F_{p,tot,x,N} = \sum_z \left(F_{i,nm,x,N} + F_{i,R,x,N} + F_{i,B,x,N} + F_{i,G,x,N}\right)$$

(49)

$$F_{p,tot,y,N} = \sum_z \left(F_{i,nm,y,N} + F_{i,R,y,N} + F_{i,B,y,N} + F_{i,G,y,N}\right)$$

In case of helical gear, the same "*slice methodology*" used for the evaluation of the pressure forces inside the meshing zone need to be executed for equations (43) - (45). The total pressure forces outside the meshing zone for each gear is obtained through the same integration:

$$F_{nm,g,helical} = \int_{z_1}^{z_2} F_{nm,g} dz = \frac{b}{\beta} \int_{\varphi_1}^{\varphi_2} F_{nm,g}(\varphi) d\varphi \qquad (50)$$

where $F_{nm,g,helical}$ is the generic pressure force component evaluated in case of helical gears and $F_{p,g}$ is one of the pressure force components described in the equations (43) - (45).

Maintaining the same methodology for the other described forces, the components for the tooth tip leakages are:

$$F_{tl,x,G} = \sum_{z} \left(F_{i,tl,G} \cdot \sin\varphi \right)$$

$$F_{tl,y,G} = \sum_{z} \left(F_{i,tl,G} \cdot \cos\varphi \right) \tag{51}$$

$$F_{tl,x,N} = \sum_{z} \left(F_{i,tl,N} \cdot \sin\left(\varphi + \frac{2\pi}{z} - \alpha \right) \right)$$

$$F_{tl,y,N} = \sum_{z} \left(F_{i,tl,N} \cdot \cos\left(\varphi + \frac{2\pi}{z} - \alpha \right) \right) \tag{52}$$

The force components for the side tooth leakages are:

$$F_{sl,x,G} = 2 \cdot \sum_{z} \left(F_{i,sl,G} \cdot \sin\varphi \right)$$

$$F_{sl,y,G} = 2 \cdot \sum_{z} \left(F_{i,sl,G} \cdot \cos\varphi \right) \tag{53}$$

$$F_{sl,x,N} = -2 \cdot \sum_{z} \left(F_{i,sl,N} \cdot \sin\left(\varphi + \frac{2\pi}{z} - \alpha \right) \right)$$

$$F_{sl,y,N} = 2 \cdot \sum_{z} \left(F_{i,sl,N} \cdot \cos\left(\varphi + \frac{2\pi}{z} - \alpha \right) \right) \tag{54}$$

For the friction forces due to the radial leakages, the Couette component, while creating moment on the gear, the resultant friction force is zero due to the geometrical symmetry. The Poiseuille type flow component of this leakage, instead, while not generating any friction moment, it creates a friction force acting on the gear. The shear stress generated by this flow for a single CV on each gear is:

$$\tau_{i,rl} = \frac{h_{side}}{2} \frac{\left(p_i - p_{bearing} \right)}{l_{rd}} \tag{55}$$

where $p_{bearing}$ is the pressure inside the drain bushing channel and l_{rd} is defined as (Figure 15):

$$l_{rd} = \frac{\pi (R_{root} + R_{drain})}{z} \tag{56}$$

The friction force generated by this shear stress is equal to:

$$F_{i,rl,G} = \int_{R_{drain}}^{R_{root}} \left(\tau_{i,rl,G} \cdot l_{rd} \cdot \frac{2\pi}{z}\right) dR$$

$$F_{i,rl,N} = \int_{R_{drain}}^{R_{root}} \left(\tau_{i,rl,N} \cdot l_{rd} \cdot \frac{2\pi}{z}\right) dR \tag{57}$$

Thus, the components of the radial friction forces are:

$$F_{rl,x,G} = -2 \cdot \sum_{z} \left(F_{i,rl,G} \cdot \sin\left(\varphi + \frac{\pi}{z}\right)\right)$$

$$F_{rl,y,G} = 2 \cdot \sum_{z} \left(F_{i,rl,G} \cdot \cos\left(\varphi + \frac{\pi}{z}\right)\right) \tag{58}$$

$$F_{rl,x,N} = 2 \cdot \sum_{z} \left(F_{i,rl,N} \cdot \sin\left(\varphi + \frac{2\pi}{z} - \alpha\right)\right)$$

$$F_{rl,y,N} = 2 \cdot \sum_{z} \left(F_{i,rl,N} \cdot \cos\left(\varphi + \frac{2\pi}{z} - \alpha\right)\right) \tag{59}$$

III.2.4.2.1. Pressure Forces Evaluation in Case of Helical Gears

In case of helical gears, the helical angle causes the presence of non-zero components of the pressure forces along the axial direction of the pump. Outside the meshing zone, for every slice in which the gears' axial dimension is divided, the CV is loaded by a single uniform pressure value in the radial direction, thus the helical angle generates two equal but opposite forces along the axial dimension, resulting thus in a total net axial component equal to zero, as showed in Figure 19.

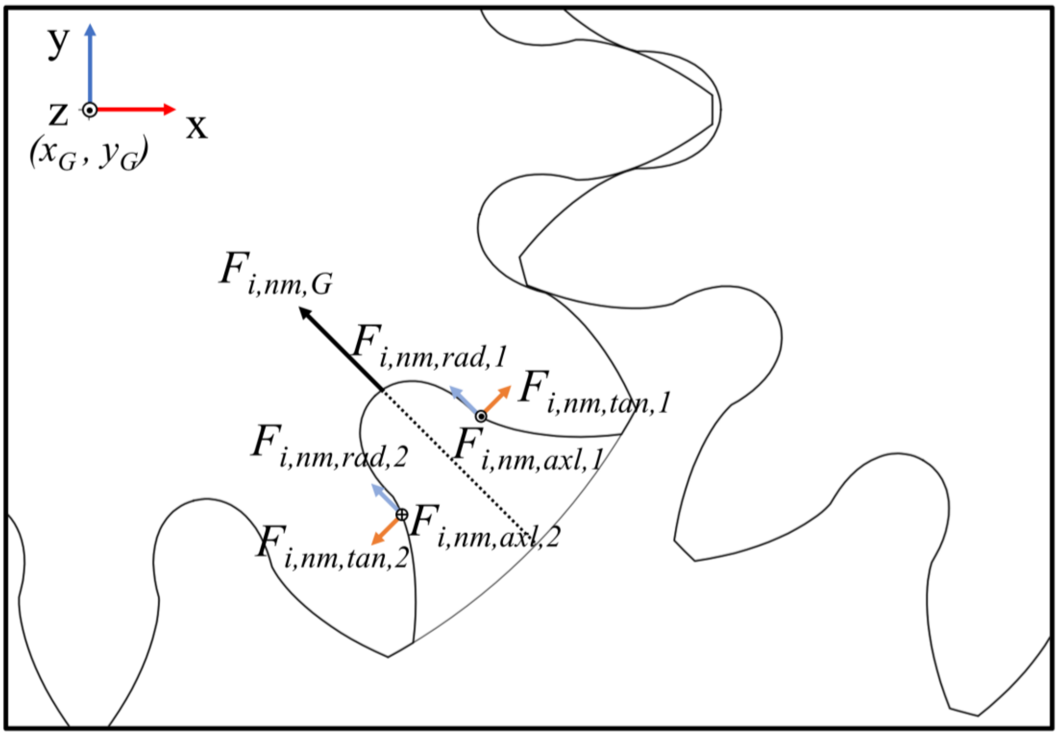

Figure 19 - Pressure forces in the non-meshing zone for helical gear.

Inside the meshing zone, since the CV is divided in three different areas with different pressure values, the axial pressure force component results unbalanced, creating thus the need to evaluate the pressure force also along the z axis of the reference system adopted.

Referencing to the Figure 13 and Figure 14, the resulting total pressure forces along the z axis for a single slice of each of the helical gear is the following:

$$F_{p,i,k,z,G} = -\tan\beta \cdot \left[F_{i,k,R,x,G} \cdot sign\left[\frac{(y_{1D} + y_{1ts})}{2} - y_G\right] + F_{i,k,R,y,G} + F_{i,k,B,x,G} \cdot sign\left[\frac{(y_{1ts} + y_{1ms})}{2} - y_G\right] + F_{i,k,B,y,G} \cdot sign(x_{1ts} - x_{1ms}) + F_{i,k,G,x,G} \cdot sign\left[\frac{(y_{1ms} + y_{2D})}{2} - y_G\right] + F_{i,k,G,y,G}\right]$$

(60)

$$F_{p,i,k,z,N} = \tan\beta \cdot \left[- F_{i,k,R,x,N} \cdot sign\left[\frac{(y_{1S} + y_{2ms})}{2} - y_N\right] - F_{i,k,R,y,N} - F_{i,k,B,x,N} \cdot sign\left[\frac{(y_{2ms} + y_{2bs})}{2} - y_N\right] - F_{i,k,B,y,N} \cdot sign(x_{2bs} - x_{2ms}) - F_{i,k,G,x,N} \cdot sign\left[\frac{(y_{2bs} + y_{2S})}{2} - y_G\right] + F_{i,k,G,y,N}\right]$$

To obtain the pressure force component for a single tooth of each gear, the usual integration of the "*slice methodology*" was employed:

$$F_{p,i,z,G} = \int_{z_1}^{z_2} F_{p,i,k,z,G} dz = \frac{b}{\beta} \int_{\varphi_1}^{\varphi_2} F_{p,i,k,z,G}(\varphi) d\varphi$$

(61)

$$F_{p,i,z,G} = \int_{z_1}^{z_2} F_{p,i,k,z,G} dz = \frac{b}{\beta} \int_{\varphi_1}^{\varphi_2} F_{p,i,k,z,G}(\varphi) d\varphi$$

Finally, the total pressure force component along the z axis is:

$$F_{p,z,G} = \sum_{z} \left(F_{p,i,z,G}\right)$$
$$F_{p,z,N} = \sum_{z} \left(F_{p,i,z,N}\right) \tag{62}$$

III.2.4.2.2. Teeth Contact Force

The contact force F_{cont}, showed in Figure 20, is the force due to the contact between the gears during their meshing. This force is responsible for balancing the total moment on the driven gear acting along the line of contact of the coupled gears' teeth.

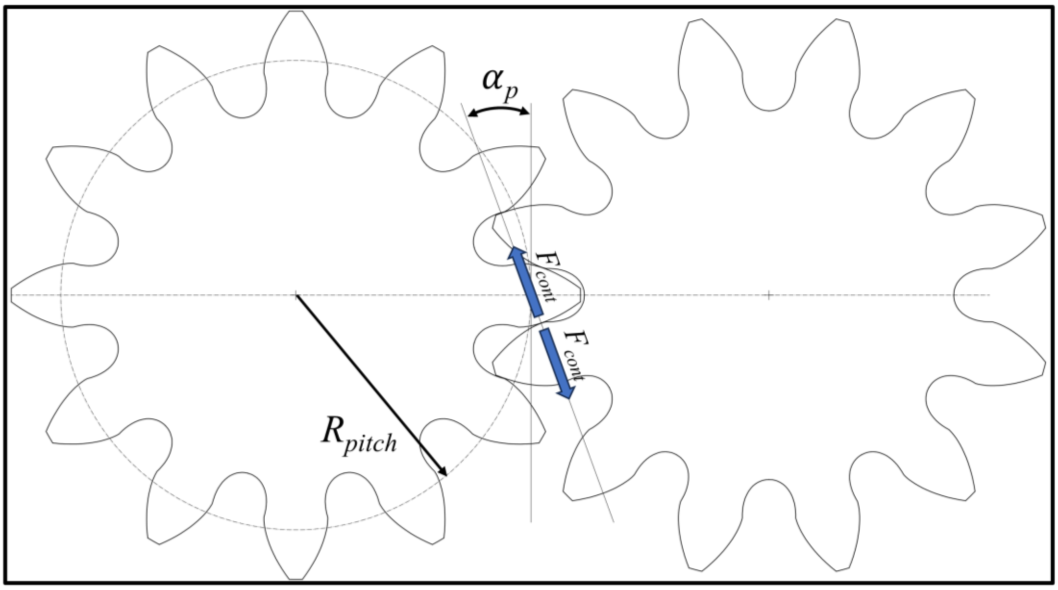

Figure 20 - Teeth contact force.

The value of this force is expressed by the following equation:

$$F_{cont} = \frac{M_N}{R_{pitch} \cdot \cos\alpha_p} \tag{63}$$

where R_{pitch} is the radius of the pitch circle and α_p is the pressure angle of the coupled gears.

This force acts along the line of contact, creating a couple of forces of equal values but opposite direction, as shown in Figure 20. The component of these forces along the axis of the reference system are the following:

$$\begin{aligned} F_{cont,x,G} &= -\cos\beta \cdot F_{cont} \cdot \sin\alpha_p \\ F_{cont,y,G} &= \cos\beta \cdot F_{cont} \cdot \cos\alpha_p \end{aligned} \tag{64}$$

$$\begin{aligned} F_{cont,x,N} &= \cos\beta \cdot F_{cont} \cdot \sin\alpha_p \\ F_{cont,y,N} &= -\cos\beta \cdot F_{cont} \cdot \cos\alpha_p \end{aligned} \tag{65}$$

In case of helical gears, the force contact has to be normal also to the helical angle and thus it also creates a component along the axial dimension of the pump that is projected along the z-axis of the reference system through the following formulation:

$$F_{cont,z,G} = \sin\beta \cdot F_{cont}$$
$$F_{cont,z,N} = -\sin\beta \cdot F_{cont} \tag{66}$$

III.2.4.2.3. The Total Force Acting on Pump's Gear

The overall force value along the x and y-axis of the reference system acting on each gear is:

$$F_{tot,x,G} = F_{p,tot,x,G} + F_{tl,x,G} + F_{sl,x,G} + F_{rl,x,G} + F_{cont,x,G}$$
$$F_{tot,y,G} = F_{p,tot,y,G} + F_{tl,y,G} + F_{sl,y,G} + F_{rl,y,G} + F_{cont,y,G} \tag{67}$$

$$F_{tot,x,N} = F_{p,tot,x,N} + F_{tl,x,N} + F_{sl,x,N} + F_{rl,x,N} + F_{cont,x,N}$$
$$F_{tot,y,N} = F_{p,tot,y,N} + F_{tl,y,N} + F_{sl,y,N} + F_{rl,y,N} + F_{cont,y,N} \tag{68}$$

In case of helical gears, an additional force component along the z-axis is present and the total force value along this direction is equal to:

$$F_{tot,z,G} = F_{p,z,G} + F_{cont,z,N}$$

$$F_{tot,z,N} = F_{p,z,N} + F_{cont,z,N} \tag{69}$$

Finally, the overall force value and the angle of its line of direction acting on each gear are:

$$F_{tot,G} = \sqrt{F_{tot,x,G}^2 + F_{tot,y,G}^2}$$

$$\alpha_G = \arctan\frac{F_{tot,y,G}}{F_{tot,x,G}} \tag{70}$$

$$F_{tot,N} = \sqrt{F_{tot,x,N}^2 + F_{tot,y,N}^2}$$

$$\alpha_N = \arctan\frac{F_{tot,y,N}}{F_{tot,x,N}} \tag{71}$$

In case of helical gears, referring to a spherical coordinate system, the overall force value and the angles of line of directions acting on each gear are:

$$F_{tot,G} = \sqrt{F_{tot,x,G}^2 + F_{tot,y,G}^2 + F_{tot,z,G}^2}$$

$$\alpha_G = \arctan \frac{F_{tot,y,G}}{F_{tot,x,G}} \tag{72}$$

$$\theta_G = \operatorname{arccot} \frac{F_{tot,z,G}}{\sqrt{F_{tot,x,G}^2 + F_{tot,y,G}^2}}$$

$$F_{tot,N} = \sqrt{F_{tot,x,N}^2 + F_{tot,y,N}^2 + F_{tot,z,N}^2}$$

$$\alpha_N = \arctan \frac{F_{tot,y,N}}{F_{tot,x,N}} \tag{73}$$

$$\theta_N = \operatorname{arccot} \frac{F_{tot,z,N}}{\sqrt{F_{tot,x,N}^2 + F_{tot,y,N}^2}}$$

III.2.5. The Bearings' Reactions Evaluation Subroutine

The final subroutine of the EgeMATor MP+ tool is tightly related to the previous one and enables the evaluation of the micromotions of the pump's gears by evaluating the bearings' reactions to the load acting on them. This subroutine was written in MATLAB® and requires the input of the geometrical data of the bearings, while the load applied on them is obtained from the force and torque subroutine described in the previous section. The code implements a finite difference method to solve the pressure film around the bearing to balance the load applied to it. The eccentricity and the angle of minimum film thickness values are then found through an iterative inverse procedure.

The journal bearing geometry adopted and the force acting on it can be seen in Figure 21.

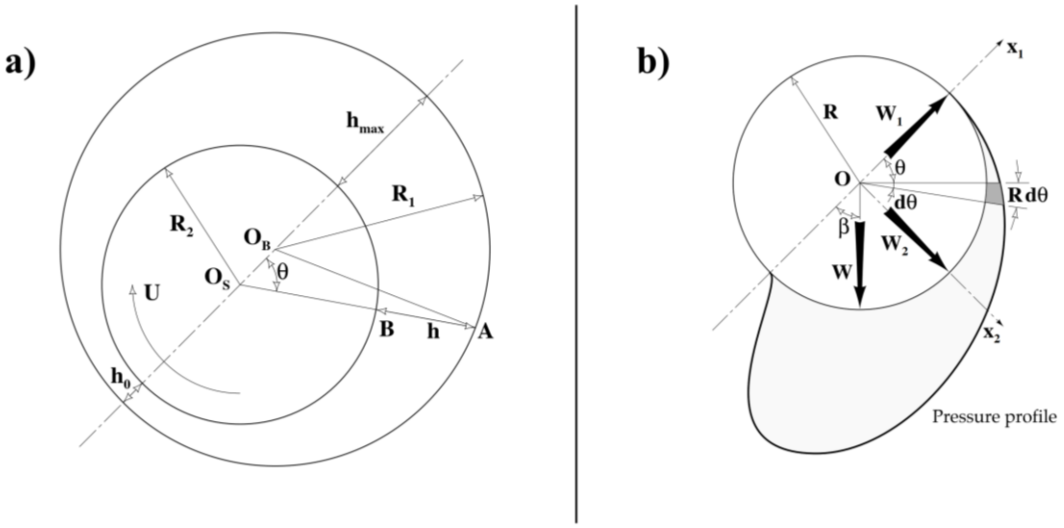

Figure 21 – Journal bearing model: a) geometry parameters definition; b) force acting on the bearing.

The methodology implemented is based on the resolution of the Reynold equations of the fluid films under the "*isoviscous*" approximation approach [34]. This approach assumed that the lubricant viscosity is constant over the film, neglecting thus the thermal effects in the hydrodynamic films. Under this assumption and with the geometry showed in Figure 21, the Reynolds equation for the fluid film can be expressed as:

$$\frac{\partial}{\partial x}\left(h^3\frac{\partial p}{\partial x}\right)+\frac{\partial}{\partial y}\left(h^3\frac{\partial p}{\partial y}\right)=6U\eta\frac{dh}{dx} \tag{75}$$

where h is the hydrodynamic film thickness, p is the film pressure, U is the bearing entraining velocity and η is the dynamic viscosity. The first step done for the implementation of the finite difference methodology was the introduction of non-dimensional methodology. This methodology consists in the substitution of all the real variable of an equation by dimensionless fractions of two or more real parameters. The benefits of this procedure are the reduction of the number of controlling parameters and a better fit to be implemented in computers' code. In the case of journal bearings with isoviscous hypothesis, the Reynolds equation (75) is expressed as a function of the film thickness *h,* pressure *p*, entraining velocity *U* and dynamic viscosity *η*. Non-dimensional forms of this variable are the following [35]:

$$\begin{aligned} h^* &= \frac{h}{c} \\ x^* &= \frac{c}{R} \\ y^* &= \frac{y}{L} \\ p^* &= \frac{pc^2}{6U\eta \mathrm{R}} \end{aligned} \tag{76}$$

Where *c* is the bearing radial clearance, *R* is the bearing radius and *L* is the bearing axial length. Although any other scheme of non-dimensionalization can be used, this particular scheme is the most popular and convenient. Substituting the equations (76) in equation (75), the non-dimensional Raynolds equations is obtained:

$$\frac{\partial}{\partial x^*}\left(h^{*3}\frac{\partial p^*}{\partial x^*}\right)+\left(\frac{R}{L}\right)^2\frac{\partial}{\partial y^*}\left(h^{*3}\frac{\partial p^*}{\partial y^*}\right)=6U\eta\frac{\partial h^*}{\partial x^*} \tag{77}$$

In equation (77) all terms are non-dimensional apart from R and L which are only present as a non-dimensional ratio.

To improve the accuracy of the numerical solutions of the Reynolds equation, Vogelpohl [36] developed the homonymous parameter, defined as follow:

$$M_v = p^* h^{*1.5} \tag{78}$$

Substituting this parameter in the non-dimensional form of Reynolds equation (77) yields the “Vogelpohl equation”:

$$\frac{\partial^2 M_v}{\partial x^{*2}}+\left(\frac{R}{L}\right)^2\frac{\partial^2 M_v}{\partial y^{*2}}=FM_v+G \tag{79}$$

where parameter F and G for journal bearings are characterized as follows:

$$F=\frac{0.75\left[\left(\frac{\partial h^*}{\partial x^*}\right)^2+\left(\frac{R}{L}\right)^2\left(\frac{\partial h^*}{\partial y^*}\right)^2\right]}{h^{*2}}+\frac{1.5\left[\frac{\partial^2 h^*}{\partial x^{*2}}+\left(\frac{R}{L}\right)^2\frac{\partial^2 h^*}{\partial y^{*2}}\right]}{h^*} \tag{80}$$

$$G=\frac{\left(\frac{\partial h^*}{\partial x^*}\right)}{h^{*1.5}} \tag{81}$$

The Vogelpohl parameter facilitates computing by simplifying the differential operators of the Reynolds equation, and furthermore it does not show high values of higher derivatives in the final solution, unlike the dimensionless pressure p^*. This is due to the fact that while p^* exhibits a sharp increase close to the minimum of hydrodynamic film thickness h^*, the M_v parameter remain instead at moderate values. Large values of higher derivatives cause significant truncation error in numerical analysis, so this clarifies why the Vogelpohl permits to improve the accuracy of the solution. Figure 22 shows a comparison of the characteristics between the Vogelpohl parameter and the non-dimensional pressure along the surface of a journal bearing with an eccentricity of 0.95 done by Cameron [38].

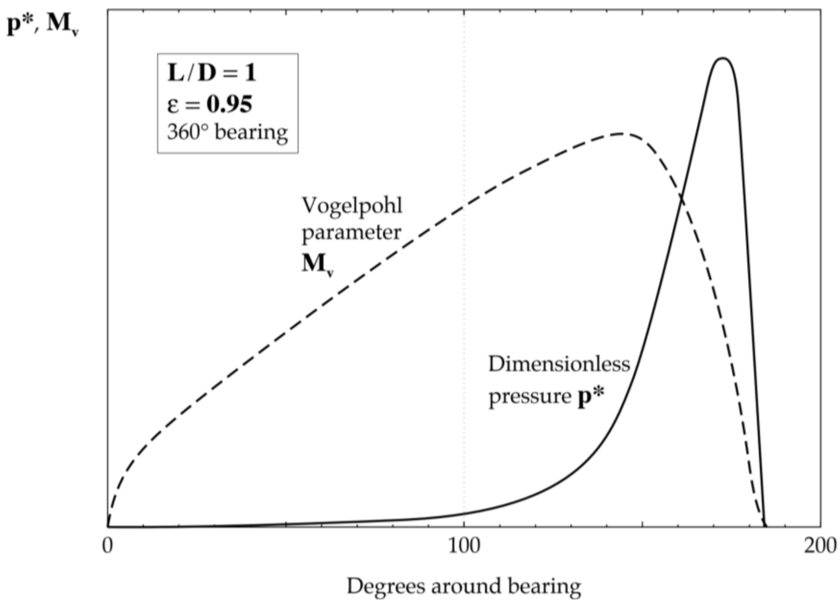

Figure 22 - Comparison of characteristics between M_v and p^*.

It can be seen from Figure 22 that the introduction of the Vogelpohl parameter does not complicate the boundary conditions in the Reynolds equation, since wherever p^* is equal to zero, so is M_v (zero values of h, i.e., solid to solid contact, are not included in the analysis). Also, wherever cavitation occurs, the gradient of M_v adjacent and normal to the cavitation front is zero like that of p^*. Numerical solutions of the Reynolds equation are obtained in terms of the Vogelpohl parameter and values of non-dimensional pressure are obtained from the definition of M_v.

The finite difference method implemented in this subroutine was based on approximating a differential quantity by the difference between function values at two or more adjacent nodes. The finite difference approximation for the first and second differential of the Vogelpohl equation are:

$$\left(\frac{\partial M_v}{\partial x^*}\right)_i \approx \frac{M_{v,i+1} - M_{v,i-1}}{2\delta x^*}$$
$$\left(\frac{\partial^2 M_v}{\partial x^{*2}}\right)_i \approx \frac{M_{v,i+1} + M_{v,i-1} - 2M_{v,i}}{(\delta x^*)^2} \tag{82}$$

Substituting in the equation (79) and also considering the approximation along the y dimension, the basis equation of the finite difference method is obtained:

$$M_{v,i,j} = \frac{C_1\left(M_{v,i+1,j} + M_{v,i-1,j}\right) + \left(\frac{R}{L}\right)^2 C_2\left(M_{v,i,j+1} + M_{v,i,j-1}\right) - G_{i,j}}{2C_1 + 2C_2 + F_{i,j}} \tag{83}$$

where the parameter C_1 and C_2 are defined as:

$$C_1 = \frac{1}{\delta x^{*2}}$$

$$C_2 = \frac{1}{\delta y^{*2}} \tag{84}$$

For the journal bearing, the boundary conditions require that p^* or M_v are zero at the edges of the bearing and also that cavitation can occur to prevent negative pressures occurring within the bearing. The range of x^* is between 0 - 2π ($360°$ angle). The range of y^* is from -0.5 to $+0.5$ as the mid-line of the bearing is selected as a datum. A domain of the journal bearing is shown in Figure 23.

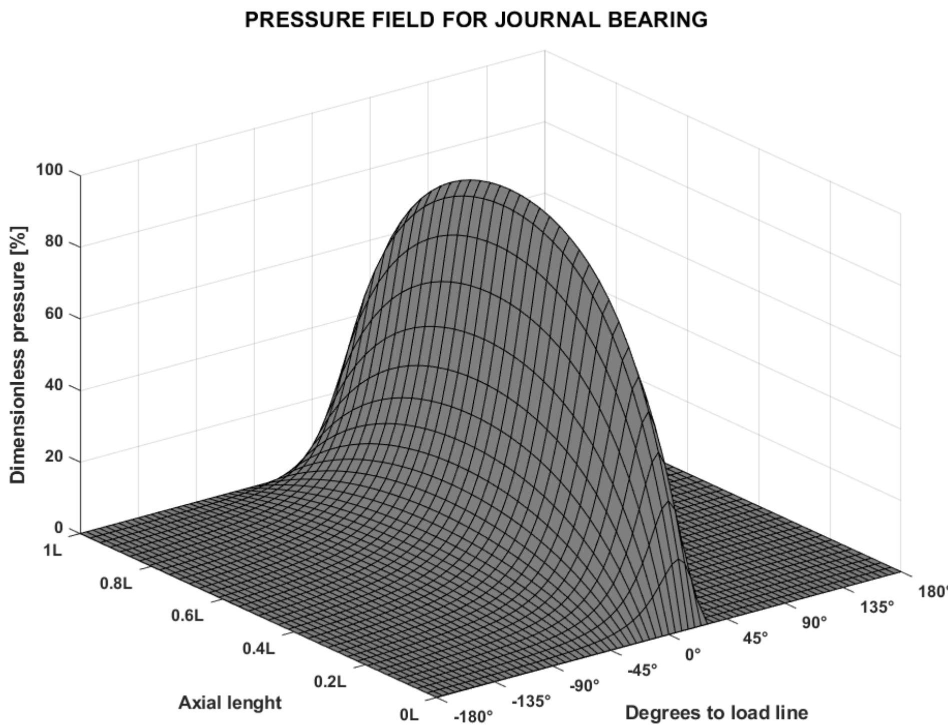

Figure 23 - Typical non-dimensional pressure field evaluated by the described subroutine methodology.

Nodes on the edges of the bearing remain at a pre-determined zero value while all other nodes require solution by the finite difference method.

The nodal values of M_v are conveniently arranged in a matrix with i and j as the column and row ordinates. The coefficients in equation (80) can also be organized into a sparse matrix with all coefficients lying close to the main diagonal. It is therefore possible to solve equation (80) by matrix inversion, but this requires elaborate computation.

Programming is greatly simplified when iterative solution methods are applied. The Gauss-Seidel iterative method is used in this subroutine. All node values are assigned an initial zero value, and the finite difference equation (80) is repeatedly applied until convergence is obtained and the film pressure distribution is evaluated for all the nodes.

This methodology allowed to evaluate the film pressure field, load, and attitude angle given the geometric bearing's characteristics, the bearing rotational speed and the eccentricity ratio as input.

So, a further iterative procedure was implemented where the obtained bearing, is compared with the value of the force on the gears obtained from the *Force and Torque subroutine.* Until a convergence between these values is reached, the iterative procedure continues to be executed changing the value of the eccentricity ratio.

The micromotions of the gears is then obtained through the following equations:

$$x_G = e_G \cdot c \cdot \cos(\beta_G + \alpha_G)$$
$$y_G = e_G \cdot c \cdot \sin(\beta_G + \alpha_G) \tag{85}$$

$$x_N = e_N \cdot c \cdot \cos(\beta_N + \alpha_N)$$
$$y_N = e_N \cdot c \cdot \cos(\beta_N + \alpha_N) \tag{86}$$

In case of helical gears, the methodology is still valid if the value of the force acting on the gear used as a comparison parameter for the subroutine is taken from only the x and y-axis. The z-axis component, while creating a thrust force, does not influence the load acting on the bearing and thus the gear's micromotion.

Chapter IV: Validation of the Tool

The traditional way to validate a numerical model consist in the execution of an extensive experimental campaign on a reference EGP and then compare the measured data obtained with the results obtained from the numerical model using the same reference EGP's geometrical data and working conditions measured in the experimental campaign.

For the validation of the EgeMATor MP+ tool developed in this work a different approach was used. A hybrid approach was employed, in which a smaller experimental campaign was carried out and the measurements obtained from it were utilized to validate a 3D CFD numerical model specifically developed. In fact, as already demonstrated in other work available in the literature [10], a 3D CFD numerical model require less measurement data to be validated to an acceptable level compared to a lumped parameter numerical model.

The validated 3D CFD numerical model allowed to obtain additional information on the EGP's dynamic behavior which could only be accessed through an experimental campaign by using special sensors, e.g., the pressure trend inside a CV during gears' rotation. Coupling the 3D CFD numerical model with the results of the standard experimental campaign, it was possible to fully validate the EgeMATor MP+ tool developed with a reduced number of 3D CFD numerical simulations, thus limiting the high computational power drawback of this type of numerical model.

This approach permitted also to execute an experimental campaign that needed smaller time but more importantly a standard typology of sensors to employ and utilize. This was the main focus due to the desire to take advantage of a test bench that were available at the company collaborating with this Ph.D. program.

The following sections will describe the reference pump deployed to validate the numerical tool, the setting up of the test bench and the measurement done in the experimental campaign, the description of the 3D CFD numerical model and finally the validation results of the EgeMATor MP+ tool will be presented and discussed.

IV.1. The Reference External Gear Pump

The acquisition of the Hydreco company by Duplomatic MS in the early 2020 opened the way to the EGMs products and projects for them. In particular, one of these projects was about a *low noise* series of pumps for generic high pressure applications. During the early test in the Duplomatic labs, the pump resulted exhibiting very efficient values from the volumetric point of view, but the noise emission did not convince the research and development department, being remarkably similar to the one of the *standard series*.

It was at that point that collaboration Ph.D. program between the Duplomatic MS company and the University of Naples Federico II came along. The support given along this program was mainly based on numerical modeling, in methodology to correctly test the pump and collect the measured data, and in finding way to understand the emission noise source and further reducing the noise emissions.

The analysis conducted in this work was executed on one of the EGPs of this *low noise* series. The reference EGP consists of a couple of helical gears with a displacement of 14.5 cm^3/rev, with a case made from die-cast alloy while the front and the rear covers are made of cast iron. This type of construction allowed to reach higher maximum pressures while maintaining a small weight, making it ideal for mobile applications but without increasing to much the global cost.

The basic technical data of the reference pump are listed in Table 1.

Table 1 - *Reference pump technical data*

Description	Value	Unit
Nominal displacement	14.5	cm^3/rev
Max. continuous pressure	260	bar
Max. intermitted pressure	290	bar
Max. peak pressure	310	bar
Min. rotational speed	500	rev/min
Max. rotational speed	3500	rev/min

Figure 24 shows the physical exterior aspect and the exploded view of the reference pump.

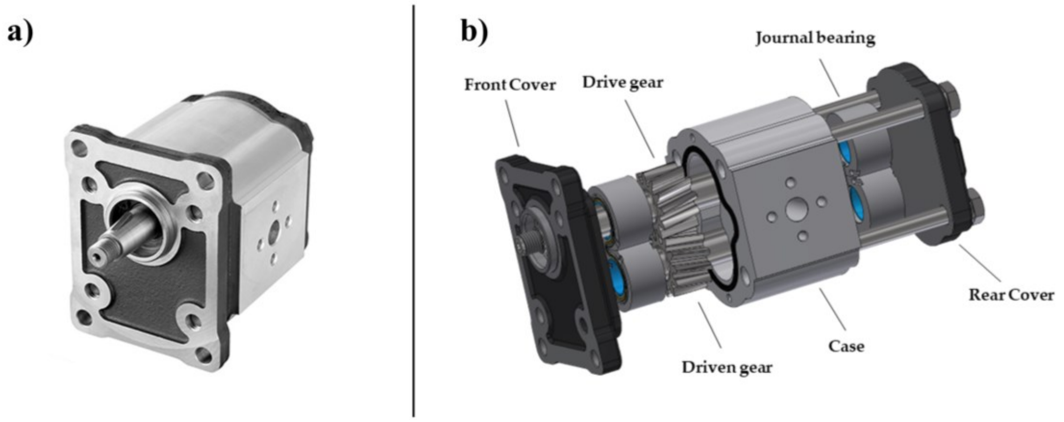

Figure 24 - Reference helical EGP: a) physical aspect; b) exploded vision.

IV.2. Test Bench Setup

The collaboration with Duplomatic MS made it possible to use equipment and instrumentation available in their lab. In there a test bench that used EGPs to check hydraulic cylinders was available and at the time of the start of the collaboration was not utilized. So, it was decided to utilize this test bench, after the required changes, to test the reference pump and to use the acquired data to validate the numerical models. Figure 25 shows the initial aspects of the test bench before the modification and adaptation work was executed.

Figure 25 - Initial test bench aspects.

The modification and adaptation required by this test bench were both hardware and software, but the latter were the one that required a more extensive study and tuning. In fact, being a test bench to validate the quality of hydraulic cylinders, no Data Acquisition System (DAQ) were available on it, so it was needed to be created from scratch. The hardware modification required the mounting and coupling adapter to be individuated an installed to fit the EGP to the servomotor.

Other hardware changes were the removal of redundant control valves and other hydraulic components (like, for example, the hydraulic accumulator visible in Figure 25 that would be not used for the test of the EGPs and the by-pass of the hydraulic cylinder with the required connections fittings.

The software changes required the building of a DAQ system to acquire and log the measurements from the pressure sensors and the flow meter. This was achieved by employing a National Institute (National Instrument Corp., Austin, USA) DAQ system. In particular, a NI cDAQ-9174 chassis was used to connect the DAQ module to the data logging and controlling PC through a USB connection. The chassis was connected to the NI-9201 voltage input module to acquire the voltage signals received from the pressure sensors and the flow meters. Besides, a NI-9263 voltage output module was also implemented to control the pressure relief valve responsible of regulating the pressure load acting on the tested EGP. Both these modules were controlled by the PC using a code written in the LabVIEW software environment developed by the Fluid Power group of the University of Naples Federico II. The developed code allows to monitor in real time the data obtained from the instrumentation already scaled in the appropriate measurement units, save them in log data files, and controlling the pressure loading valve both manually that through an imposed predetermined cycle. Figure 26 shows the interface of the developed code.

Figure 26 - Interface of the data acquisition code developed.

The hydraulic scheme of the final test rig with all the required adjustment to follow the ISO 4409:2019 [39] the is shown in Figure 27.

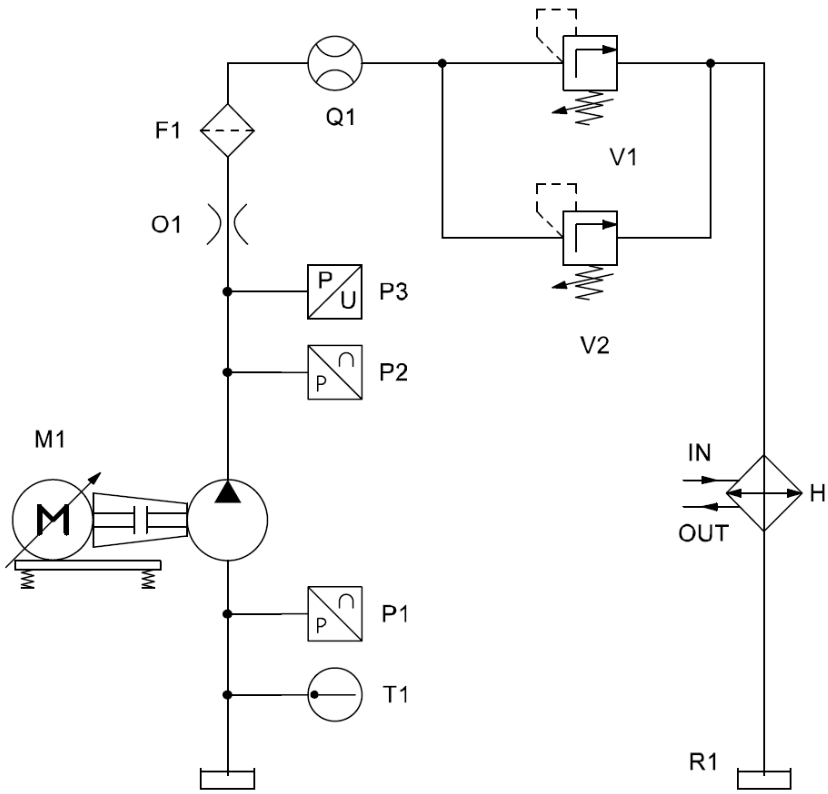

Figure 27 - Test bench hydraulic scheme.

A servomotor drives the tested pump by a flexible coupling. The proportional pressure relief valve V_1 generates the load for the pump at the required pressure while the proportional pressure relief valve V_2 is mounted in parallel with the previous one for safety reasons. Two pressure transmitters sensors, P_1 at the inlet side and P_2 at the delivery side are used to acquire the pressure signal. A high-pressure filter is installed before the flowmeter Q_1 to avoid pollutants reaching the reservoir and protect it from debris. Lastly, the thermal conditioning system consists of a water-cooled heat exchanger that recovers the oil directly from the reservoir. It is placed after the loading valve and allows control of the oil temperature in a range of ± 1°C. The detailed information for each described component is listed in Table 2.

The setup to acquire pressure ripples, using the sensor P_3, has been obtained by adding a rigid duct with a fixed orifice, O_1, placed right after the P_3 pressure sensors (as shown in Figure 27). The orifice, which has a diameter of 1.72 mm, gives the requested load. The data obtained by the sensor P_3 was acquired through the use of a NI USB-4431 DAQ system, a 24-bit Dynamic Signal Acquisition.

Tests have been carried out with an oil *ISO 46*, grade *HL*, maintaining the temperature in the range 40° C ± 1°C. The pump has been tested varying the delivery pressure from minimum to maximum continuous for different speeds. The experimental campaign has involved the analysis of several working conditions with the additional measurement of the noise and vibration levels. Being the numerical models focused on the fluid dynamic aspect, only a reduced number of the acquired parameters corresponding to the working conditions tested have been utilized to validate the numerical models.

__Table 2__ - Hydraulic test bench components feature.

Name	Description	Details
P_1	Inlet pressure sensor	Duplomatic model PTH, scale: -1÷10 bar and ±0.25% FS
P_2	Outlet pressure sensor	Duplomatic model PTH scale: 0÷400 bar and ±0.25% FS
P_3	High-frequency pressure sensor	PCB® model 113B26, (PCB Piezotronics, Inc., NY, USA), 0÷10kHz, resonant frequency: >= 500 kHz
M_1	Electric servomotor	KEB G2, Max Power: 46 kW, Max working Torque: 220 Nm, Speed Range: 0÷3000 rev/min
Q_1	Flow meter	VSE VS 0.4 (VSE.flow®, Neuenrade, Germany), scale 0.03÷40 L/min, 0.3% measured value accuracy
F_1	Filter	MP Filtri model FHP 350, Nominal filter rating: 25 µm, Max working pressure: 420 bar
V_1	Load valve	Duplomatic model PRE25J, Capacity 400 L/min, Maximum working pressure: 350 bar
V_2	Pressure relief valve	Duplomatic model RQM5-P, Capacity 400 L/min, Maximum working pressure: 350 bar
H_1	Heat exchanger	WTK P7-60 FF
R_1	Reservoir	Duplomatic 600LT C.S., Capacity: 600 L, ISO VG 46
T_1	Inlet thermocouple	Trafag model T1, PT-100, scale -10÷100 °C, class A accuracy

IV.3. The Three-dimensional CFD Numerical Model

The 3D CFD numerical modeling constitutes the most advanced method for evaluating the flow field of positive displacement pumps. This methodology is based on the resolution of the Navier-Stokes equations in a three-dimensional domain discretized with a varying geometry mesh. The major difficulties of this approach are the definition and application of procedures to deform and transpose the grid mesh as the gears rotate and the grid refinement required to model the small gaps. Overcoming these difficulties permit to correctly evaluate the non-uniform pressure distribution in each displacement chamber and to factor in different variable chamber shapes and effects of the inlet and out-let structures.

The three-dimensional CFD numerical model used in this work to provide a further validation tool for the lumped parameter model developed implements a novel approach by using a new capability available in the commercial code Simerics MP+ v.5.2.15, developed by Simerics Inc. (1750 112th Ave NE, Ste C250, Bellevue, WA 98004). This approach employs the use of a body-fitted binary tree grid generator that accurately follows the fluid volume extracted along the gears' helical angle. The parent-child tree architecture permits to obtain expandable data structure requiring reduced memory storage, generating thus an accurate and efficient grid, hence eliminating the need of geometry approximations, as can be found in previous works in literature [15].

The fluid domain was obtained from the CAD files of the pump, extracting only the necessary surfaces and volumes required for the developed model, as shown in Figure 28.

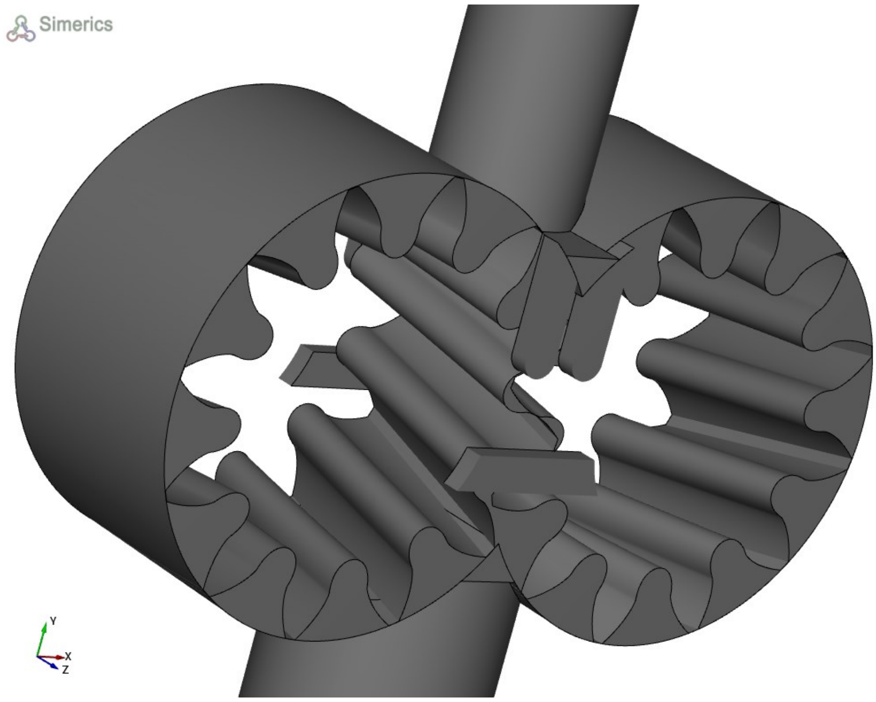

Figure 28 - Reference helical gear pump fluid domain.

The fluid volumes obtained were meshed using the rotor template Mesher for EGPs with a structural mesh for the gears that is updated automatically during the rotation.

A mesh sensitivity analysis was executed by varying the number of cells used to discretize the helical gears and the wear-plates and comparing the mean volumetric flow rate with the one acquired during experimental tests; four different rotor and wear-plates grids with progressively finer mesh have been modeled.

Table 3 lists the number of cells used to model them for each analyzed mesh while Figure 29 reports the convergence of the volumetric flowrate done with the four models.

Table 3 *- Number of cells of the different mesh used in the sensitivity analysis.*

Mesh	Number of cells
Mesh #1	195k
Mesh #2	330k
Mesh #3	700k
Mesh #4	1.49M

The results obtained from this analysis show that the coarser mesh number one had proved to have low accuracy with an error of 18%, while the finer mesh had a convergence increment so minor that does not justify the higher computational power and time that required. The mesh number three was chosen to be employed in the following analysis.

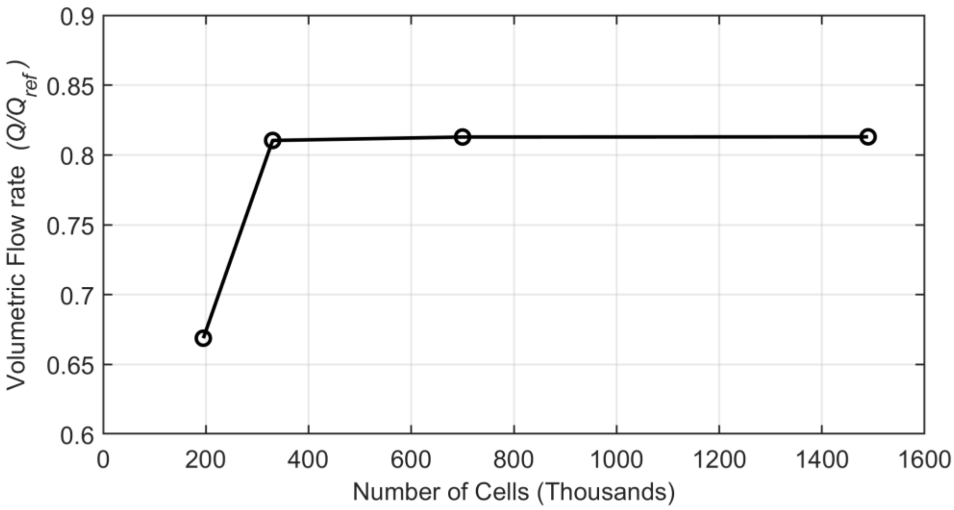

Figure 29 - Convergence of the volumetric flowrate for the mesh sensitivity analysis.

The final model with the chosen grid mesh contained around 950k cells and it is shown in Figure 30.

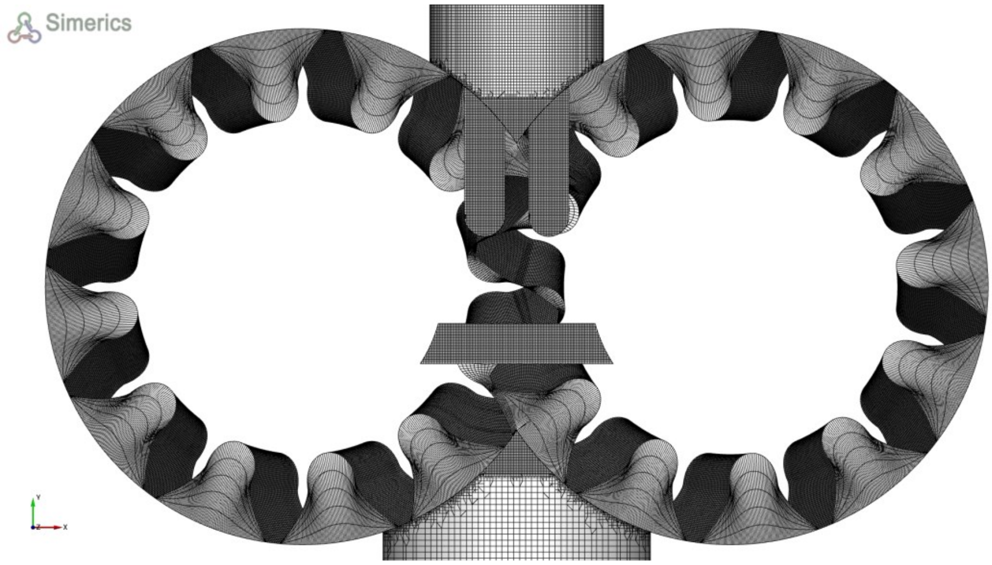

Figure 30 - Final mesh grid of pump's fluid domain.

The simulations were run on a workstation provided with an Intel® Xeon® CPU E5-2640v2 @ 2.00 GHz (two processors) with 192 GB RAM. The computational time required to complete a shaft revolution, with a saving angle step of 0.5 degrees, was about 36 hours.

The pressure forces effect that acts on the gears were considered in the model by translating them along the vertical axis toward the inlet side, reducing the clearance between the gears' tooth tip and the housing. Along with the contact between the driving and the driven gear, this entailed a problem for the 3D CFD numerical model which does not permit inserting null clearances. Thus, the choice of the value for these gaps was of utmost importance to replicate real working conditions. The driven gear was also rotated to reproduce the contact with the driving gear. Theses aspects imposed the execution of a gap analysis to find a value that permits to reduce the leakages through the gaps to more realistic values without losing the convergence of the simulation. A starting value of *25 μm* was chosen. The analysis yielded unrealistic high crossflow values during the meshing for the chosen initial value, while the more restrictive value *of 5 μm* reports minimal leakages. Therefore, a gap of *5 μm* was then chosen for both gaps inquired and shown in Figure 31. For the reference pump analyzed, the value employed offsetting the gear by *35 μm* toward the inlet side and a relative rotation of 0.11 degree for the driven gear against the driving one.

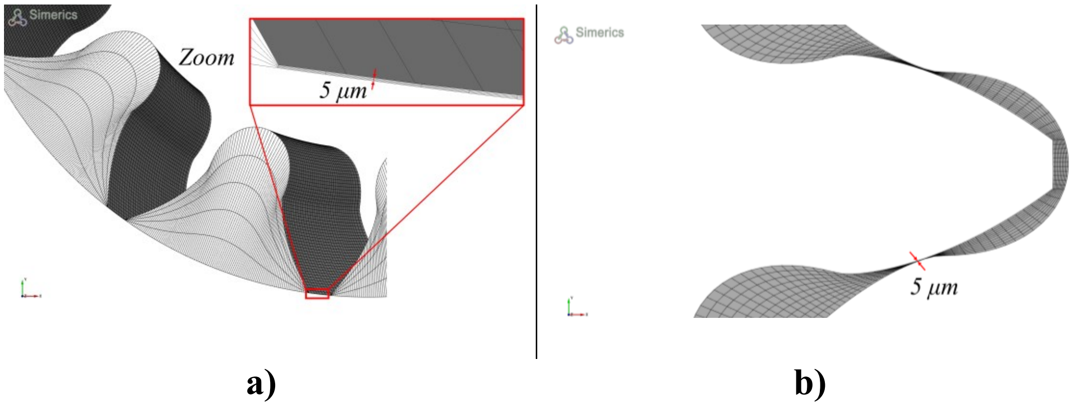

Figure 31 - Mesh gap analysis: a) tooth's tip and housing gap value; b) meshing teeth contact gap value.

The numerical model includes the evaluations of turbulence and cavitation. The turbulence was predicted using a standard k-ε turbulence model with the implementation of the Renormalization Group Theory (RNG) statistical technique. This statistical technique permitted to increase the model response to rapid strains, thus increasing the results' accuracy requiring only an exiguous amount of additional computational power. The robustness of this implemented methodology can be found in numerous works available in literature [40 - 46], while the equations of the model and a comparison with the standard *k-ε* turbulence model can be found in technical literature [47 - 48].

The cavitation model employed is directly available in Simerics MP+ and is capable of predicting cavitating conditions with high reliability. It is an extension of the work of Singhal et al., based on the Rayleigh-Plesset equation [49] appraising cavitation, aeration and liquid compressibility. This model considers the fluid in cavitating conditions to be a mixture of liquid, vapor and some non-condensable gas (NCG). The vapor distribution is characterized by this model with the following equation:

$$\frac{\partial}{\partial t}\int_{\Omega(t)} \rho f_v d\Omega + \int_{\sigma} \rho\big((\vec{v} - \vec{v_\sigma}) \cdot \vec{n}\big) f_v d\sigma = \int_{\sigma} \left(D_v + \frac{\mu_t}{\sigma_v}\right)(\nabla f_v \cdot \vec{n}) d\sigma + \int_{\Omega} (R_e - R_c) d\Omega \tag{87}$$

where D_v is the diffusivity of the vapor mass fraction and σ_v is the turbulent Schmidt number. For this analysis, these two numbers are set equal to the mixture viscosity and unity, respectively. The vapor generation term, R_e, and the condensation rate, R_c, are evaluated with the following equations:

$$R_e = \begin{cases} C_e \dfrac{\sqrt{k}}{\sigma_l} \rho_l \rho_v \left[\dfrac{2}{3} \dfrac{(p - p_v)}{\rho_l}\right]^{\frac{1}{2}} \left(1 - f_v - f_g\right) & p < p_v \\ 0 & p \geq p_v \end{cases}$$

$$R_c = \begin{cases} 0 & p < p_v \\ C_c \dfrac{\sqrt{k}}{\sigma_l} \rho_l \rho_v \left[\dfrac{2}{3} \dfrac{(p - p_v)}{\rho_l}\right]^{\frac{1}{2}} f_v & p < p_v \end{cases} \tag{88}$$

The Singhal's cavitation theory was expanded to include also non-condensable gases (NCG) in the liquid [48]. The unsteady mixture (liquid, liquid vapor and NCG) density ρ is evaluated in accordance with the formula (89):

$$\frac{1}{\rho} = \frac{f_v}{\rho_v} + \frac{f_g}{\rho_g} + \frac{\left(1 - f_v - f_g\right)}{\rho_l} \tag{89}$$

The NCG in the hydraulic fluid can be found in a free and/or in a dissolved state. The cavitation modeling utilized for this analysis is the Equilibrium Dissolved Gas Model. This model assumes that the free NCG mass fraction is not constant; its evaluation is obtained by the resolutions of a further transport equation for the mass fraction of the dissolved gas (90):

$$\begin{aligned} \frac{\partial}{\partial t}\int_{\Omega(t)} \rho\, f_{g,d}\, d\Omega + \int_{\sigma} \rho\left(\left((\vec{v} - \vec{v_\sigma}) \cdot \vec{n}\right) f_{g,d}\, d\sigma\right) \\ = \int_{\sigma} \left(D_{f_{g,d}} + \frac{\mu_t}{\sigma_{g,d}}\right)(\nabla f_{g,d} \cdot \vec{n})\, d\sigma \\ \cdot \int_{\Omega} \frac{\rho}{\tau}\left(\frac{p}{p_{d,equil,ref}} f_{d,equil,ref} - f_{g,d}\right) d\Omega + \int_{\Omega} \left(S_{g,d}\right) d\Omega \end{aligned} \tag{90}$$

where $f_{d,equil,ref}$ is a user-specified value and represents the equilibrium mass fraction of the dissolved gas at the reference pressure $p_{d,equil,ref}$, another user-specified value as well; $S_{g,d}$ is the law of gas dissolution or release defined by the user. The time scale τ, for this model implemented, tends toward zero, resulting so in a near-instant mass transfer. The mass fraction of the free gas is evaluated from the following condition:

$$f_g = f_{g,f} + f_{g,d} = f_{g,specified} \quad (91)$$

where $f_{g,specified}$ is another user-specified value.

The model developed requires a certain number of parameters to characterize the modeled fluid and the boundary conditions of the pump. The analysis conducted in this work were executed with the parameters listed in Table 4.

Table 4 *- Parameters and boundary conditions used for the numerical developed model.*

Parameter	Value	Unit
Dynamic fluid viscosity	0.03763	$Kg \cdot m^{-1} \cdot s^{-1}$
Liquid Density	851	Kg/m^3
Fluid Temperature	313.15	K
Inlet Pressure	1.12	bar (absolute)
Liquid Bulk Modulus (β_k)	11000	bar
Linear Bulk Modulus Coefficient (K_1)	9	-
Saturation Pressure	1e-06	bar (absolute)
Dissolved Gas Reference Pressure	0.25	bar (absolute)
Dissolved Gas Mass Fraction	2.94e-05	-

The parameters presented in Table 4 were chosen in different ways. Some of them, like the oil density and the dynamic fluid viscosity, were obtained from the datasheet of the hydraulic oil used in the test bench. The fluid temperature and the pressure inlet reflect the data obtained from the sensors of the test bench. Finally, the remaining parameters' values derived from experience of previous works conducted on this typology of pump done by the author's research group.

One of the main advantages of 3D CFD numerical model is the possibility to evaluate cavitation phenomena inside the computational domain of the simulated gear pump. Due to the unfeasibility for lumped parameter model to evaluate this phenomenon and being this work focused on the validation of the lumped parameter tool, this aspect was not investigated.

The 3D CFD numerical model allows to also study the pressure wave effects, so an analysis of the pressure ripple at the delivery side of the pump was also carried out. To reproduce the same conditions of the experimental validation campaign, the numerical model implemented a supplementary volume. This new volume has the same geometry as the one used on the test bench which consists of a rigid duct with a fixed orifice of *1.72 mm* at its end.

The final geometry implemented in the numerical model is shown in Figure 32, where is also represented the position of the monitoring point added into the model located at the same position as the high-frequency pressure transducer (P_3 in Figure 27) used during the experimental campaign.

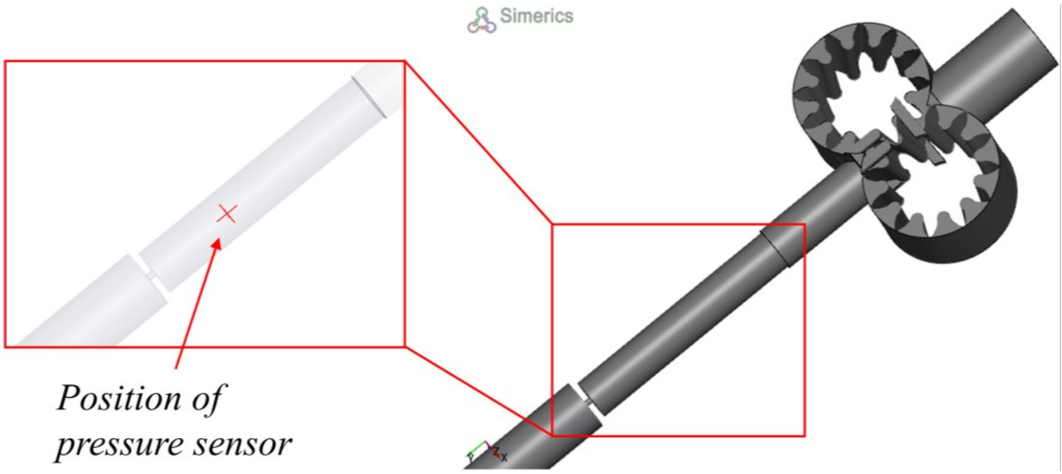

Figure 32 - Pressure ripple analysis: fixed orifice and the monitoring point.

IV.4. Validation Results

This section presents a comparison analysis between the experimental test campaign data, the 3D CFD and lumped parameters numerical models and thus validating the numerical models, especially the EgeMATor MP+ lumped parameter model.

The experimental campaign involved the analysis of high number of working conditions. Naturally, this high number of working conditions could be replicated also by the numerical models, but that would require too much time to be executed, especially the 3D numerical model.

For this reason, the simulations for the 3D numerical model were executed for three different pump shaft speeds and two different outlet pressures, for a total number of six different working conditions simulated, as listed in Table 5.

Table 5 *- Definition of the working condition simulated for the 3D numerical model.*

	Speed (rev/min)	**Outlet Pressure (bar)**
S1	1000	100
S2	1000	200
S3	1500	100
S4	1500	200
S5	1800	100
S6	1800	200

The lumped parameter model allowed to simulate a higher number of working conditions thanks to its lower computational resources and time required. A total number of 24 simulation for the lumped parameter model were executed, swiping four different pump shaft speeds and six different outlet pressures. The specific speeds and outlet pressure are listed in Table 6.

Table 6 *- Definition of the working condition simulated for the 3D numerical model.*

Outlet Pressure (bar)	**1000 (rev/min)**	**1500 (rev/min)**	**1800 (rev/min)**	**2200 (rev/min)**
20	•	•	•	•
50	•	•	•	•
100	•	•	•	•
150	•	•	•	•
200	•	•	•	•
240	•	•	•	•

The analysis has been split in two parts: the first part focused on flow rate mean values in which the available experimental data have been used to evaluate the accuracy of the developed models on a steady state aspect; the second part has been centered on a comparison between the two numerical models and the experimental data regarding the pressure ripples on the delivery outlet, focusing thus on a more dynamic aspect. If not specified, the following results were referred to a pump's rotational speed of 1500 rev/min and a delivery pressure of 200 bar, typical working operational value for the reference pump.

IV.4.1. Delivery Flow Mean Value

Figure 33 displays a comparison of the delivery flow rate mean values between the experimental and the simulated data for a number of different working conditions. The flow rate values were normalized to a reference value, Q_{ref}, for competitive reasons.

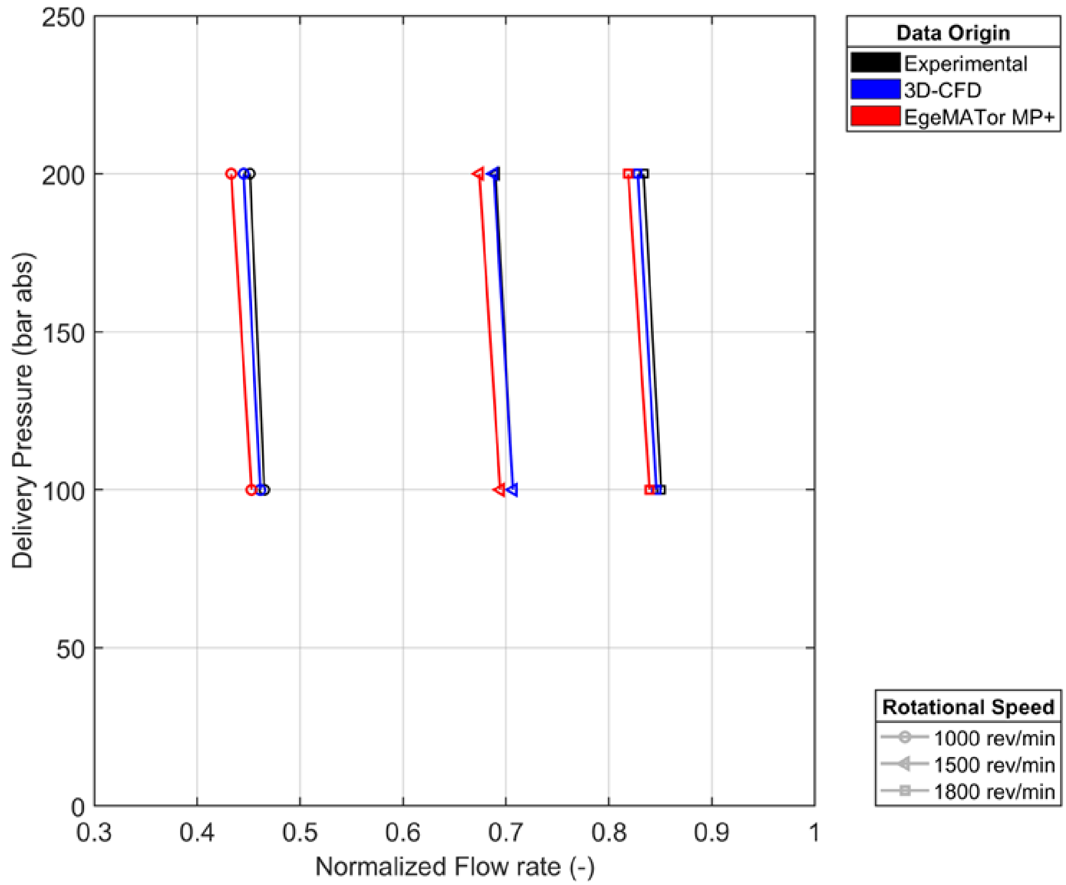

Figure 33 - Comparison of the normalized average flow rate between experimental data and numerical models.

The chart shows that both the numerical model predicted the delivery flow rate mean values and trend with great accuracy, with a percentage difference from the experimental data of less than 1% for the

3D CFD numerical model and less than 3% for the lumped parameters model, staying thus under the uncertainty range of the experimental measurements.

The 3D CFD approach showed excellent accuracy for the rotational speed of 1500 rev/min, while the other two analyzed speeds exhibited less accuracy. This is likely due to the chosen constraint required to execute the simulations approximated better real pump's conditions for the rotational speed of 1500 rev/min compared to the others.

The lumped parameters approach exhibited accuracy inferior to the CFD but constant for every speed analyzed, ensuring thus being reliable for a greater number of working conditions.

Furthermore, the lumped parameters model seems to overestimate internal leakages values, as this could explain the inverse proportionality of the accuracy to the delivery pressure.

As said before, the lumped parameter model simulated a high number of working conditions have been simulated with respect to the 3D CFD numerical model thanks to its reduced computational time required. The extra simulation values have not been included in the comparison for visual clarity.

Figure 34 shows a comparison of the delivery flow rate between only the experimental and all the available the simulated data obtained from the lumped parameter numerical model developed with the EgeMATor MP+ tool. This is showed to have a better overview of the capability of the model. The flowrate values were again normalized to a reference value, Q_{ref}, for competitive reasons.

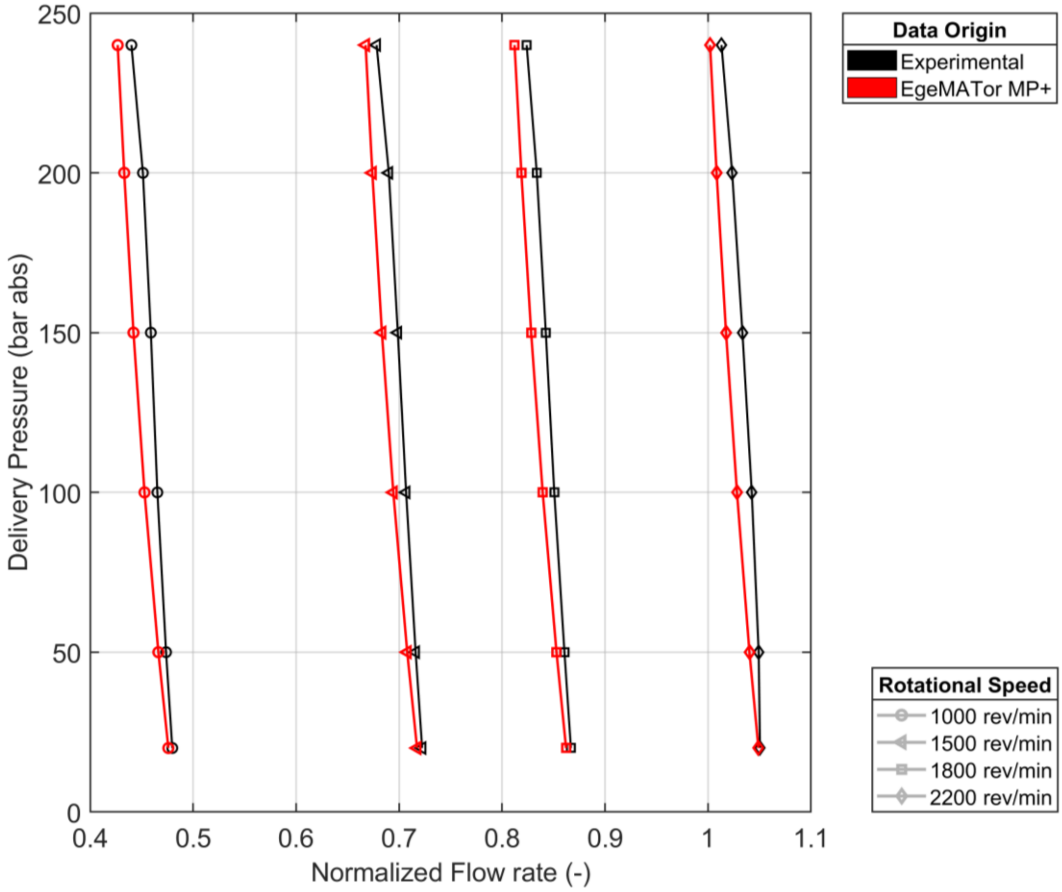

Figure 34 - Comparison of the normalized average flow rate between experimental data and lumped parameters numerical model results.

The increased number of working conditions showed that the hypothesis that the lumped parameters model seems to overestimate internal leakages values seems to be correct, as the simulations at lower outlet pressure are almost superimposable. Nevertheless, the overall results are completely satisfactory given the lower computational time and processing power required.

IV.4.2. Pressure Ripple Analysis

The analysis of the dynamic effects due to the pressure wave effects is virtually impossible to be executed with a lumped parameter approach numerical model due to the nature itself of the approach, imposing the homogeneity of the physical properties inside the CVs. Thus, to evaluate pressure ripples at the delivery side of the pump, a modification of the approach used were implemented, making the model not a pure lumped parametric approach but instead a hybrid 0D - 1D numerical model, even though the 1D aspect is extremely limited. The Simcenter Amesim environment used to develop the hydraulic simulation subroutine has the capability to simulate hydraulic straight pipe by means of a 1D CFD model, therefore allowing the analysis of the pressure variations inside the pipe. The hydraulic model was thus revised with the introduction of the hydraulic straight pipe model with the same fixed orifice used in the 3D CFD model and during the experimental tests that was positioned on the delivery side of the pump. Finally, a pressure sensor transmitter was positioned in the same position of the high frequency pressure transducer P_3 implemented in the experimental test campaign (as displayed in Figure 27).

Figure 35 displays a comparison of the pressure ripples trends between the experimental and the simulated data for a rotational speed of *1500 rev/min* and with a fixed orifice diameter of *1.72 mm*. The experimental data were averaged over three measure acquisitions in a steady-state condition for each case analyzed. The pressure ripples values have been normalized to reference value, p_{ref}, for competitive reasons.

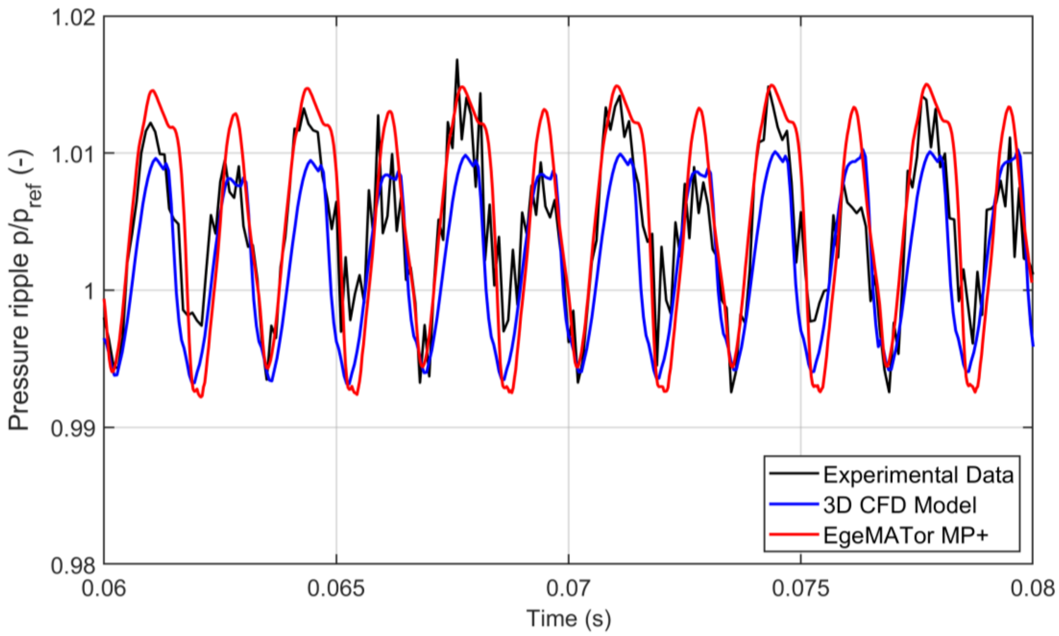

Figure 35 - Pressure ripples comparison for 1500 rev/min and fixed orifice of 1.72 mm.

The examination of the experimental data suggest that the pump exhibits a dual-flank behavior for the working condition analyzed. Both numerical models correctly predicted this behavior, reproducing the amplitude and the frequency of the pressure ripples measured with great accuracy. The CFD numerical model generally seems to better follows the ripples amplitude trends while the lumped model follows with good accuracy the first pressure ripple but overestimates the pressure drop of the intermediate throat and the second ripple peak of the meshing teeth couple.

Figure 36 displays the same pressure ripples trends comparison for a different working condition, which is a rotational speed of *1000 rev/min* with the same fixed orifice diameter of *1.72 mm*. The pressure ripples values have again been normalized to reference value, p_{ref}, for competitive reasons.

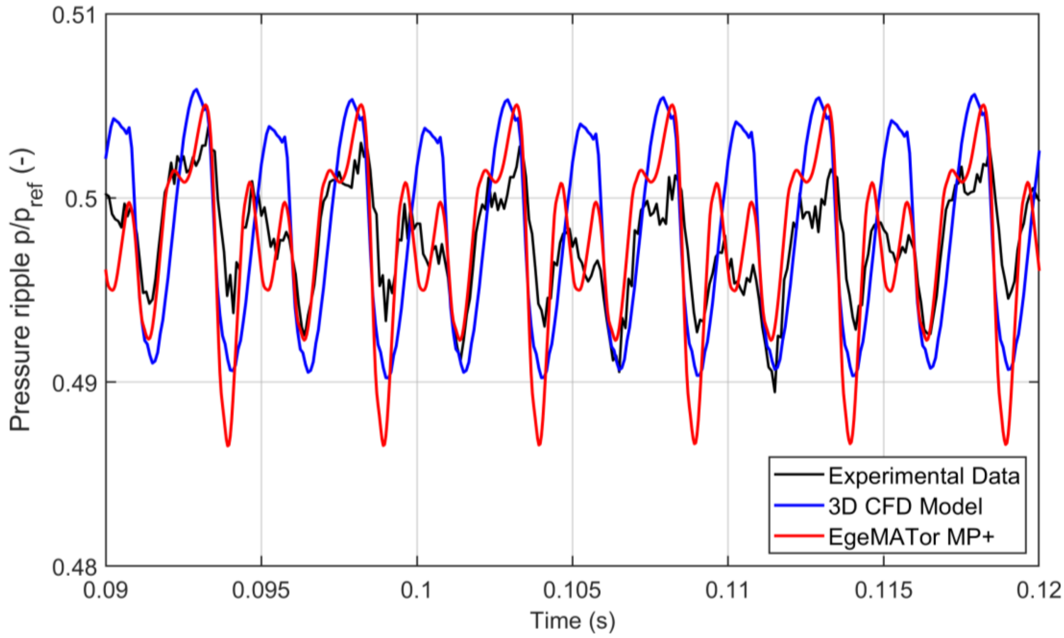

Figure 36 - Pressure ripples comparison for 1000 rev/min and fixed orifice of 1.72 mm.

The experimental data revealed that even for this working condition the dual-flank behavior was still present. Analyzing the chart, it can be seen that both numerical models replicate this behavior, correctly predicting the frequency of the pressure ripples measured with good accuracy, albeit with more amplitudes deviations than the previously analyzed case. The CFD numerical model, in fact, correctly predicted the first pressure ripple but greatly overestimated the second one. This error could be plausible attributed to the model constraint of fixed gears' positions and no null clearance.

The lumped parameter model exhibited again a higher pressure drop of the intermediate throat, but generally demonstrated better trend prediction of the second ripple compared to the 3D numerical model. This was partly thanks to the lower delivery pressure for the case analyzed that reduced the negative effect of the overestimation of leakages and brought out the positive effect of the evaluation of the teeth contact that the lumped parameters approach allows to consider.

As a further means of comparison and validation, a pressure analysis inside the meshing zone between the two numerical was conducted to evaluate how the two model handle the pressure spikes during the meshing of the gears.

Figure 37 presents the pressure spikes comparison for a variable chamber of the driven gear for the rotational speed of *1500 rev/min* and with a fixed orifice of *1.72 mm*. For this case as well the pressure values were normalized to reference value, p_{ref}, for confidentiality reasons.

Both numerical models handled the pressure spikes in the meshing zone in the same way, with the lumped parameter model reaching higher maximum pressure value and reaching the inlet pressure earlier than the 3D CFD model. This is most likely due to the wave effect phenomenon that the 3D CFD model can evaluate but the lumped parameter cannot, that contributes to build up a certain “hydraulic inertia” that delay the actual pressure increase or decrease.

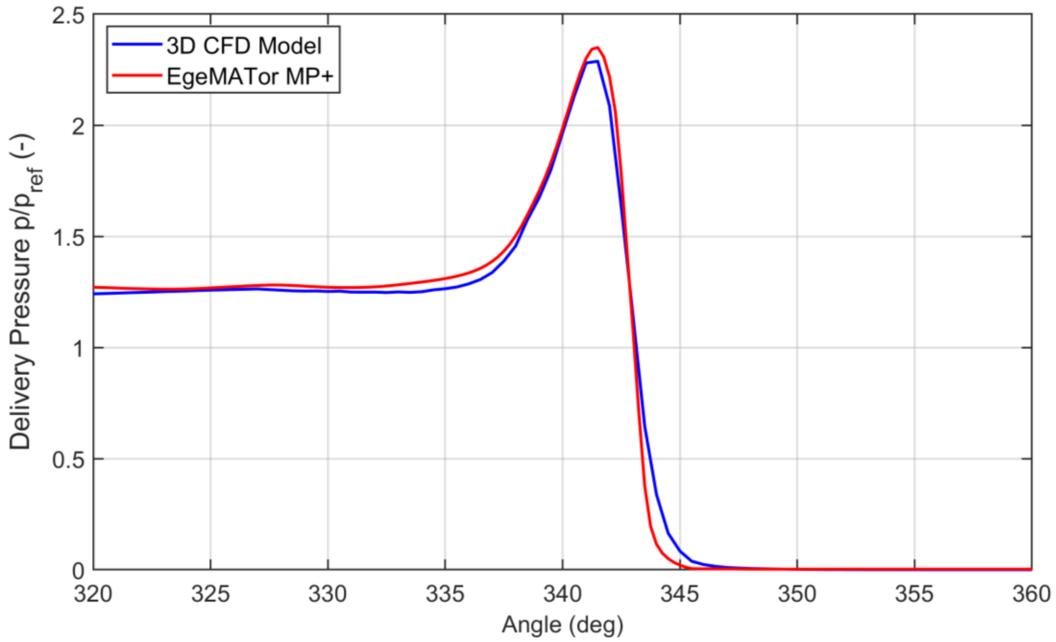

Figure 37 - Pressure spikes comparison for 1500 rev/min and fixed orifice of 1.72 mm.

IV.4.3. Validation Conclusions

The results of the validations showed that both the numerical model developed permitted to obtain high level of accuracy for both steady state and dynamics conditions. The lumped parameter tools showed a very satisfactory accuracy levels regarding the previsions of the flow rate in steady state conditions. The impressive results come from the dynamics analysis, in which the lumped parameters models exhibited similar if not better accuracy predictions than the 3D CFD numerical model, successfully predicting the double flank behavior of the pump requiring just a small fraction of the computational power but more importantly of the time required to simulate the working conditions. It is this great flexibility of the model that will be exploited in the next section, where an optimization procedure based on the lumped parameter approach of the EgeMATor MP+ tool will be described and validated.

Chapter V: EGPs Optimization Procedure

The high flexibility of the lumped parametric model allows to further expand the capability of the EgeMATor MP+ tool. In fact, the main reason that led to the development of this tools was the possibility to exploit the light computational resource required by the lumped parameter approach to implement optimization procedure to improve the EGPs performances, in particular regarding the noise emissions.

In particular, for hydraulic positive displacement machines, the noise sources are essentially of two types: fluid-borne noise (FBN) and structure-borne noise (SBN). FBN is due to the flow ripples and while SBN is mainly caused by the vibration of mechanical components as a consequence of force oscillations. These two typologies of noise sources affect the total air-borne noise (ABN) emission. Therefore, in order to study and reduce the ABN the understanding of fluid dynamics which is responsible for FBN generated inside the components is fundamental.

In the next sections, a methodology to optimize the pump's noise emissions by reducing flow ripples and pressure spikes in the meshing zone, considered the main noise source for an EGP, will be described. The described methodology will then be executed on the reference pump and the results will be briefly described. Finally, the optimization procedure will be validated through a noise emissions experimental campaign carried out in collaboration with the STEMS institute of Ferrara.

V.1. Optimal Groove Design Research Methodology

The developed numerical tool for studying and analyzing EGPs was designed to also include further capabilities such as optimization procedures. The methodology implemented in the developed tool allowed to optimize the design of pressure relief grooves inside the pump's wear plates for a given gears tooth profile.

This procedure was based on geometric assumptions in order to minimize the crossflow between delivery and suction while limiting pressure spikes during the meshing of the gears. To better understand the methodology used in this optimization procedure, a small description of the internal connections implemented in the lumped parameters model is required to describe in more detail the optimization methodology and the equations used in it.

Figure 7 shows a schematization of all the internal connection that were implemented in the model. As it can been seen, the connections between the variable displacement chamber volumes ($G_{i,vol}$ - $N_{i,vol}$) and the plate relief grooves are modeled as variable orifices. The opening and closing timings paired with the cross-sectional area values of these connections are the features that affect the most the EGP performance and behavior.

The previously described Surface Tool estimates the volume of a displacement chamber as function of the rotation angle, φ. The optimization procedure starts by finding the rotation angle value which corresponds to the minimum value of the chamber volume. The identified angle, φ_{DC_MIN}, express the angle at which the instantaneous switch between delivery and suction pressure occurs, representing thus one of the defining parameters for a correct design of the pressure relief grooves.

The optimization of the wear plate design around this angle value is of utmost importance to prevent too high pressure spikes and back flow rate. The next step implements the start of an iterative procedure. This iterative procedure requires the parametrization of the pressure relief grooves geometries, as the Figure 38a shows.

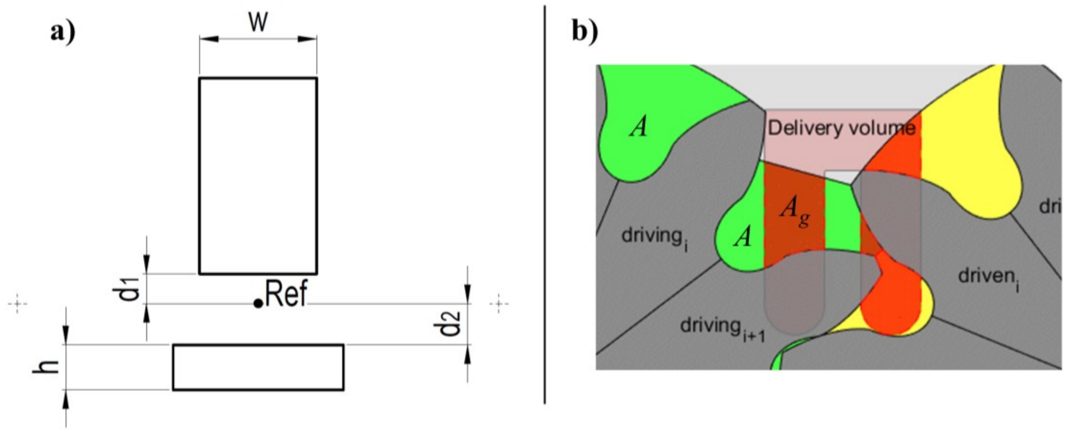

Figure 38 - Optimal groove design methodology: a) parameters for the groove shape design search; b) areas evaluated.

The parametrization was chosen to be normalized against the gear module m, to be independent by the size of the pump and they vary between an interval of values, as can be seen in Table 7.

__Table__ 7 - Grooves parametrization

Description	***Value***	***Min***	***Max***
Delivery Groove width	W	1	3
Suction Groove height	h	0.5	2
Delivery Groove reference distance	d_1	0	3
Suction Groove reference distance	d_2	0	3

For this work, a simple rectangular shaped groove design was chosen for both the delivery and inlet groove to be utilized for the optimization of the grooves design. The range of the parameters permitted to evaluate a large number of designs that were tested inside the iterative procedure against a series of objective functions:

$$TF_1 = \left|\varphi_{DC\_MIN} - \varphi_{GRV}\right| \tag{92}$$

$$TF_2 = \frac{1}{n}\sum_{i=1}^{n} A\left(\varphi_{DC\_MIN} \mp n\Delta\varphi\right) - A_g\left(\varphi_{DC\_MIN} \mp n\Delta\varphi\right) \tag{93}$$

The objective function TF_1 in equation (92) was implemented to check the volumetric efficiency of the tested design. To achieve high volumetric efficiency values, the TF_1 needs to be as small as possible. This implies the reduction of the angular difference between the rotation angle value of minimum chamber volume φ_{DC_MIN}, and the characteristics rotation angle value for the grooves φ_{GRV}, reducing thus the amount of backflow from delivery to inlet side. In particular, for the delivery groove, φ_{GRV} represents the rotation angle of connection closure between the groove and the delivery chamber, while φ_{GRV} represents the rotation angle of connection opening between the groove and the delivery chamber for the suction groove. The objective function TF_2 in equation (93) was implemented to minimize the internal pressure peaks occurring during gears' meshing in proximity of φ_{DC_MIN}. This objective function evaluates the cross-sectional area difference between the groove A_g (in dark red Figure 38b) and the projection area of the displacement chamber volumes on the lateral side A (in green Figure 38b). The reduction of the pressure peaks requires this difference to be as small as possible for a number n of points with an angular pitch distance from φ_{DC_MIN} equal to $\Delta\varphi$, with both values chosen as user input. This ensures a more gradual transition between the delivery and inlet area around the φ_{DC_MIN}, reducing thus the pressure peaks. The minus or plus sign in equation (93) are respectively for the delivery or suction groove. The iterative procedure has tested all the designs and then has selected the one that permitted to obtain the total minimal value for the sum of both objective functions, with an equal weight between them due to both of them were based on similar geometric assumptions. In this way, the methodology allowed to identify the optimal starting and ending positions for the pump pressure relief groove design. Future works will implement more complex geometries and objective functions to also permit the analysis of the groove shapes, thus further improving the optimization possibilities.

V.2. Optimization Methodology Results

The optimization methodology was applied on the reference pump to obtain a new and optimized geometry. The results of this optimization procedure leaded to a radical change of the design philosophy: from a symmetrical design of the pressure relief grooves geometries for the reference pump, to an asymmetrical one on which the front and rear wear plates exhibit pressure relief grooves with noteworthy geometric differences between them, as shown in Figure 39.

The validation of the optimization methodology was carried out in two phases: in the first phase, the new design was compared to the reference pump through numerical models; in the second phase, an experimental campaign was performed and the optimized design and the reference pump were tested on a specific test rig available in the laboratories of the CNR-STEMS research institute in Ferrara, allowing to test and acquire the flow rate and the noise emissions of the tested pumps.

The first phase was carried out simulating a number of working conditions and comparing the results obtained between the optimized and reference designs. To focus on the principal aspects investigated by the optimization methodology, the comparison examined the mean flow rate value, the non-uniformity of the flow rate and the pressure evolution inside the variable displacement chamber.

In this work, only the comparison results obtained for a pump speed of *1500 rev/min* and a system delivery pressure of *200 bar* are shown. The flow rate is presented normalized to a reference value, Q_{ref}, for confidential reasons.

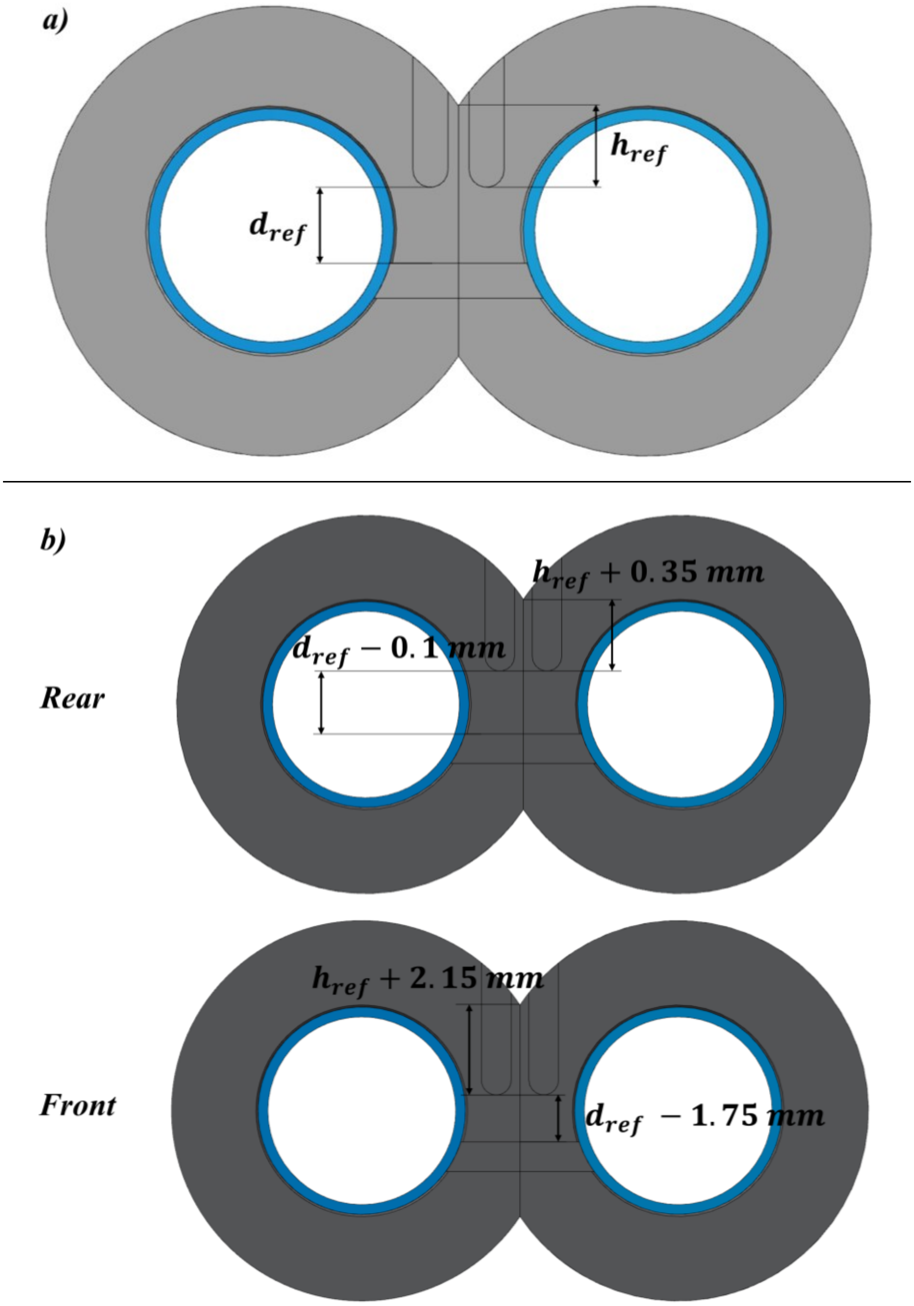

Figure 39 - Relief grooves design: a) reference pump; b) proposed optimized design.

Figure 40 and Table 8 show the numerical comparison between the reference and optimized design of the flow ripple and mean flow rate.

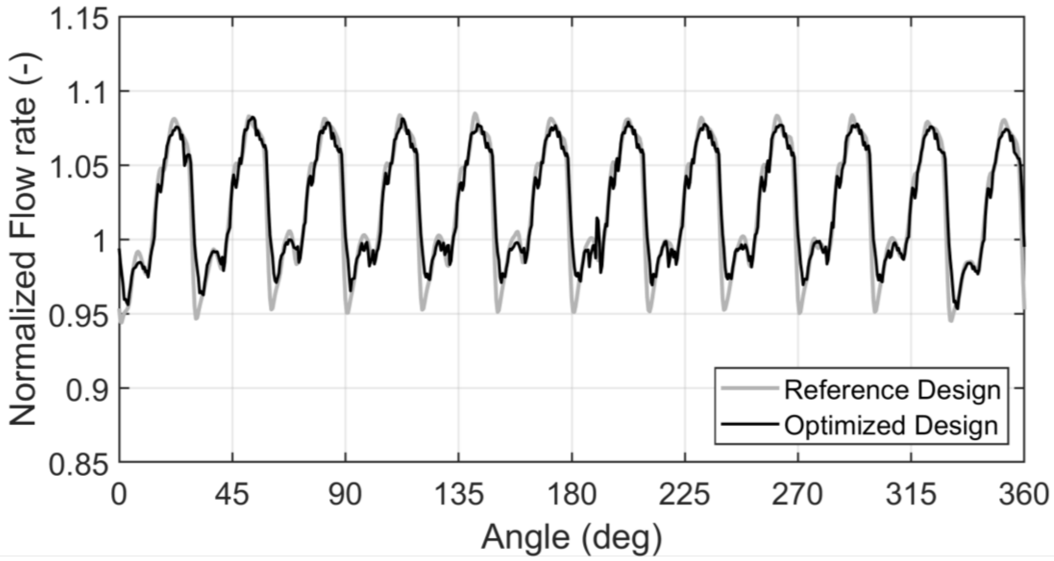

Figure 40 - Numerical flow ripple comparison at n=1500 rev/min, Δp=200 barA

The comparison shows that for both analyzed physical dimensions, the optimized design exhibited improved performances, with an increase of about *0.5%* of the mean delivery flow rate and a reduction of the non-uniformity of the flow ripple of around *8%*. In particular, the reduction of the non-uniformity rate was mainly due to a higher minimum value of the flow ripples. This aspect implies a lower value of backflow rate, one of the aspects on which the optimization methodology was focused on.

Table 8 *- Pump designs comparison at n=1500 rev/min Δp=200 barA.*

Description	***Value***	***Unit***
Mean flow rate Reference Design	1.021	Q_{ref}
Mean flow rate Optimized Design	1.024	Q_{ref}

Figure 41 presents another important result: the comparison of the numerical pressure evolution inside the variable displacement chamber around the meshing zone between the reference and optimized pumps.

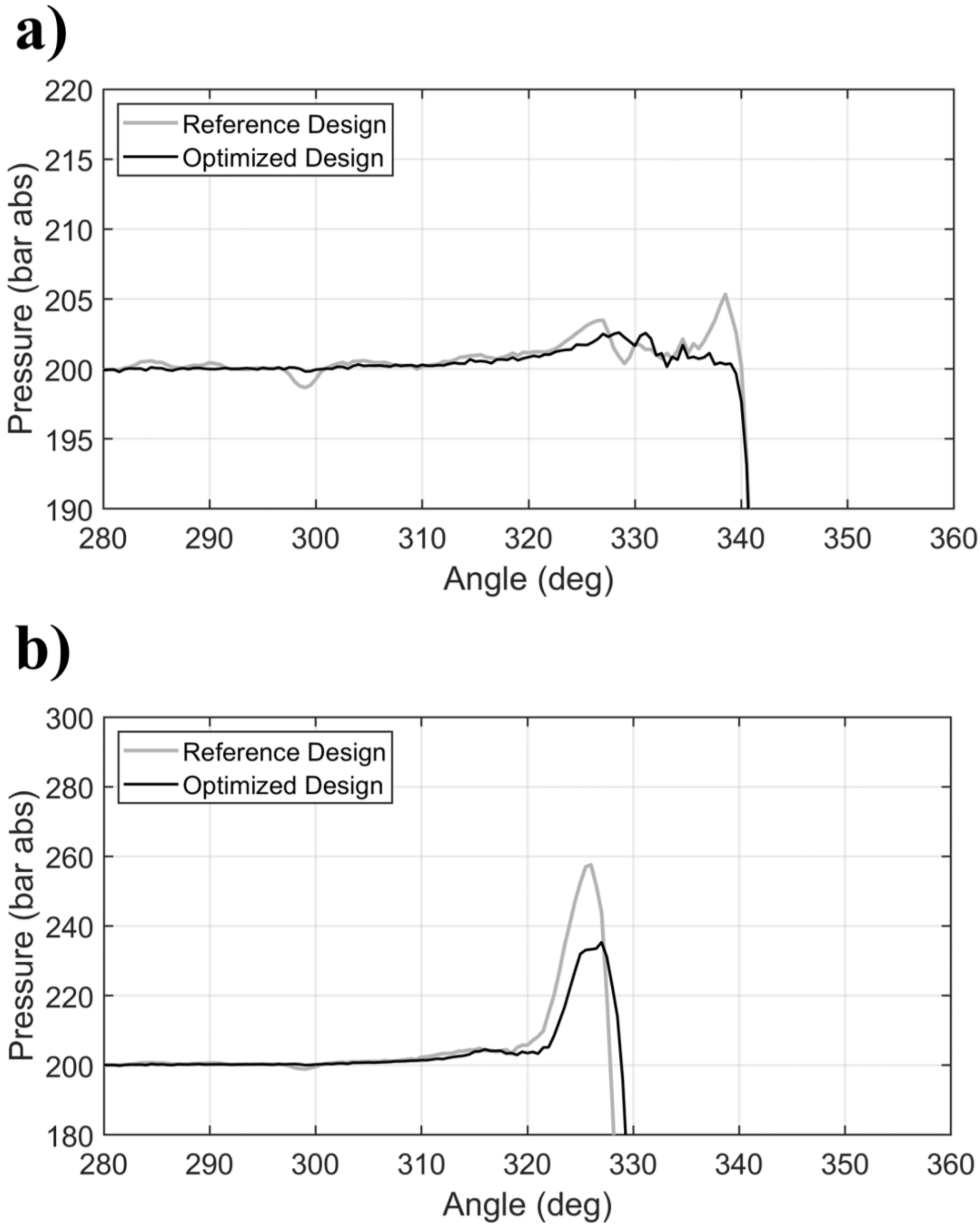

Figure 41 - Numerical pressure evolutions comparison at n=1500 rev/min, Δp=200 barA: a) driving gear; b) driven gear.

In particular, Figure 41a describes a chamber of the driving gear while Figure 41b of the driven gear. The comparison highlights a reduction of the pressure spikes during the gears' meshing of both the driving and driven gears' chambers, further suggesting the validity of the methodology employed. The reduction was mainly relevant for the driving gear's chamber, with pressure spikes reduction of about *10%*. This result, coupled with the reduction of the non-uniformity rate of the flow ripple, hinted to lower production of vibrations for the optimized design and hence a reduction to the noise emissions.

V.3. Optimization Methodology Experimental Validation

To validate the noise reduction suggested by the results of the numerical simulations, the second phase of the validation process was carried out. The new design was prototyped and both reference and optimized pumps were employed in an experimental campaign was executed with the collaboration of the CNR-STEMS research institute in Ferrara. This institute have a long and extensive knowledge of the noise and sound emission of hydraulic machines, especially for EGPs [50 - 51].

In fact, the laboratories of the CNR-STEMS research institute in Ferrara built a specific test rig for testing gear EGPs, which physically isolate the pump from the prime mover. In order to isolate the pump under test and acquire only the noise radiated from it, the pump was mounted on a metal plate placed inside a large shed while the prime mover and all the other hydraulic components were installed outside this shed and separated from the plate where the pump was mounted by a concrete wall. Both inlet and outlet pipes were routed to minimize the impact of the noise emitted by extraneous sources and passed through the wall. The pump flow rate was acquired thanks to the screw type flow meter installed on the pressure line. The hydraulic circuit also integrates pressure and temperature transducers that permitted to continuously monitor both these physical parameters during the acquisitions.

The tests were carried out with the oil maintained at a temperature of *40° C ± 3°C* thanks to the usage of an off-line cooling system. The environmental conditions were almost constant throughout the test, with air temperature ranging from *4* to *9 ℃* and humidity value ranging from *80* to *94 %*. The background noise was stationary, with SPLs always lower more than *15 dB* than the corresponding SPLs of the noise sources under test at each measurement point. In order to consider the directivity of the noise emissions of each pump tested, the sound pressure measurements were simultaneously performed in five different positions arranged at a *30 cm* distance from the noise source in each direction. The data acquisitions were performed using an *8-channels Siemens SCADAS analyzer (SCM-VM8.E module)* coupled with *Simcenter LMS Test.Lab software*. The microphones and the measurement instrumentation met the requirements of *class 1* instruments. Sound pressure measurements were performed in the frequency range of *20÷10000 Hz* and all the measurement chain was recalibrated several times over the course of the tests with a pistonphone (*Brüel&Kjær 4220*). This methodology ensures the repeatability of the operating conditions for all the pump under test.

The tests were performed at six different rotational pump speeds: *500 rev/min; 1000 rev/min; 1500 rev/min; 1800 rev/min; 2000 rev/min* and *2200 rev/min*. For each speed, six different delivery pressures were investigated, from no-load condition to maximum continuous pressure, in subsequent ascending and descending runs: *10 bar; 50 bar; 100 bar; 150 bar; 200 bar; 240bar*. Therefore, for each pump under test, for the 36 operating conditions chosen (*6* rotational speeds and *6* delivery pressure), a total of *72* flow value and 3*60* spectra of SPL measurements were acquired. The hydraulic scheme of the test rig is reported Figure 42a, while Figure 42b shows the sound measurement setup.

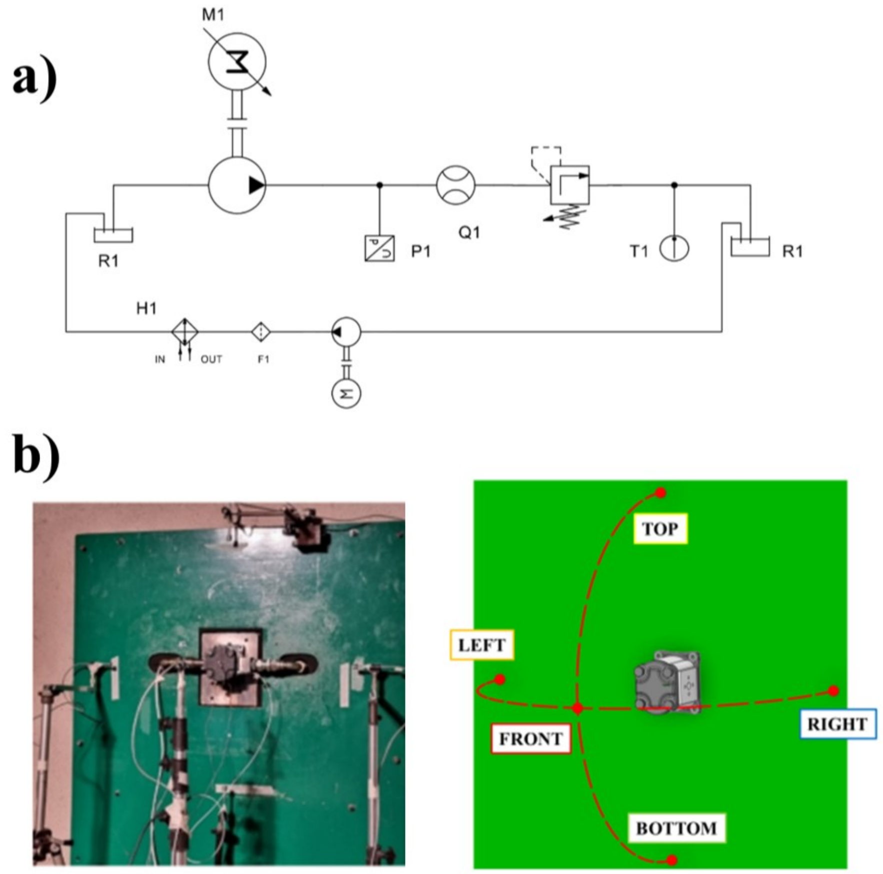

Figure 42 - Optimization experimental validation: a) test bench layout; b) noise measurement acquisition setup.

Figure 43 reports the SPLs difference between the reference and optimized pumps obtained from the experimental campaign. The SPLs are averaged over all the five microphones used. The chart displays that for all the working condition tested, the reference pump always exhibited higher SPL values, with a maximum difference of about *10 dBA* at high speed and high pressures and a mean difference of about *6 dBA*. These results validated the optimal groove design research methodology proposed in this work with a high degree of confidence and demonstrated the efficacy of the new optimized design.

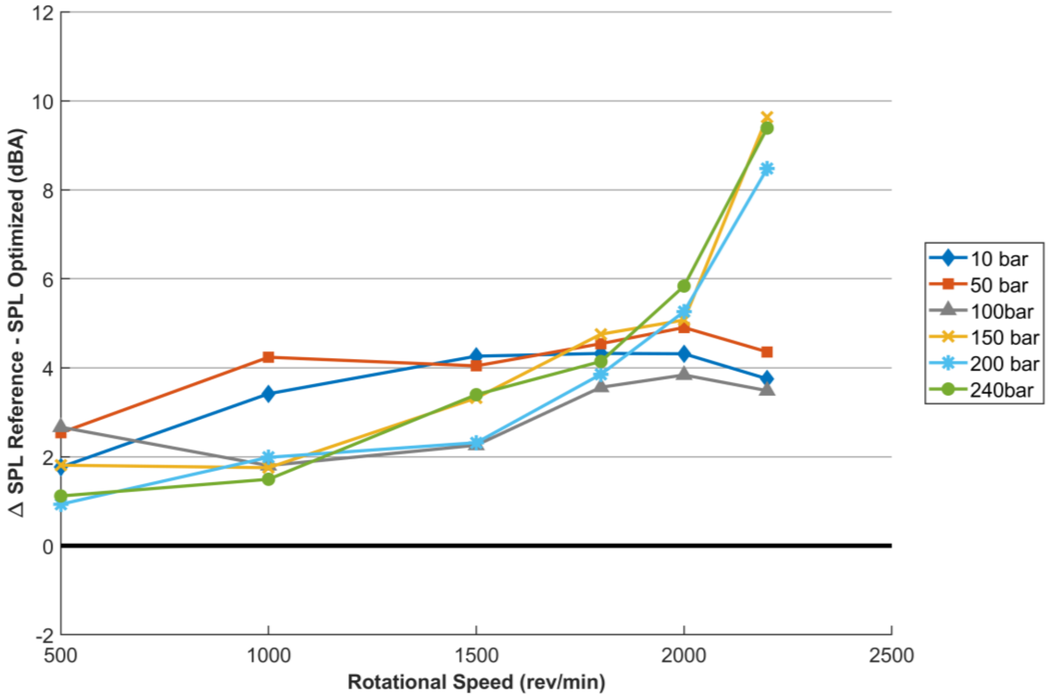

Figure 43 - SPLs difference between reference pump and optimized pump.

Chapter VI: Conclusions

In this Ph.D. thesis a comprehensive tool based on lumped parameter numerical model to analyze and optimize External Gear Pumps (EGPs) was presented and deeply described. The tool, named EgeMATor MP+, was developed by the Hydraulic Research Group of the University of Naples "Federico II" led by Professor Adolfo Senatore in collaboration with the international company Duplomatic Motion Solution and the Italian National Research Council (CNR-STEMS).

The tool was design with the possibility to study a wide range of EGPs, in particular the helical EGPs thanks to a methodology that take into consideration the adjustment required by the presence of a helical angle along the axial dimension of the pump for both the fluid-dynamics and mechanical characteristics.

The validation of this developed tool was executed on a reference commercial helical gear pump provided by the collaborating company Duplomatic Ms. The validation was executed in a hybrid way: before executing an experimental campaign on a test rig of the collaborating company, a 3D CFD numerical model was also developed and then validated along the lumped parameter model. This was done to compensate for the limited amount of test typologies that were doable on the available test bench. This validating methodology permitted to deeply validate the EgeMATor MP+ tool even with limited experimental data available.

The results from the validation proved that, while the 3D CFD numerical model achieved the higher accuracy level, the lumped parameter models exhibited only slightly lower accuracy level while requiring only a small fraction of the computational resource and time required by the 3D CFD numerical model.

This great flexibility of the EgeMATor MP+ permitted to employ what was the main focus of developing a lumped parameter-based tool, which is the possibility to employ optimization procedure. A geometrical base optimization procedure to optimize the design of the pressure relief's grooves was detailed. This optimization was aimed to reduce flow ripples and pressure spikes in the meshing zone, reducing thus the FBN emissions of the pump.

The methodology was applied to the reference helical EGPs, obtaining thus a new proposed design for the pressure relief's grooves. The new design was prototyped and an experimental campaign in collaboration with the CNR-STEMS research facility to evaluate the noise performances of the new design and validating thus the proposed optimization procedure.

The CNR-STEMS research facility built a specific test rig, which physically isolate the pump from the prime mover. This experimental campaign measured both flow rate and Sound Pressure Levels (SPLs). SPLs were measured in several points around each pump, allowing thus to analyze a more complete emissivity of the pump. The results of this experimental noise campaign confirmed the results obtained from the lumped parameter tool, with the optimized pump showed an average SPL value of 6 dBA lower than the reference pump, validating thus the methodology.

The developed EgeMATor MP+ tool showed great potentiality, allowing to both analyze and optimize the noise emission of different type of EGPs, making it thus a valuable tool for both the scientific and industrial field which will help to keep EGPs competitive in this electrification process, reducing the emerged disadvantages while trying to exploit the new possibilities allowed by it, such as the possibility of quickly varying the motor speed without losing efficiency, thus offsetting the fixed displacement characteristic or the possibility of combining the electric and hydraulic parts in a single more compact component, thus reducing the total weight.

Despite the excellent results achieved, the developed model still has some limits that will require further development. In fact, the model is currently limited to fluid-dynamics analysis only, lacking any type of structural analysis. This aspect needs to be developed and implemented in the tool to allow to also evaluate the structural component of the noise emission, thus further reducing it through a procedure to optimize both fluid-dynamics and structural aspects. Finally, the results obtained from the tool represent the values obtained from a pump not subjected to any work cycle. Therefore, a methodology to predict the actual wear of the components according to the work cycles undergone need to be developed in order to analyze its impact on both the fluid dynamic performance and the sound emission.

Nomenclature

Acronyms

Name	*Descriptions*
ABN	Air-Borne Noise
CAD	Computer-Aided Design
CFD	Computational Fluid Dynamics
CNR	Italian National Research Council
CPU	Central Processing Unit
CV	Control Volume
DAQ	Data Acquisition System
DXF	Drawing Exchange Format
EgeMATor MP+	External Gear Machine Multi Tool Simulator for Multiple Gears' Profiles
EGM	External Gear Machine
EGP	External Gear Pump
FBN	Fluid-Borne Noise
GIF	Graphics Interchange Format
IHA	Innovative Hydraulics and Automation
ISO	International Organization for Standardization
NCG	Non-Condensable Gas
RNG	Renormalization Group Theory
SBN	Structure-Borne Noise
SPL	Sound Pressure Level
STEMS	Sciences and Technologies for Sustainable Energy and Mobility
TSV	Tooth Space Volume

Symbols

Name	*Descriptions*
C_c	Cavitation condensation coefficient
C_e	Cavitation evaporation coefficient
D_v	Diffusivity of the vapor mass fraction (m^2/s)
$D_{v,d}$	Diffusivity of the dissolved NCG (m^2/s)
$f_{d,equil,ref}$	Equilibrium mass fraction of the dissolved gas at the reference pressure
f_g	Mass fraction of free NCG
$f_{g,d}$	Free NCG mass fraction
$f_{g,f}$	Mass fraction of dissolved NCG
$f_{g,specified}$	User-specified value
f_v	Mass fraction of the vapor
n	Rotational speed (rev/min)
$\vec{\boldsymbol{n}}$	Surface normal of the surface σ
p	Pressure (Pa)
p_{ref}	Reference pressure value (Pa)
$p_{d,equil,ref}$	Reference pressure for the dissolved gas equilibrium mass fraction (Pa)
p_v	Phase-change threshold pressure (Pa)
Q_{ref}	Reference Flow rate value (L/min)
R_e	Vapor generation rate
R_c	Vapor condensation rate
$S_{g,d}$	Source of dissolved NCG (kg/m^3)
V	Volume (m^3)
$\vec{\boldsymbol{V}}$	Fluid velocity vector (m/s)

Greek Symbols	**Description**
β	Total Helix angle (rad)
β_k	Fluid bulk modulus (Pa)
μ_t	Turbulent viscosity (Pa·s)

ρ	Density of mixture (kg/m^3)
ρ_{atm}	Fluid density at atmospheric pressure (kg/m^3)
ρ_g	Density of gas (kg/m^3)
ρ_l	Density of liquid (kg/m^3)
σ	Surface of the control volume (m^2)
$\sigma_{g,d}$	Dissolved Gas Schmidt number
σ_v	Vapor Schmidt number
Ω	Control volume (m^3)
τ	Time scale (s)
$\vec{\boldsymbol{\tau}}$	Stress tensor
φ	Angle (deg)
$\Delta\varphi$	Saving delta angle (deg)

Reference

[1] E. Scolaro, M. Beligoj, M. P. Estevez, L. Alberti, M. Renzi and M. Mattetti, "Electrification of Agricultural Machinery: A Review," in IEEE Access, vol. 9, pp. 164520-164541, 2021, https://doi.org/10.1109/ACCESS.2021.3135037.

[2] A. Lajunen, J. Suomela, J. Pippuri, K. Tammi, T. Lehmuspelto, P. Sainio, "Electric and Hybrid Electric Non-Road Mobile Machinery – Present Situation and Future Trends," *World Electr. Veh. J.* 2016, *8*, 172-183, https://doi.org/10.3390/wevj8010172.

[3] L. Ge, L. Quan, X. Zhang, B. Zhao, J. Yang, "Efficiency improvement and evaluation of electric hydraulic excavator with speed and displacement variable pump," Energy Conversion and Management, Volume 150, 2017, Pages 62-71, ISSN 0196-8904, https://doi.org/10.1016/j.enconman.2017.08.010.

[4] K. Korane, "Electrification Exposes Hydraulic-Pump Shortcomings," [Online] https://www.fluidpowerworld.com/electrification-exposes-hydraulic-pump-shortcomings (accessed on 24 March 2023).

[5] P. Y. Li, J. Siefert, D. Bigelow, "A Hybrid Hydraulic-Electric Architecture (HHEA) for High Power Off-Road Mobile Machines," Proceedings of the ASME/BATH 2019 Symposium on Fluid Power and Motion Control, ASME/BATH 2019 Symposium on Fluid Power and Motion Control, Longboat Key, Florida, USA, October 7–9, 2019, V001T01A011, ASME, https://doi.org/10.1115/FPMC2019-1628.

[6] J. Ivantysyn, M. Ivantysynova, "Hydrostatic Pumps and Motors: Principles, Design, Performance, Modelling, Analysis, Control and Testing," Tech Books International, 2003.

[7] M. Rundo, "Models for Flow Rate Simulation in Gear Pumps: A Review," *Energies* 2017, *10*, 1261, https://doi.org/10.3390/en10091261.

[8] N. D. Manring, S. B. Kasaragadda, (September 18, 2003), "The Theoretical Flow Ripple of an External Gear Pump," ASME. J. Dyn. Sys., Meas., Control, September 2003, 125(3): 396–404, https://doi.org/10.1115/1.1592193.

[9] X. Zhao, A. Vacca, “Theoretical Investigation into the Ripple Source of External Gear Pumps,” Energies 2019, 12, 535, https://doi.org/10.3390/en12030535.

[10] E. Frosina, A. Senatore, M. Rigosi, “Study of a High-Pressure External Gear Pump with a Computational Fluid Dynamic Modeling Approach,” Energies 2017, 10, 1113, https://doi.org/10.3390/en10081113.

[11] A. Vacca, M. Guidetti, "Modelling and experimental validation of external spur gear machines for fluid power applications," Simul.Model. Pract. Theory, vol. 19, pp. 2007-2031, 2011 ISSN 1569-190X, https://doi.org/10.1016/j.simpat.2011.05.009.

[12] M. Borghi, M. Milani, F. Paltrinieri, B. Zardin, "Pressure Transients in External Gear Pumps and Motors Meshing Volumes," SAE Technical Paper 2005-01-3619, 2005, https://doi.org/10.4271/2005-01-3619.

[13] M. Borghi, B. Zardin, E. Specchia, "External Gear Pump Volumetric Efficiency: Numerical and Experimental Analysis," SAE Technical Paper 2009-01-2844, 2009, https://doi.org/10.4271/2009-01-2844.

[14] S. Mancò, N. Nervegna, "Simulation of an external gear pump and experimental verification," in Proceedings of the JHPS International Symposium on Fluid Power, Tokyo, Japan, 13–16 March 1989, https://doi.org/10.5739/isfp.1989.147.

[15] A. S. Heisler, J. J. Moskwa, F. J. Fronczak, "Simulated Helical Gear Pump Analysis Using a New CFD Approach," Proceedings of the ASME 2009 Fluids Engineering Division Summer Meeting. Volume 1: Symposia, Parts A, B and C, Vail, Colorado, USA. August 2–6, 2009, pp. 445-455, ASME, https://doi.org/10.1115/FEDSM2009-78472.

[16] F. Qi, S. Dhar, V. Nichani, C. Srinivasan, et al., "A CFD study of an Electronic Hydraulic Power Steering Helical External Gear Pump: Model Development, Validation and Application," SAE Int. J. Passeng. Cars - Mech. Syst. 9(1):346-352, 2016, https://doi.org/10.4271/2016-01-1376.

[17] A. Corvaglia, A. Ferrari, M. Rundo, O. Vento, “Three-dimensional model of an external gear pump with an experimental evaluation of the flow ripple,” Proceedings of the Institution of Mechanical Engineers, Part C: Journal of

Mechanical Engineering Science, 2021, 235(6):1097-1105, https://doi.org/10.1177/0954406220937043.

[18] T. Ransegnola, X. Zhao, A. Vacca, “A comparison of helical and spur external gear machines for fluid power applications: Design and optimization,” Mechanism and Machine Theory, Volume 142, 2019, 103604, ISSN 0094-114X, https://doi.org/10.1016/j.mechmachtheory.2019.103604.

[19] M. Battarra, E. Mucchi, “A method for variable pressure load estimation in spur and helical gear pumps,” Mechanical Systems and Signal Processing, Volumes 76–77, 2016, Pages 265-282, ISSN 0888-3270, https://doi.org/10.1016/j.ymssp.2016.02.020.

[20] B. Zardin, M. Borghi, (2008), “Modeling and simulation of external gear pumps and motors,” 5th FPNI PhD Symposium, 323-341.

[21] G. Marinaro, E. Frosina, A. Senatore, “A Numerical Analysis of an Innovative Flow Ripple Reduction Method for External Gear Pumps,” Energies 2021, 14, 471, https://doi.org/10.3390/en14020471.

[22] S. Falfari, P. Pelloni, "Setup of a 1D Model for Simulating Dynamic Behaviour of External Gear Pumps," SAE Technical Paper 2007-01-4228, 2007, https://doi.org/10.4271/2007-01-4228.

[23] E. Mucchi, G. Dalpiaz, A. Fernàndez del Rincòn, “Elastodynamic analysis of a gear pump. Part I: Pressure distribution and gear eccentricity,” Mechanical Systems and Signal Processing, Volume 24, Issue 7, 2010, Pages 2160-2179, ISSN 0888-3270, https://doi.org/10.1016/j.ymssp.2010.02.003.

[24] E. Mucchi, G. Dalpiaz, A. Rivola, “Elastodynamic analysis of a gear pump. Part II: Meshing phenomena and simulation results,” Mechanical Systems and Signal Processing, Volume 24, Issue 7, 2010, Pages 2180-2197, ISSN 0888-3270, https://doi.org/10.1016/j.ymssp.2010.02.004.

[25] E. Mucchi, G. Dalpiaz, “Elasto-dynamic analysis of a gear pump–Part III: Experimental validation procedure and model extension to helical gears,” Mechanical Systems and Signal Processing, Volumes 50–51, 2015, Pages 174-192, ISSN 0888-3270, https://doi.org/10.1016/j.ymssp.2014.05.048.

[26] E. Mucchi, G. Dalpiaz, A. Fernàndez del Rincòn, “Elasto-dynamic analysis of a gear pump–Part IV: Improvement in the pressure distribution modelling,”

Mechanical Systems and Signal Processing, Volumes 50–51, 2015, Pages 193-213, ISSN 0888-3270, https://doi.org/10.1016/j.ymssp.2014.05.049.

[27] F. Rituraj, A. Vacca, M. A. Morselli, "Modeling of manufacturing errors in external gear machines and experimental validation," Mechanism and Machine Theory, Volume 140, 2019, Pages 457-478, ISSN 0094-114X, https://doi.org/10.1016/j.mechmachtheory.2019.06.016.

[28] W. Strasser, (October 27, 2006). "CFD Investigation of Gear Pump Mixing Using Deforming/Agglomerating Mesh," ASME. J. Fluids Eng. April 2007, 129(4): 476–484, https://doi.org/10.1115/1.2436577.

[29] F. Orlandi, G. Muzzioli, M. Milani, F. Paltrinieri, L. Montorsi, "Development of a Numerical Approach for the CFD Simulation of a Gear Pump under Actual Operating Conditions," Fluids 2023, 8, 244, https://doi.org/10.3390/fluids8090244.

[30] R. Rituraj, A. Vacca, M. A. Morselli, "Thermal Modelling of External Gear Machines and Experimental Validation," Energies 2020, 13, 2920, https://doi.org/10.3390/en13112920.

[31] J. Zhou, A. Vacca, P. Casoli, "A novel approach for predicting the operation of external gear pumps under cavitating conditions," Simulation Modelling Practice and Theory, Volume 45, 2014, Pages 35-49, ISSN 1569-190X, https://doi.org/10.1016/j.simpat.2014.03.009.

[32] R. S. Devendran, A. Vacca, "Optimal design of gear pumps for exhaust gas aftertreatment applications," Simulation Modelling Practice and Theory, Volume 38, 2013, Pages 1-19, ISSN 1569-190X, https://doi.org/10.1016/j.simpat.2013.06.006.

[33] X. Zhao, A. Vacca, S. Dhar, "Numerical Modeling of a Helical External Gear Pump With Continuous-Contact Gear Profile: A Comparison Between a Lumped-Parameter and a 3D CFD Approach of Simulation," Proceedings of the BATH/ASME 2018 Symposium on Fluid Power and Motion Control, BATH/ASME 2018 Symposium on Fluid Power and Motion Control, Bath, UK, September 12–14, 2018, V001T01A053, ASME, https://doi.org/10.1115/FPMC2018-8903.

[34] F. Sadeghi, “6 - Elastohydrodynamic lubrication,” Editor(s): Homer Rahnejat, Tribology and Dynamics of Engine and Powertrain, Woodhead Publishing, 2010, Pages 171-226e, ISBN 9781845693619, https://doi.org/10.1533/9781845699932.1.171.

[35] G. W. Stachowiak, A. W. Batchelor, “4 - Hydrodynamic Lubrication,” Editor(s): G. W. Stachowiak, A. W. Batchelor, Engineering Tribology (Third Edition), Butterworth-Heinemann, 2006, Pages 103-204, ISBN 9780750678360, https://doi.org/10.1016/B978-075067836-0/50005-5.

[36] G. W. Stachowiak, A. W. Batchelor, “5 - Computational Hydrodynamics,” Editor(s): G. W. Stachowiak, A. W. Batchelor, Engineering Tribology (Third Edition), Butterworth-Heinemann, 2006, Pages 205-259, ISBN 9780750678360, https://doi.org/10.1016/B978-075067836-0/50006-7.

[37] G. Vogelpohl, “Beitrage zur Kenntnis der Gleitlagerreibung,” Ver. Deutsch. Ing., Forschungsheft, 1937, pp. 386.

[38] A. Cameron, “Principles of Lubrication,” Chapter by M.R. Osborne on Computation of Reynolds' Equation, Longmans, London, 1966, pp. 426-439

[39] ISO 4409:2019 - Hydraulic fluid power - Positive-displacement pumps, motors and integral transmissions - Methods of testing and presenting basic steady state performance, ISO/TC 131/SC 8, 2019, https://www.iso.org/standard/68410.

[40] M. Borghi, B. Zardin, "Axial Balance of External Gear Pumps and Motors: Modelling and Discussing the Influence of Elastohydrodynamic Lubrication in the Axial Gap," Proceedings of the ASME 2015 International Mechanical Engineering Congress and Exposition, Volume 15: Advances in Multidisciplinary Engineering, Houston, Texas, USA, November 13–19, 2015, V015T19A038, ASME, https://doi.org/10.1115/IMECE2015-51632.

[41] C. Schleihs, E. Viennet, M. Deeken, H. Ding, X. Xia, S. Lowry, H. Murrenhoff, “3D-CFD simulation of an axial piston displacement unit,” In Proceedings of the 9th International Fluid Power Conference, Aachen, Germany, 24–26 March 2014, pp. 332–343, https://publications.rwth-aachen.de/record/661817.

[42] P. Casoli, A. Vacca, G. Franzoni, “A Numerical Model For The Simulation of External Gear Pumps,” Proceedings of the JFPS International Symposium on Fluid Power, 2005, Volume 2005, Issue 6, Pages 705-710, Released on J-STAGE November 08, 2011, Online ISSN 2185-6303, https://doi.org/10.5739/isfp.2005.705.

[43] R. Castilla, P.J. Gamez-Montero, N. Ertürk, A. Vernet, M. Coussirat, E. Codina, “Numerical simulation of turbulent flow in the suction chamber of a gearpump using deforming mesh and mesh replacement,” International Journal of Mechanical Sciences, Volume 52, Issue 10, 2010, Pages 1334-1342, ISSN 0020-7403, https://doi.org/10.1016/j.ijmecsci.2010.06.009.

[44] Y. Y. Liu, K. An, H. Liu, J. G. Gong, L. Q. Wang, (2019), “Numerical and experimental studies on flow performances and hydraulic radial forces of an internal gear pump with a high pressure,” Engineering Applications of Computational Fluid Mechanics, 13:1, 1130-1143, https://doi.org/10.1080/19942060.2019.1666746.

[45] L. Zhou, Z. Wang, (December 19, 2007), "Numerical Simulation of Cavitation Around a Hydrofoil and Evaluation of a RNG κ-ε Model," ASME, J. Fluids Eng. January 2008, 130(1): 011302, https://doi.org/10.1115/1.2816009.

[46] D. S. Zhang, W. D. Shi, B. Chen, X. F. Guan, “Unsteady flow analysis and experimental investigation of axial-flow pump,” Journal of Hydrodynamics, Ser. B, Volume 22, Issue 1, 2010, Pages 35-43, ISSN 1001-6058, https://doi.org/10.1016/S1001-6058(09)60025-1.

[47] F. Perini, K. Zha, S. Busch, R. Reitz, "Comparison of Linear, Non-Linear and Generalized RNG-Based k-epsilon Models for Turbulent Diesel Engine Flows," SAE Technical Paper 2017-01-0561, 2017, https://doi.org/10.4271/2017-01-0561.

[48] Simerics Inc., Simerics MP+’s User Manual—V 5.2.15, Simerics: Bellevue, WA, USA, 2022.

[49] A. K. Singhal, M. M. Athavale, H. Li, Y. Jiang, (August 19, 2002), "Mathematical Basis and Validation of the Full Cavitation Model," ASME, J. Fluids Eng, September 2002, 124(3): 617–624, https://doi.org/10.1115/1.1486223.

[50] E. Carletti, F. Pedrielli, (2019), "Noise and Vibration Risk Assessment for the Operators of Crawler Loaders," Archives of Acoustics, 44, 761-773, https://doi.org/10.24425/aoa.2019.129731.

[51] E. Carletti, G. Miccoli, F. Pedrielli, G. Parise, (2016), "Vibroacoustic Measurements and Simulations Applied to External Gear Pumps. An Integrated Simplified Approach," Archives of Acoustics, 41, 285–296, https://doi.org/10.1515/aoa-2016-0028.

Ringraziamenti

I ringraziamenti sono sempre la parte più difficile dopo un corso di dottorato lungo tre anni che mi ha portato a conoscere e collaborare con numerose persone, in quanto il rischio di dimenticare qualcuno è altissimo.

Inizio ringraziando il prof. Senatore e la prof.ssa Frosina che mi hanno supportato e soprattutto sopportato sin dal mio percorso di tesi magistrale e mi hanno indirizzato verso questo percorso di dottorato, credendo nelle mie capacità forse anche più di me stesso; li ringrazio insieme a tutto il FPRG, Luca, Gianluca, Antonella, Pasquale e Raffaele per i bei momenti passati insieme, confidando nella possibilità di ulteriori esperienze in futuro.

Non posso non ringraziare il prof. Grassi, coordinatore del corso di Dottorato, sempre disponibile a risolvere problemi burocratici e altre mie "scoccianti" richieste.

Ringrazio con affetto la prof.ssa Minav, che mi ha permesso di trascorrere un breve ma intenso periodo in Finlandia, espandendo così la mia conoscenza sia dal punto di vista accademico che culturale; il gruppo di ricerca IHA, Abid, Vinay, Thèo, Chunjie, IIris, Sebastian, Daniel, Joonas, Matias, Ville e Zakhar, che mi hanno accolto in Finlandia e mi hanno aiutando a districarmi nella cultura locale e facendomi dimenticare della distanza da casa.

Ringrazio Duplomatic MS per la possibilità offertami, in particolare nella persona di Roberto Maddalon. Ringrazio il mio tutor aziendale Michele Pavanetto e Simone Bulleri, che insieme mi hanno aiutato a crescere dal punto di vista lavorativo; ringrazio Raffaello, Ina, Riccardo, Emanuele, Esther, Paola, Andrea e tutti gli altri colleghi che mi hanno fornito conoscenza tecnica e, forse più importante, supporto morale.

Ringrazio tutto il gruppo di ricerca dell'istituto STEMS-IMAMOTER di Ferrara, Francesca, Eleonora, Pietro e Alessandro. Grazie a loro sono riuscito ad approfondire la parte acustica del mio lavoro di tesi ad un livello superiore e con il quale è stato un vero piacere collaborare.

Infine, ma naturalmente non per importanza, ringrazio la mia famiglia, mio fratello Francesco che mi ha sopportato durante i miei sproloqui in videochiamata ma soprattutto mia madre Lina, in quanto senza i suoi innumerevoli sacrifici e la sua ferma convinzione nelle mie capacità, molto probabilmente non avrei raggiunto i vari traguardi della mia vita.

In conclusione, dedico questo lavoro di tesi ai miei due nonni che sono stati sempre presenti ad ogni mio risultato importante nella vita ma che purtroppo non sono più tra noi.